

ABSTRACT

Title of dissertation: MOSQUITO-INSPIRED
SWARMING AND PURSUIT FOR
AUTONOMOUS ROTORCRAFT

Daigo Shishika, Doctor of Philosophy, 2017

Dissertation directed by: Professor Derek A. Paley
Department of Aerospace Engineering
Institute for Systems Research

The long-term goal of this research is to design cooperative-control algorithms for autonomous vehicles inspired by the collective behaviors in animal groups. The specific research objectives of this dissertation are twofold: (1) to analyze and model the swarming and pursuit behaviors observed in the mating swarms of mosquitoes, and (2) to design mosquito-inspired control algorithms to perform swarming and pursuit with autonomous rotorcraft.

The first part of this dissertation analyzes the reconstructed flight data of the malarial mosquito *Anopheles gambiae* to characterize the velocity-alignment interaction between male mosquitoes, who aggregate to form mating swarms and subsequently pursue a female mosquito. Both swarming and pursuit behaviors are represented using self-propelled particle models. The model is used together with tools from control theory to investigate the connection between velocity-alignment behavior and success in pursuit. The results of this research have a potential impact on vector-control methods for malaria, and are also utilized in the second part of

this dissertation.

The second part of this dissertation studies two types of pursuit problems inspired by the collective behavior in mosquito swarms. The first problem considers the strategy for a single pursuer chasing a single target. This problem has been studied extensively for the application to missile guidance and navigation. Here, we tailor the assumptions on the dynamics of the agents as well as the design criteria for the application to small and agile rotorcraft. The second pursuit problem incorporates the swarming behavior by considering a scenario in which multiple guardian vehicles are deployed to protect an area against fast intruders. We derive necessary and sufficient conditions for capturing the intruder. We also present swarming strategies to maximize the performance of the guardians, inspired by the random-oscillatory motion and the velocity-alignment behavior of male mosquitoes.

MOSQUITO-INSPIRED SWARMING AND
PURSUIT FOR AUTONOMOUS ROTORCRAFT

by

Daigo Shishika

Dissertation submitted to the Faculty of the Graduate School of the
University of Maryland, College Park in partial fulfillment
of the requirements for the degree of
Doctor of Philosophy
2017

Advisory Committee:
Professor Derek A. Paley, Chair/Advisor
Professor Rama Chellappa
Professor Inderjit Chopra
Professor P. S. Krishnaprasad
Professor Robert M. Sanner

© Copyright by
Daigo Shishika
2017

Acknowledgments

First and foremost, I sincerely thank my advisor, Prof. Derek Paley, for giving me the opportunity to join the Collective Dynamics and Control Laboratory (CDCL) and pursue my degree in the United States. When I came from Japan and joined his group five years ago, I did not know that it would become my second home that I will truly miss. I thank Dr. Paley for his thoughtful guidance, which allowed me to have the freedom to explore the problems that interest me. He always gave me encouragement and support, instead of pressure, even when a paper deadline was approaching. He taught me the importance of scientific writing through his painstaking effort in editing paper drafts. He also taught me, without words, various skills to be successful in academia including accessibility in communication, time management, and collaboration. I was fortunate to be able to absorb those skills over the past five years. He will continue to be my role model as a researcher with innovative ideas and effective communication skills, a mentor with encouraging guidance, a teacher with clear and illuminating lectures, and a father with commitment to family fulfillment.

For their time and feedback I am grateful to my dissertation committee members, Professors P. S. Krishnaprasad, Robert Sanner, Rama Chellappa, and Inderjit Chopra. The classes I have taken from Dr. Krishnaprasad and Dr. Sanner made the core of my skill set as a control engineer. Their enthusiasm and dedication in teaching greatly inspire me.

For discussions about mosquito behaviors, I thank Dr. Nicholas Manoukis of

United States Department of Agriculture and Dr. Sachit Butail of Northern Illinois University. This was my first collaborative work when I was starting my research in the graduate school. I thank them for being very supportive and patient during the preparation of my first journal paper. Moreover, my dissertation research was only possible because of their preceding efforts in collecting mosquito data.

I gratefully acknowledge the help from Dr. Derrick Yeo in setting up the quadrotor experiments. He was always willing to spend time teaching me how things work in hardware implementation. I also thank Justin Yim who joined us through the NSF Research Experiences for Undergraduates program. By building an autonomous hovercraft testbed, he turned my theory on paper into something that works in reality. I still admire his passion and excitement towards his research. I also thank undergraduate students Zeyad Emam and Katarina Sherman for their contributions to my projects.

I was very fortunate to be surrounded by wonderful students in the CDCL. I thank Frank Lagor, who paved the path by completing every milestone in the program a little ahead of me, making past five years a enjoyable journey. I also owe thanks to Dr. Levi DeVries, Dr. Tracie Severson, Chin Gian Hooi, Dr. Nitin Sydney, Dr. Amanda Chicoli, Dr. Feitian Zhang, Dr. Derrick Yeo, Will Craig, Brett Barkley, Brian Free, Jinseong Lee, Debdipta Goswami, Helene Nguewou, and Dr. Will Scott for all the happy memories.

The AHS Student Design Competition was a great opportunity for me to work with people in the University of Maryland's Rotorcraft Center of Excellence. I thank my teammates Stacy Sidle, Chris Bogdanowicz, Brandon Gudenius, Xing

Wang and Justin Winslow. I also acknowledge the faculty members and senior students including Prof. Inderjit Chopra, Dr. V. T. Nagaraj, Dr. Ananth Sridharan, Dr. Bharath Govindarajan and Dr. Vikram Hrishikeshavan, for their support and guidance.

Outside of academic work, I thank my friends and fellow graduate students for providing me with breathing space. I am grateful to Kota Hara for being my tennis partner, as well as Dan Escobar, Tyler Sinotte, and Lauren Trollinger for organizing the volleyball and soccer events that made for many entertaining afternoons. I also thank my friends in Japan for all the fun times during my visit back home.

I thank the people who supported me in preparing my application for the graduate program in the U.S., especially Dr. Yoshiaki Kuwata, Dr. Yu Wang, and my former advisors at the University of Tokyo, Prof. Keiji Kawachi and Prof. Nobuo Takeda.

Finally, I want to thank my family for their unwavering support. I thank my parents, Futoshi and Sumiko, for always believing in me and for supporting me in every possible way. To my sister Sakura, your energy and effort towards your professional goals have always inspired me. I thank my brother Wataru for showing us how to enjoy life and be happy. I dedicate this dissertation to all of my family.

Table of Contents

List of Tables	viii
List of Figures	ix
1 Introduction	1
1.1 Motivation	2
1.2 Background and Related Work	4
1.2.1 Analysis and Modeling of Animal Group Behavior	4
1.2.2 Pursuit Problems for Autonomous Agents	7
1.3 Contributions of Dissertation	10
1.4 Outline	13
2 Analyses and Modeling of Swarming Behavior	15
2.1 Correlation Function	16
2.2 Interaction Network	20
2.2.1 Induced Interaction Graph	20
2.2.2 Features of Pairwise Interaction Network	22
2.2.3 Differences between Species	25
2.3 Swarm Model	26
2.3.1 Simulated Swarm Model without Interaction	26
2.3.2 Simulated Swarm Model with Interaction	27
2.4 Discussion	30
3 Analyses and Modeling of Pursuit and Coupling Behavior	34
3.1 Switching in Male's Behavior	35
3.2 Initiation of Close Encounter	37
3.2.1 Classical Pursuit	37
3.2.2 Motion Camouflage	39
3.3 Male-Female Coupling Flight	42
3.4 Swarm Model with Pursuit Behavior	46
3.4.1 Force Model	46
3.4.2 Female Model and Pursuit	49

3.4.3	Parameter Switching	50
3.5	Lyapunov Stability Analysis	52
4	Mosquito-Inspired Pursuit: Single Pursuer Case	57
4.1	Background	58
4.1.1	Design Criteria	58
4.1.2	Problem Formulation	60
4.1.3	Ultimate Boundedness	63
4.1.4	Hovercraft Testbed	64
4.2	Theoretical Results	67
4.2.1	Bio-inspired Pursuit Law	67
4.2.2	Robustness to Measurement Error	70
4.2.3	Modification of the Pursuit Law	75
4.2.4	Comparison with Existing Pursuit Laws	76
4.2.5	Robustness to Control Saturation	81
4.3	Experimental Results	86
4.3.1	Measurement Noise	86
4.3.2	Comparison between Pursuit Laws	88
4.3.3	Comparison with Theory	90
5	Mosquito-Inspired Swarming for Decentralized Pursuit	92
5.1	Background	93
5.1.1	Inspiration from Mosquitoes	93
5.1.2	Problem Formulation	95
5.2	Control Theoretic Analysis	98
5.2.1	Limitation of Static Guardian	99
5.2.2	Sufficient Conditions for Target Capture	101
5.3	Algorithms and Simulation Results	106
5.3.1	Orbiting Strategy	107
5.3.2	Random-Swarming Strategy	112
5.3.3	Optimal Randomness	117
5.3.4	Gain Modulation	118
5.3.5	Velocity-Alignment Strategy	121
5.4	Experimental Results	124
5.4.1	Experimental Testbed	125
5.4.2	Disturbance Observer	126
5.4.3	Effect of Time Delay	127
5.4.4	Optimal Randomness	128
5.4.5	Velocity-Alignment Strategy	130
6	Conclusion	135
6.1	Summary	135
6.2	Ongoing Work and Proposed Work	138
6.2.1	Mosquito Mate Selection	138
6.2.2	Rotorcraft Pursuit in Three Dimensions	140

6.2.3	Competition between Two Swarms	141
A	Supplemental Theoretical Results	148
A.1	Calculation of β^*	148
A.2	Required N_P for Circling Strategy	149
	Bibliography	152

List of Tables

2.1	Linear regression model	26
2.2	Parameters for the swarm simulation	29
3.1	Parameter switching between three behavioral states	51
4.1	Characteristics of state measurement errors	87
4.2	Performance of various pursuit laws	90
5.1	System parameters and their nominal values	98
5.2	Nondimensionalized system parameters	100
5.3	Parameters in the swarming algorithm	115

List of Figures

1.1	Two objectives of dissertation	2
2.1	Calculation of unit-velocity cross correlation	18
2.2	Time interval between tight turns	19
2.3	Frequency distribution of correlation values	21
2.4	Visualization of interaction network.	23
2.5	Features of interaction and network	24
2.6	Augmented swarming model with interaction	28
2.7	Model fit to swarming data from two real swarms	30
3.1	The definition of close encounter	36
3.2	Vectors and angles used to define classical pursuit metric	37
3.3	Time history of metric classical pursuit metric	38
3.4	Classical pursuit metric from seven data sets	39
3.5	Time history of motion camouflage metric	41
3.6	Motion camouflage metric from seven data sets.	41
3.7	Trajectories of male and female during coupling flight	43
3.8	Model fit of relative acceleration during coupling flight	43
3.9	Control gains during coupling flight	44
3.10	Illustration of model parameters	47
3.11	The pursuit state from start to end	50
3.12	State transition diagram for male mosquito	51
3.13	Simulation snapshot of three different behaviors	52
4.1	Trajectories of wild mosquitoes in coupling flight	59
4.2	Reference frames and coordinates	61
4.3	Autonomous hovercraft testbed	64
4.4	Ultimate boundedness of the solutions in the x_2x_3 -plane	73
4.5	Comparison of the controller specific terms	79
4.6	Numerical simulation until the first close encounter	80
4.7	Numerical simulation of near-miss scenario	81
4.8	Nullclines of the system	83
4.9	Four different configurations of nullclines	84

4.10	Measurement errors in the experiments	88
4.11	Experimental trial up until the first close encounter	89
5.1	Illustration of the swarming and pursuit scenario	95
5.2	Sufficient condition on the initial velocity for target capture	104
5.3	Conditions for target capture in the nondimensional parameter space	106
5.4	Effect of initial conditions on the orbiting motion	109
5.5	Effect of orbiting motion on the probability of target capture	109
5.6	Optimal orbiting motion	111
5.7	Mean velocity with varying white noise intensity	116
5.8	Snapshots of the swarm with varying randomness	116
5.9	Probability of target capture as a function of K_r	118
5.10	Snapshots of the swarm with varying elongation parameter σ	121
5.11	Probability of target capture with velocity-alignment behavior	123
5.12	The architecture of the experimental setup	125
5.13	Probability of target capture as a function of K_r	129
5.14	Velocity-alignment forcing in simulation and experiment	131
5.15	Snapshots of pursuit scenario with velocity-alignment strategy	133
6.1	Payoff matrix	143
A.1	Computing saturation factor β for pursuit force	148
A.2	Definitions of angles and speeds in the velocity space	149
A.3	Example of circling motion	150
A.4	Sufficient number of circling guardians for guaranteed target capture	151

Chapter 1

Introduction

Cooperative control of autonomous mobile robots has been studied for various applications including search and rescue, surveillance, cargo transportation, and environmental monitoring. The advantages of multi-agent systems include their capability to cover a large area simultaneously, to distribute the work load (both physical and computational) within the agents, and their robustness to failure of individual agents. The challenge lies in the complexity of the systems involving multiple agents, and the essential task for engineers is to make such systems operate reliably under various conditions. Collective behaviors in animal groups, which show remarkable coordination with high robustness to uncertainties in the natural environment, have inspired engineers to design algorithms that emulating them. This dissertation studies cooperative control strategies for small and agile rotorcraft inspired by the behaviors of the malarial mosquito *Anopheles gambiae* (*An. gambiae*).

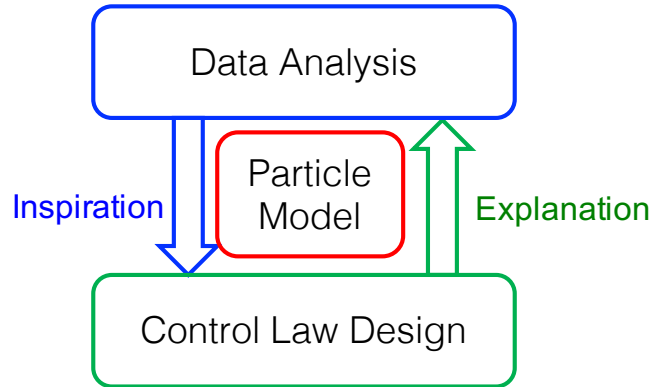


Figure 1.1: Two objectives of the dissertation.

1.1 Motivation

The males of *An. gambiae* aggregate and form a mating swarm to attract a female mosquito. A female, which flies faster than the males, passes through the swarm several times until she mates with a single male. These collective dynamics of mosquitoes contain two key aspects—swarming and pursuit—that are relevant to various control problems for autonomous mobile robots. In addition, the collective behavior of males shows an interesting combination of collaboration and competition, i.e., they cooperate with one another to form a swarm in order to increase the chance of an encounter with a female, but they also compete against each other to capture the female. Furthermore, the fact that the female moves faster introduces an additional challenge to the pursuit problem for male mosquitoes.

Inspired by the aforementioned observations that are unique to mosquito swarms, we seek to design control laws that achieve swarming and pursuit flight with autonomous rotorcraft. To make use of the observations from mosquito behaviors in control design, we first desire to have a sufficient understanding of the

biological system. Therefore, the objectives of this dissertation are two fold: biological data analyses and bio-inspired control design. Figure 1.1 illustrates the interrelation between the two parts. The goal is to use tools from engineering to understand the biological system, and then to use inspirations from the biological system to solve engineering problems.

Previously, Butail et al. [1] obtained video sequences of the malarial mosquito *An. gambiae* in Mali, Africa. The authors developed a tracking software to reconstruct three-dimensional kinematics (positions and velocities) of flying mosquitoes from the image sequences. Understanding some of the collective behaviors based on the reconstructed flight data is the objective of the first part of this dissertation. Since insect aggregations have highly random motion as compared to more organized group behaviors such as bird flocks or fish schools, one of our interests is in characterizing the inter-agent interactions that may exist but are obscured by the apparent randomness of the swarm. We also seek to understand how males' swarming behavior is related to their success in pursuit. Understanding the processes that lead to mating in this species of mosquito has potential to aid in a release-based program of malaria vector control.

In studying the pursuit flight of male mosquitoes, we attempted to compare it against existing pursuit strategies developed for engineering applications. Missile guidance and navigation is one of the fields in which the problem of pursuit has been extensively studied. However, the dynamics of fixed-wing vehicles (or missiles) and small and agile agents (like mosquitoes) are so different that we could not find an appropriate algorithm to employ. This difficulty motivated our study of pursuit laws

for small and agile agents. Since mosquitoes can hover around a fixed point in the space and also change their directions of motion rapidly, we emulate their behavior using rotorcraft micro aerial vehicles (MAVs), instead of fixed-wing vehicles.

We are also interested in the randomness that exists in mosquito swarms, in contrast to collective motion in bird flocks or formation control of aircraft, where well-organized coordinated flight is desired. We formulate a novel problem that combines both swarming and pursuit aspects. In particular, we consider a scenario where multiple guardian vehicles are deployed to protect an area against fast intruders. Our interest is to see how the strategies inspired by the behaviors of male mosquitoes (e.g., random oscillatory motion and velocity-matching interaction) can be useful in this pursuit scenario for autonomous vehicles. The results of the second part of this dissertation have potential application to drone countermeasures.

1.2 Background and Related Work

This section presents previous research in the field that is relevant to the two topics we study in this dissertation: (1) analysis and modeling of animal group behavior, and (2) pursuit problems for autonomous vehicles.

1.2.1 Analysis and Modeling of Animal Group Behavior

Collective movement of animals exemplified by birds [2–4] and fish [5–8] is often analyzed using the concept of *collective order*. The most standard form of order is *polarization*, which quantifies how well the velocity vectors of the group members

are aligned with each other. An example of a polarized group is a pigeon flock [4], where members fly in parallel resulting in the translation of the entire group.

Although polarization is a commonly used order parameter, the concept of collective order is more general. Consider a milling motion in fish [8]. The velocity vectors of the group members are not polarized, but there is a collective order in the form of rotation. In addition, a group can expand or contract, which gives rise to dilatational collective order [9].

Unlike bird flocks or fish schools, aggregation of insects appears to lack collective order, and therefore the interactions that may exist between the animals are less obvious compared to groups with collective order. Researchers have found evidence of local interactions in midge swarms. Kelly et al. [10] used speed distributions and the statistics of spatial arrangement to find evidence for local clusters of correlated motion. Attanasi et al. [9] used an instantaneous velocity correlation to show evidence for correlated motion based on a metric perception mechanism.

The swarming behavior of malarial mosquitoes also appears to lack collective order. Crepuscular swarms of *An. gambiae* and *Anopheles coluzzii*, formerly known as the M and S “molecular forms” [11], can be described as three-dimensional leks with characteristics of scramble competition by numerous males for a few females [12]. The behavioral and evolutionary bases for mating swarms in this species have only recently been examined in detail and observations to date suggest that it does not fall neatly into a single category [12–14]. One important area of investigation in the mating system of these malaria vectors is the nature and extent of male-male interaction in the swarm. Male-male interactions are represented in theories of lek

formation, where they range from aggression or arena defense [15], to collectively increased signaling to females [16], and association with successful males [17].

In modeling and analyzing various animal group behaviors discussed above, self-propelled particle models are useful. Vicsek et al. [18] first introduced a self-propelled particle model to show that some emergent behaviors observed in animal collectives can be generated by a simple model in which individuals move in the average direction of their neighbors. Following this work, researchers have used self-propelled particle models to investigate many other collective behaviors in animal groups.

Couzin et al. [19] used a particle model to investigate the spatial dynamics of an animal group such as a fish school or bird flock; this model revealed the existence of group-level behavioral transitions related to minor changes in individual-level interactions. Scott and Leonard [20] studied a three-agent model involving a single pursuer (a bear) and two evaders (a mother caribou and her calf), and performed stability analysis of some equilibrium formations. Gazi and Passino [21] studied a general class of attraction/repulsion functions that can be used to achieve swarm aggregations; they presented stability analysis to characterize swarm cohesiveness, size, and motion.

Following the work by Okubo [22] on the dynamics of insect aggregation, Butail et al. modeled swarming mosquitoes as particles attached to the centroid of the swarm with damped spring [23]. They also used a velocity autocorrelation to find the natural frequency and the damping ratio of the mosquito's oscillatory motion. This dissertation extends these prior works and augments the existing

particle model in Chapters 2 and 3.

Particle models are not only useful in investigating animal behaviors, but have also been used to design formation controls for multiple vehicles. For example, Leonard and Fiorelli [24] presented a framework for coordinated and distributed control of multiple autonomous vehicles using artificial potentials and virtual leaders. Paley and Leonard [25] showed the stability of the parallel and circular group motion presented in [19], and extended it to a control law for trajectory tracking. Olfati-Saber and Murray [26] presented a dynamic, graph-theoretic framework for flocking and used it to achieve obstacle avoidance. Gazi [27] considered a general model for vehicle dynamics and used sliding-mode control to track the motion of swarm members presented in [21]. This dissertation formulates pursuit problems using self-propelled particle models in Chapters 4 and 5.

1.2.2 Pursuit Problems for Autonomous Agents

The problem of pursuit has a number of applications such as missile guidance, surveillance, robot control, and animal behavior. Taxonomy and surveys of the research in the field have been presented, for example, in [28] and [29]. Depending on how we model the environment, pursuer, and the target—including the number of agents, their dynamics, and sensing capabilities—pursuit problems can be divided into a variety of subcategories [29].

In general, pursuit problems are mathematically formulated as a system of differential equations describing the motion of the pursuer and the target. The

input to the system are the control algorithms of the agents, and the definition for successful target capture is typically given by some conditions on the agents' positions and velocities. Of interest is the design of pursuit algorithms to guarantee target capture while considering other design criteria such as time optimality, energy efficiency, and robustness to uncertainties. Note that the evasion strategy for the target is also an equally important problem, although it is not the main focus of this dissertation.

There are two distinct approaches in studying pursuit problems. The first approach, which is related to game theory, formulates the problem as a pursuit-evasion game. This approach utilizes an objective function (e.g., distance between the agents) that the pursuer tries to minimize while the evader tries to maximize. Optimization techniques are used to find the optimal algorithms for both the pursuer and the evader. Pioneering work in this field was done by Isaacs [30], who formalized a class of problems known as differential games. The second approach designs pursuit laws a priori and then analyzes the behavior of the system. The control laws are designed based on the tools from control theory, or sometimes from the observation of biological systems. This dissertation uses the latter approach for its convenience in incorporating mosquito-inspired attributes.

In the recent history, pursuit has been studied extensively for application to missile guidance and navigation. In the missile-guidance literature, it has been shown that a viable approach to target intercept is stabilizing the line of sight (LOS), i.e., the line extending from the pursuer to the target [31]. The idea is to enhance the efficiency of target intercept by avoiding the tail-chase scenario, which

may occur with pure pursuit (also known as classical pursuit [32]) in which the pursuer simply aims directly at the target. A well-known strategy to achieve the LOS stabilization is called proportional navigation (PN) [33–35]. PN is known to have optimality in terms of the square integral of the control effort against a non-maneuvering target [36]. Some variants of PN can be found in [37–40].

Pursuit is also an important component in biological systems ranging from prey capture to mating [20, 41, 42]. Stabilization of the LOS has also been studied in this context and related strategies include constant-bearing pursuit and motion camouflage [32, 41]. Animals like bats [41] and insects [12, 42] execute pursuit with limited sensor accuracy using highly agile motion. These characteristics are especially pertinent to the bio-inspired pursuit problem using small, robotic vehicles considered in Chapter 4.

The aforementioned works on pursuit typically define the success of pursuit as target *intercept*, where the pursuer aims to collide into the target. On the other hand, a less aggressive pursuit scenario considered for the application to autonomous robots is target *tracking*, where a pursuer seeks to approach and stay close to the target without colliding with it. A path-planning algorithm to track a ground vehicle with a UAV is proposed in [43]. Strategies to encircle a target with a team of pursuers are proposed in [44, 45]. The idea of tracking is also utilized in formation control as the concept called *cyclic pursuit* [46, 47]. Each agent pursues another agent in the group to generate a chain of leader-follower interactions [48, 49].

The capabilities of the pursuers greatly influence the pursuit problem. First, consider how a pursuer’s sensor is modeled. One category in the pursuit-evasion

game is the so-called *search problem*, in which a pursuer has limited perceptual range [50, 51]. The objective of a pursuer is to intelligently search for the target without the knowledge of its location (pursuit before detection). On the other hand, in the missile-guidance literature and in target-tracking problems, it is assumed that the pursuer at least knows the position of the target (pursuit after detection). Second, consider how the dynamics of the pursuer are modeled. In the robotics community, there are studies on pursuit problems for the application to agents with specific constraints [52, 53]. However, more generally, when the agents are treated as point particles, the majority of pursuit-evasion games assume that the pursuer has a constant speed [43–45, 50], whereas some other works consider variable speed [54, 55]. With a unique combination of these assumptions, this dissertation introduces a novel pursuit problem in Chapter 5.

1.3 Contributions of Dissertation

This dissertation makes contributions to the understanding of the behaviors in the mating swarms of mosquitoes and in the application to control design for autonomous rotorcraft. Some materials from this dissertation have been previously published or submitted for review, including [56–59]. Conference papers in which early versions of these results appeared include [60, 61]. Some results—including the analysis of pursuit and coupling behavior described in Chapter 3—have not yet appeared elsewhere.

We characterize the interaction between male mosquitoes in their mating

swarms. We develop a time-resolved correlation function to quantify the degree of velocity alignment for a given pair of mosquitoes. The correlation function is applied to different data sets (male only swarms, male-female coupling flights, and simulated swarms) to obtain probability distributions of the correlation value. Using Bayes' decision rule, we define a threshold on the correlation value to determine whether a given pair of mosquitoes are interacting or not. The correlation threshold combined with the lag analysis generates instantaneous interaction graphs, which show that the male mosquitoes form subgroups whose size and membership change rapidly. We also improve an existing particle model by including local interactions represented by damping of the relative velocity between males. The new model provides a better null hypothesis against which to test deviations from normal swarming behavior.

We also study the velocity-alignment behavior in relation to the pursuit behavior. We analyze the pursuit behavior preceding the formation of a male-female couple in the swarm to find the pursuit strategy used by mosquitoes. We also model the coupling flight using a delayed differential equation, i.e., the relative acceleration is modeled as a force from a damped spring (with delay) connecting the couple. We show that the spring and damping constants, which can be interpreted as control gains, increase when the male changes its behavior from swarming to coupling. We extend the existing particle model by including gain switching, and also a particle that represents a female mosquito. The new model produces three behaviors observed in a mosquito swarm—swarming, velocity-alignment, and pursuit. We perform Lyapunov stability analyses on the particle model to show how

the velocity-alignment behavior during the swarming phase can potentially increase the success of subsequent pursuit.

Inspired by the pursuit in mosquito mating swarms, we study two pursuit problems. The first problem considers pursuit of a single target by a single pursuer, in which the assumptions on each agent’s dynamics and design criteria are specific for small and agile vehicles. We design a pursuit law based on Lyapunov analysis and establish its robustness to unknown target acceleration and measurement errors using the concept of ultimate boundedness. Robustness to control saturation is analyzed using the phase portrait of the closed-loop system. We also present results from experiments that were conducted to study the practical challenges involved in pursuit by lightweight platforms with noisy sensors. These experiments highlight the benefit of using less control effort in the presence of large measurement errors, when compared with existing pursuit guidance laws.

The second problem considers a scenario in which multiple guardians with limited perceptual range and bounded acceleration are deployed to protect an area from an intruder. The main challenge for the guardian (male mosquito) is to quickly respond to a fast intruder (female) by matching its velocity. We focus on the strategy in the swarming phase, when a guardian has not yet perceived the intruder. In the parameter space consisting of the intruder’s speed and guardians’ abilities (i.e., maximum acceleration and perceptual range) we identify necessary and sufficient conditions for target capture. We propose swarming algorithms inspired by the behavior of male mosquitoes to improve the target capture capability. The theoretical results are illustrated by experiments with an indoor quadrotor swarm.

The problem studied in this work can be applied to a situation where multiple vehicles are deployed to enforce a no-fly zone, for the application to drone counter-measures, or for convoy protection. The results of this work may provide guidelines in selecting the capabilities of vehicles for such applications, and also provide a methodology to fully utilize those capabilities.

1.4 Outline

Chapter 2 analyzes the swarming behavior of male mosquitoes, and characterizes their intermittent velocity-alignment interaction. We propose a particle model that includes velocity-alignment behavior and show how it reduces the discrepancy between the existing swarm model and the flight data of real swarms. A discussion of the results and their significance are provided at the end of the chapter.

Chapter 3 analyzes the pursuit and coupling behavior of mosquitoes. We first present how the male's behavior switches with a close encounter with a female mosquito. We then analyze the mechanism that causes the close encounter to occur, in relation to existing pursuit strategies (i.e., pure pursuit, motion camouflage). We model the relative motion between the male and female during the coupling phase and use the result to extend the particle model to include pursuit behavior. Finally, we perform Lyapunov analysis of the particle model to show the effect of male's velocity-alignment behavior on his success in pursuing a female.

Chapter 4 formulates and studies the pursuit problem for small and agile agents. After proposing a pursuit law and showing its robustness to unknown target

maneuver and sensor noise, we compare it against existing pursuit laws analytically, numerically, and experimentally. We experimentally implemented the pursuit laws using an autonomous hovercraft testbed. The experimental results, which validate the theoretical contributions, are provided at the end of the chapter.

Chapter 5 formulates and studies the cooperative pursuit problem for a swarm of guardian vehicles protecting an area from fast intruders. We characterize this new pursuit problem with control-theoretic analyses. We then propose swarming strategies inspired by the swarming behavior of male mosquitoes. The performance of the swarming strategies are illustrated by computer simulation and also by experiments with small quadrotors in a motion-capture environment.

Chapter 6 concludes the dissertation and suggests directions for future research.

Chapter 2

Analyses and Modeling of Swarming Behavior

Butail et al. obtained three-dimensional positions and velocities of swarming mosquitoes from stereoscopic video sequences and described the oscillatory motion of male mosquitoes in the swarm [23] using the dynamic model of Okubo [22]. Evidence for interactions in mosquito swarms was suggested in [23] by analyzing the velocity disagreement between neighbors. Inspired by studies of neural networks that show incidence of correlated signals [62], we analyze the interaction networks in a mosquito swarm using the unit-velocity cross correlation to classify mosquito pairs as interacting or non-interacting. Section 2.2 proposes a procedure to define a threshold on the correlation value to detect whether a given pair of mosquitoes are interacting or not. Section 2.2 presents how the correlation threshold combined with the lag analysis generates instantaneous interaction graphs, which show that the male mosquitoes form subgroups whose size and membership change rapidly. Section 2.3 improves an existing particle model by including local interactions represented by damping

of relative velocity between males. The chapter concludes with some discussions of the results.

2.1 Correlation Function

Cross correlation [3,4] measures the similarity between two signals taking time delay or lag into account. The cross correlation value of two discrete, scalar signals $f(t)$ and $g(t)$ with time lag m is $r_{fg}(m) = \sum_{t=-\infty}^{\infty} f(t+m)g(t)$. Maximum correlation at a positive lag m indicates that f is lagging behind g . We use as signals the three-dimensional velocity \mathbf{v} of each mosquito obtained from stereo-video tracking in the field [23]. Let T_w be an even integer that specifies the time window in which we calculate the correlation value and \cdot denote the vector inner product. The velocity cross correlation of mosquito i and j at time t with lag m is

$$\tilde{R}_{ij}(m, t; T_w) = \frac{1}{T_w + 1} \sum_{n=-T_w/2}^{T_w/2} \mathbf{v}_i(t + n + m) \cdot \mathbf{v}_j(t + n). \quad (2.1)$$

When $T_w = 0$, $\tilde{R}_{ij}(m, t) = \mathbf{v}_i(t + m) \cdot \mathbf{v}_j(t)$ represents an instantaneous measure of correlation; when $T_w \geq 2$, $\tilde{R}_{ij}(m, t)$ is averaged over $T_w + 1$ video frames. Since we wish to know at each instant whether a given pair of mosquitoes is interacting, the instantaneous correlation $T_w = 0$ is problematic because it fails to reject incidental velocity alignment. (Further details for choosing T_w are described in the sequel.)

The cross correlation (2.1) is positive when the angular disagreement in the direction of motion is less than $\pi/2$ radians; otherwise it is negative. The value (2.1) is also affected by flight speed in the following sense: the (absolute value of) \tilde{R}_{ij} is

large when either insect is flying at high speed, even if the direction of motion is not well aligned. In order to focus on the directional alignment, we consider the unit velocity $\hat{\mathbf{v}} = \mathbf{v}/\|\mathbf{v}\|$ of each mosquito and define the unit-velocity cross correlation as

$$\tilde{r}_{ij}(m, t; T_w) = \frac{1}{T_w + 1} \sum_{n=-T_w/2}^{T_w/2} \hat{\mathbf{v}}_i(t + n + m) \cdot \hat{\mathbf{v}}_j(t + n). \quad (2.2)$$

The unit-velocity cross correlation (2.2) takes values in the range $[-1, 1]$; the value $+1$ (resp. -1) occurs when the direction of motion is completely parallel (resp. anti-parallel) throughout the time interval of length T_w . Figure 2.1 illustrates the calculation of the unit-velocity cross correlation. Although the unit-velocity cross correlation ignores speed (velocity magnitude), its value is easier to interpret than the velocity cross correlation because it represents the degree of alignment in the direction of motion.

The correlation value $C_{ij}(t)$ between mosquito i and j at time t with a time window T_w is calculated using (2.2) as follows:

$$C_{ij}(t) \triangleq \tilde{C}_{ij}(m^*, t; T_w) = \frac{1}{2} \left(\tilde{r}_{ij}(m^*, t; T_w) + \tilde{r}_{ji}(-m^*, t; T_w) \right), \quad (2.3)$$

$$\text{where } m^* = \arg \max_{|m| \leq m_{\max}} \tilde{C}_{ij}(m, t; T_w). \quad (2.4)$$

Taking the mean of \tilde{r}_{ij} and \tilde{r}_{ji} ensures the relation between i and j is consistent, i.e., i and j do not lag behind each other at the same time. The parameter T_w affects the correlation value in various ways. First, it specifies the number of the data points used to find the similarity between the direction of motion of two mosquitoes.

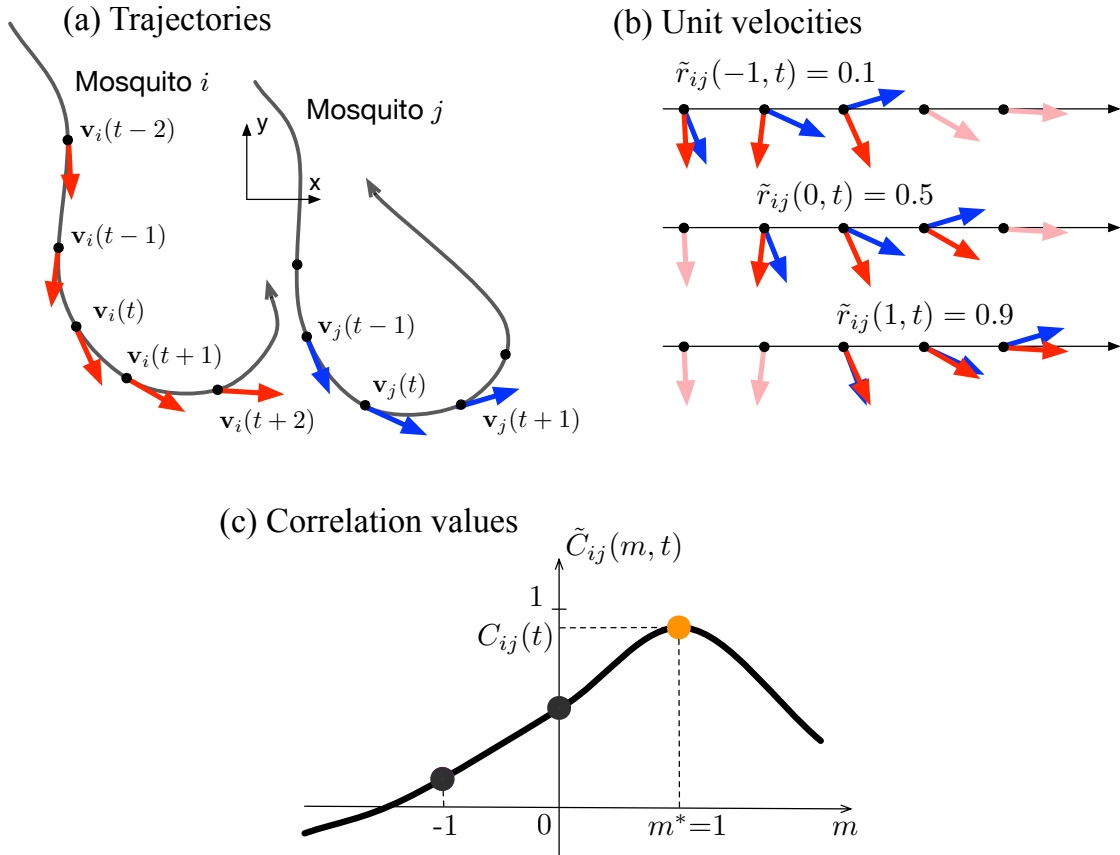


Figure 2.1: Calculation of unit-velocity cross correlation. (a) Two hypothetical flight trajectories and direction of motion projected on a plane (actual calculation is performed with three-dimensional velocities). (b) Calculation of cross correlation (2.3) between i and j with $T_w=2$, using three data points from each trajectory (actual calculation is performed with $T_w=10$). Cross correlation between \mathbf{v}_i and \mathbf{v}_j at time t is shown for lags $m = -1, 0$, and $+1$. (c) Determining the optimal lag m^* and cross correlation \tilde{r}_{ij}^* by choosing the peak from $\tilde{r}_{ij}(m, t)$. A positive lag indicates that i is following j .

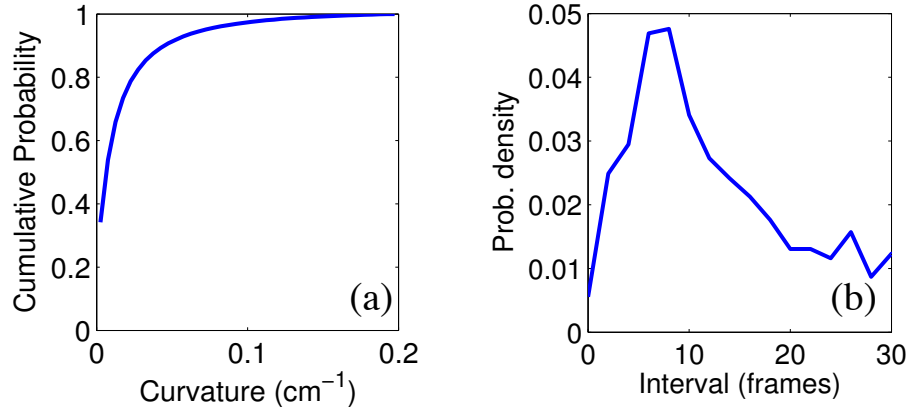


Figure 2.2: Interval between tight turns. (a) Cumulative probability of curvature value. (b) Interval between tight turns. A tight turn is defined as a turn with curvature greater than $0.1 \text{ (cm}^{-1}\text{)}$. The peak is at 8 frames (0.32 s).

Therefore, a smaller value of T_w leads to a higher risk of detecting accidental coordination. Second, since we average the value over $T_w + 1$ frames, the true correlation may be suppressed if we choose T_w to be too large. Considering these two points, we base the choice of T_w on the frequency of the flight turns that the males make. Figure 2.2-a shows the cumulative probability of the curvature in a male’s flight trajectory. Using this figure, we set a threshold of $0.1 \text{ (cm}^{-1}\text{)}$ on the value of the curvature to define tight turns. Figure 2.2-b shows that the interval between tight turns so defined has its peak probability at 8 frames (0.32 s). We choose $T_w = 10$ frames (0.40 s) so that these turning flights are typically included in every sliding time window.

Recall that m^* is the lag value that maximizes the correlation value. We set two restrictions on the optimal lag m^* when we search for the maximum in (2.4). First, to avoid erroneous correlation, we set an upper and a lower bound on m^* given by $m_{\max} = 4$ frames (0.16 s), based on the frequency of the tight turns as

described above. Second, since the optimal m^* in terms of matching two signals should be a critical point in the curve of $\tilde{C}_{ij}(m, t)$ as in Figure 2.1-c, we restrict the candidates for m^* to those m that achieve local maxima. When there are multiple local maxima, we use m^* with the largest $\tilde{C}_{ij}(m, t)$ among those candidates; when there is no critical point within the range $[-m_{\max}, m_{\max}]$, then we use the value $m^* = 0$.

2.2 Interaction Network

This section introduces a procedure to define a threshold on the correlation value to define whether a given pair of mosquitoes are interacting or not. We then characterize the features of pairwise interaction network.

2.2.1 Induced Interaction Graph

The unit-velocity cross correlation measures the degree of interaction (if any) between two mosquitoes according to the alignment in their direction of motion. Figure 2.3 shows the probability density for the correlation values taken from 8 swarms of *An. gambiae* (approximately 450,000 data points). These data are compared to simulated data from a random-walk model, to simulated data from a swarming model without interaction, and to field data from 8 male-female coupling events (about 200 data points). Construction of the simulated swarm is described in Section 2.3.

Comparing the simulated swarm and the real swarm to the simulated random walk, we see that the first two have their peak-probability correlation values near

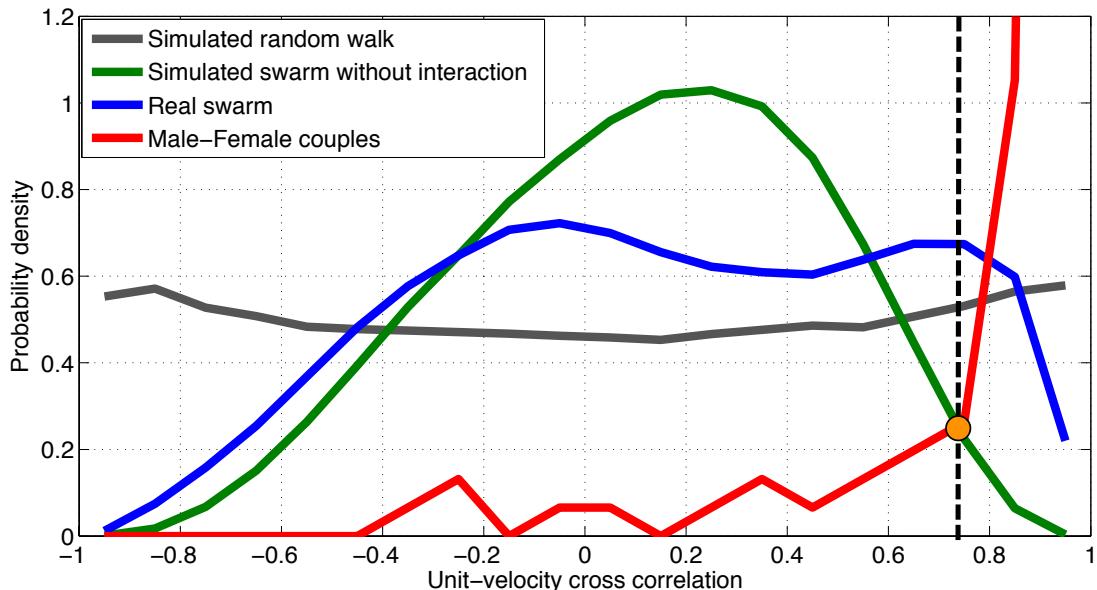


Figure 2.3: Frequency distribution of correlation values for real and simulated swarms. Unit-velocity cross correlation probabilities calculated for 8 real swarms and 8 coupling flights, normalized to have unit integral. The vertical dashed line passing through the orange dot indicates the threshold for interaction. The area under each curve to the right of the threshold shows the proportion of the pairs that are classified as interacting.

zero, whereas the latter has an almost uniform distribution in the interval $[-1, 1]$.

Although the simulated swarm without interaction captures some of the features of the real swarm, the real swarm exhibits an elevated probability of high correlation values compared with the simulated swarm. To detect interactions, we define a threshold on the correlation value inspired by Bayes decision rule [63], using the intersection at 0.75 of the green curve (simulated swarm without interaction) and the red curve (male-female couples). This choice ensures the minimum error rate in classification, assuming that it is equally probable for a pair of mosquitoes to be interacting or not [63]. We label pairs that have a correlation value greater than the threshold as interacting; otherwise we label them as non-interacting.

For an interacting pair, a nonzero lag value m^* that maximizes the correlation indicates an instantaneous following behavior [4]. A positive lag for C_{ij} (or a negative lag for C_{ji}) indicates that mosquito i is following the motion of mosquito j . (Note that this does not necessarily imply i is chasing j ; simply that i is matching its direction of motion to that of j .) The interaction lag analysis, combined with the cross-correlation threshold, induces a directed graph [4] that describes the instantaneous interaction topology in the swarm. Each node represents a mosquito and the edges are directed towards the followers. Figure 2.4-a depicts the instantaneous interaction graph for a real swarm. Figure 2.4-b depicts the interval graph [64]. Note that, although males in the simulated swarm are not directly interacting, pairs with correlation value above the threshold are misclassified as interacting; the area under the green curve above the threshold, which corresponds to the misclassified data, accounts for less than 2% of the area under the curve.

2.2.2 Features of Pairwise Interaction Network

Here we analyze the characteristics of the interactions that occur between pairs of males in the *An. gambiae* swarms, as well as the subgroups that are defined by those pairwise interactions. Figure 2.5-a plots the probability density of the distance between all pairs of males. The curve for interacting pairs lies to the left of the curve for non-interacting pairs, which indicates that an interacting pair is likely to fly closer together than a non-interacting pair. Figure 2.5-b shows the neighbors with which each male is interacting, sorted by their relative proximity. When a

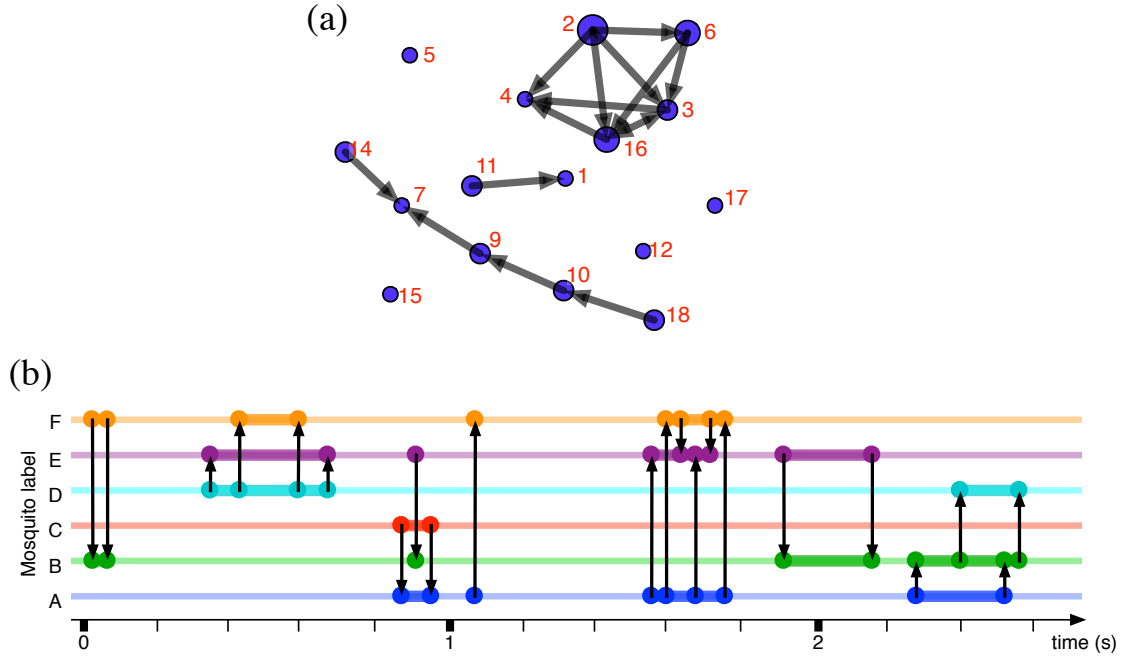


Figure 2.4: Visualization of interaction network. (a) Visualization of interaction graph generated by software “SoNIA” [McFarland, D., BenderedeMoll, S., *SoNIA: Social Network Image Animator*. Available from <http://www.stanford.edu/group/sonia>]. The figure shows an instantaneous interaction graph. Each node represents a mosquito and each edge directed towards a follower represents an interaction. The size of a node is proportional to the number of incident edges originating from it. Note that the distance in this figure does not represent Euclidean distance. Nodes without edges are located randomly. (b) Interval graph. Directed edges are shown at the starting and the ending point of each pairwise interaction. The thick line indicates that the mosquito is in an interacting state.

male is interacting with more than one other male at the same time, the plot shows the one with the greatest correlation value. The probability of interaction decreases as the neighbor number increases. Figure 2.5-c shows the duration of interaction (i.e., the period of time that the correlation value stays above the threshold). The resolution of this analysis is equal to the video frame rate (0.04 s).

Consider a subgroup of a swarm to be defined as the weakly connected component of an interaction graph induced as in the preceding section. A weakly connected component is a set \mathcal{V} of nodes that are connected to each other by edges; treating

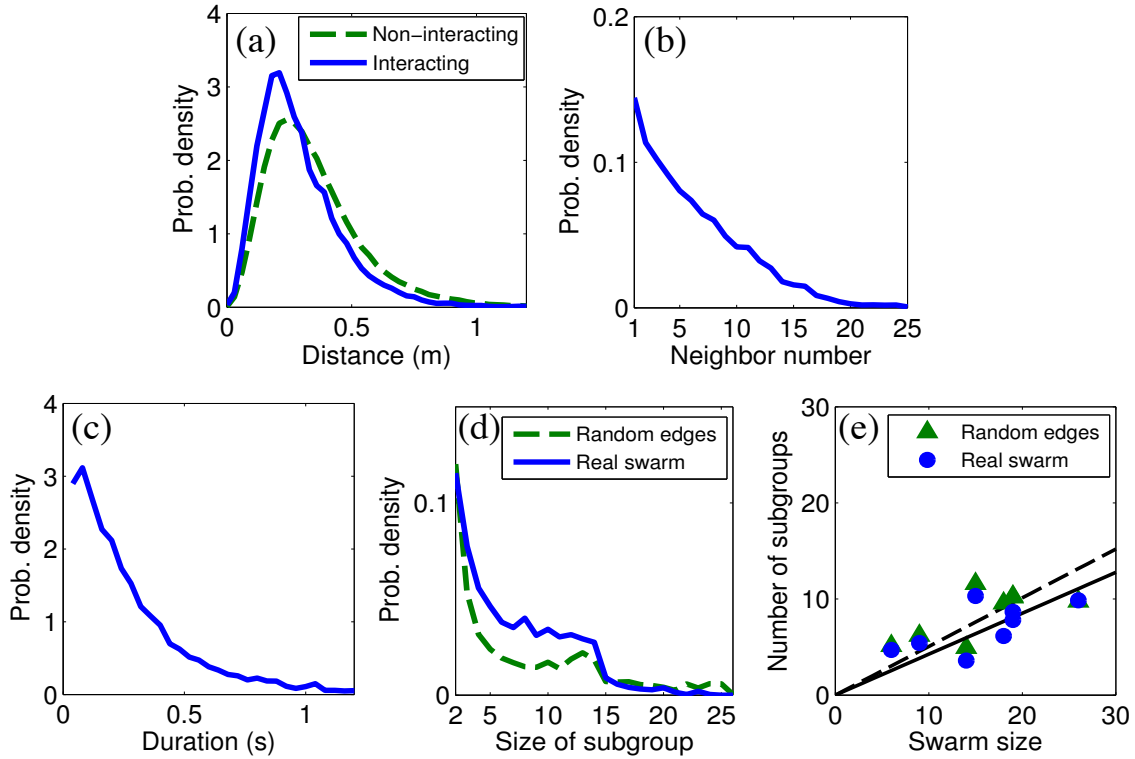


Figure 2.5: Features of interaction and network. (a), Probability density of distance between two males, for interacting and non-interacting pairs. (b), Probability of interacting with k th-neighbor. (c), Duration of interaction, i.e., the period of time that the correlation value stays above the threshold. (d), Probability of the size of subgroup in which a male may be included at each moment for subgroup sizes greater than one. The result is compared to a reference null model with randomized edges [64]. (e), Number of subgroups versus swarm size with linear regression passing through the origin.

the edges as undirected, each node in \mathcal{V} is reachable from any other node in \mathcal{V} [65].

For example, if i is following j and j is following k , then $\{i, j, k\}$ are in the same subgroup. If i and j are both following k , they are also in the same subgroup.

Figure 2.5-d shows the instantaneous probability of the subgroup size in which a male may be included omitting subgroup size 1, which corresponds to no interaction. In order to find the type of subgraph that is overrepresented in the mosquito swarm, called a motif [64], compare the result to a randomized edges model; in this

model the connected pairs are randomly shuffled while the number of edges at each time remains the same as in the real data. Figure 2.5-e shows the number of subgroups versus swarm size in 8 swarm sequences (regression slope = 0.427, adjusted $R^2 = 0.612$).

2.2.3 Differences between Species

Along with data on 8 swarms of *An. gambiae*, we have sequences of positions from 3 swarms of *An. coluzzii*, formerly known as the *Anopheles gambiae* M form [11]. We performed the same unit-velocity cross correlation analysis of the flight data from *An. coluzzii*, and compared the results with those from *An. gambiae*. In order to test whether the difference in the species affects the degree of male-male interactions, we used a linear regression model with the proportion of time each male spends interacting with other males as the response variable; the species and the mean swarm size were fixed effects. Data were averaged over entire swarms. Table 2.1 indicates a significant positive relationship between swarm size and the proportion of time individuals spent interacting but no significant differences between the species. An interaction term for the fixed effects was included in a separate model but found to be not statistically significant (results not shown).

Table 2.1: Linear regression model. The effect of the species and swarm size on the proportion of time each male spends interacting with another male. Standard error (SE), t -statistics (t), and p -values (p) are shown.

source	value	SE	t	p
Intercept	0.239	0.145	1.643	0.139
Species	-0.106	0.108	-0.976	0.358
Mean Swarm Size	0.025	0.009	2.772	0.024

Residual SE = 0.155 (8df); Adjusted $R^2=0.469$; Model $F_{2,8} = 5.418$; $p = 0.033$

2.3 Swarm Model

This section studies self-propelled particle models to characterize the swarming behavior of male mosquitoes. First, we introduce an existing swarming model without interaction, which was used in the previous section to find the threshold in the correlation value. We then propose a new swarming model which reproduces the velocity-alignment interaction. Model parameters are optimized to fit to swarming data from real swarms.

2.3.1 Simulated Swarm Model without Interaction

Consider a system of point particles with unit mass. Let \mathbf{r}_i , \mathbf{v}_i , and \mathbf{a}_i be the position, velocity, and acceleration of mosquito i with respect to an inertial point O . Following [22], we model the force on mosquito i as a linear combination of the external force $\mathbf{F}_i^{(\text{ext})}$, the drag force $\mathbf{F}_i^{(\text{drag})}$, and the interaction force $\mathbf{F}_i^{(\text{int})}$, i.e.,

$$\mathbf{a}_i = \mathbf{F}_i^{(\text{ext})} + \mathbf{F}_i^{(\text{drag})} + \mathbf{F}_i^{(\text{int})}. \quad (2.5)$$

Velocity fluctuation is modeled as a damped oscillator [23]; the frequency and damping ratio are obtained from the velocity autocorrelation. Based on this previous analysis, we model the first two components in (2.5) as resulting from a damped spring that connects the mosquito to the centroid of the swarm. Let $\hat{\mathbf{r}}_i = \mathbf{r}_i / \|\mathbf{r}_i\|$. Assuming the centroid is fixed in an inertial frame (only approximately true in real data), then we can without loss of generality attach the spring to the point O , i.e.,

$$\mathbf{F}_i^{(\text{ext})} + \mathbf{F}_i^{(\text{drag})} = -\text{diag}\{\mathbf{k}\}\mathbf{r}_i - \text{diag}\{\mathbf{b}\}(\mathbf{v}_i \cdot \hat{\mathbf{r}}_i)\hat{\mathbf{r}}_i. \quad (2.6)$$

The parameters \mathbf{k} and \mathbf{b} denote the three-dimensional spring constants and the damping constants, respectively; since they are vector quantities, the spring can have different constants in each direction (e.g., down-wind, cross-wind, and vertical) [23]. Since we do not know the internal interaction force, we assign white noise as the third component, i.e., $\mathbf{F}^{(\text{int})} = \mathbf{W}$, where the random process $\mathbf{W}(t)$ has the autocorrelation $R_{\mathbf{W}}(\tau) = \mathbf{A}\delta(\tau)$. The intensity \mathbf{A} of the white noise was determined in [23]. We discretize $\mathbf{W}(t)$ in the numerical integration with the integration time step $\Delta t = 0.04$ (s), equal to the video frame rate.

2.3.2 Simulated Swarm Model with Interaction

The dynamic swarming model (2.5)-(2.6) is based on a damped, spring-like force between each insect and the swarm centroid. Although a central-force model reproduces the cohesive motion of males in the swarm, it does not match the unit-velocity cross correlation probability density of the real swarms (see Fig. 2.3). In order to

model coordinated behavior through velocity alignment, we introduce a damper between interacting males. Let \mathcal{S}_i denote the set of mosquitoes that mosquito i are interacting with, and \mathbf{W} denote white noise with zero mean and intensity \mathbf{A} . Let $\mathbf{r}_{j/i} = \mathbf{r}_j - \mathbf{r}_i$, and $\hat{\mathbf{r}}_{j/i} = \mathbf{r}_{j/i}/\|\mathbf{r}_{j/i}\|$. The interaction force model is

$$\mathbf{F}_i^{(\text{int})} = \lambda \sum_{j \in \mathcal{S}_i} b^{\text{int}} (\mathbf{v}_{j/i} \cdot \hat{\mathbf{r}}_{j/i}) \hat{\mathbf{r}}_{j/i} + (1 - \lambda) \mathbf{W}. \quad (2.7)$$

The gain $\lambda \in (0, 1]$ creates a convex combination of the damping force and the random force when mosquito i is in the interacting state; $\lambda = 0$ eliminates the damping term when it is in the non-interacting state. When two particles are connected by a velocity damper, it decreases the relative velocity between them and increases the velocity alignment. Figure 2.6 illustrates the augmented swarming model.

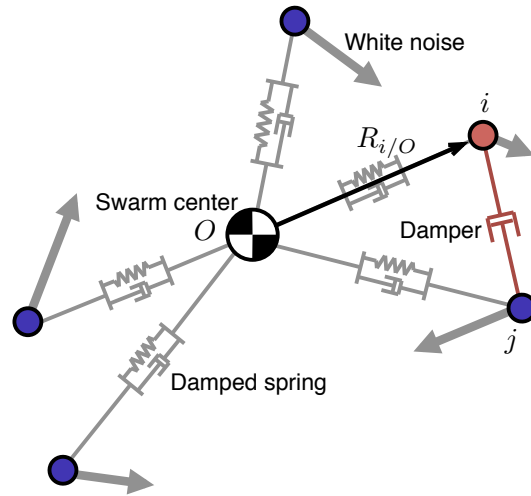


Figure 2.6: Illustration of the augmented swarming model with five males. All five are connected to the swarm centroid by a damped spring. At the instant shown, male i is in the interacting state and is subject to the (uni-directional) force from the damper connected to j ; the random force is weakened proportionally. Male j does not feel this damper force.

The interaction topology is determined as follows: males interact if the disagreement in the direction of their motion is less than the threshold 0.75; one is picked randomly to be the follower for the duration of interaction. The remaining model parameters are the damping constant b^{int} and the gain λ . We used a probabilistic search method called simulated annealing [66] to obtain the values of b^{int} and λ that best fit the real swarm in terms of the correlation probabilities. Table 2.2 shows the parameters that are used in the simulation model. Note that fitting the model to each of the 8 real swarms yields a unique set of parameters. Table 2.2 shows the mean and standard deviation of the parameter values from all 8 *An. gambiae* swarms.

Table 2.2: Parameters for the swarm simulation. The four parameters at the bottom are used only in the new simulation with interaction. Three components in each of \mathbf{k} and \mathbf{b} correspond to the values used for down-wind, cross-wind and vertical direction, respectively.

	mean	SD	units
Cohesive motion			
mass of mosquito	$m = 1$	N/A	kg
rest length of spring	$l_0 = 0$	N/A	m
spring constants	$\mathbf{k} = [35, 27, 10]$	$\pm[23, 20, 21]$	N/m
damping constants	$\mathbf{b} = [5.4, 4.5, 5.4]$	$\pm[2.0, 1.5, 2.7]$	N·s/m
integration time step	$\Delta t = 0.04$	N/A	s
intensity of random forcing	$\text{diag}\{\sqrt{\mathbf{A}}\} = [9.0, 11.0, 5.5]$	$\pm[6.5, 7.1, 4.6]$	N
Interaction			
damping constant for interaction	$b^{\text{int}} = 116$	± 66	N·s/m
threshold for velocity alignment	$r^* = 0.75$	N/A	
gain of damping term	$\lambda = 0.73$	± 0.12	

Figure 2.7 shows the unit-velocity cross correlation of the simulation model with interaction, which has elevated probability of high values as compared to the model without velocity damping. Nonparametric Kruskal-Wallis comparison of the mean squared error, E , between the probability distributions of real and simulated

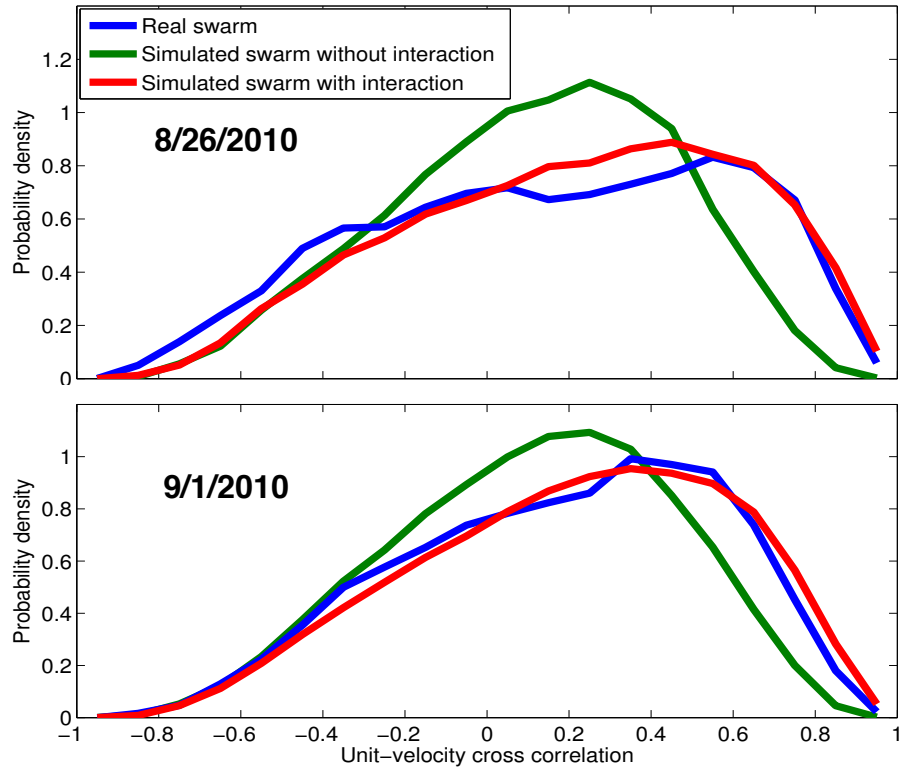


Figure 2.7: Model fit to swarming data from two real swarms of *An. gambiae*. The simulated swarm with interaction (red) fits the real data better than the original swarming model without interaction (green).

data for the 8 swarms reveal a significant reduction in error ($p = 0.011$, $\chi^2 = 6.35$) from using the model without interaction ($E = 0.072 \pm 0.06$) to the new model with interaction ($E = 0.024 \pm 0.02$).

2.4 Discussion

The results presented in this chapter strongly support the hypothesis that there is significant male-male interaction in mating swarms of *An. gambiae* and *An. coluzzii* and that these interactions go beyond simple collision avoidance. Indeed, there is regular occurrence of parallel flight between pairs and within subgroups of swarming

males. This observation and the basis and function of male-male interactions have important implications on the origins of swarming behavior and for mating in these species.

Observed parallel flight behavior may result from velocity-matching behavior by each male. It is possible that males would perform velocity-matching to any nearby flying insect in a swarm to allow mate recognition via wingbeat frequency matching [67] or potentially volatile pheromone communication, though as yet there is no evidence of the latter [68]. In mating swarms, behavioral sequences leading to insemination may be initiated by a couple matching their velocities.

A second possibility is that the observed interactions represent a means of obtaining information on what may be occurring in a part of the swarm outside an individual's perceptive range. For example, if a female enters the swarm at a point distant from a given male, but other males are responding to her by altering their flight patterns, then information may be transmitted from male to male by velocity matching. Such a scenario may be amenable to further analysis via information theory [69]; interestingly, males nearest to the female should be disadvantaged by communicating that fact, so data transmission in the context of the swarm may be viewed as detrimental for the transmitter but beneficial for the receiver.

A third interpretation of the interactions in the swarm is that males are competing for space in the lek, so that parallel flight is a form of ritualized aggression [70] between males, as is observed in the dragonfly *Plathemis lydia* [71]. Early theories of lek formation included elements of male-male competition (see review in [72]). However, this hypothesis is opposed by limits to the visual acuity of *An. gambiae* and

An. coluzzii and by the lack of observation of individual territories even including the denser swarm centroid [23, 73].

An important contribution of the current work is the improved model of male *An. gambiae* swarming over the previous approach [23]. The model presented here (see equations (2.5), (2.6), and (2.7)) includes a term representing male-male interaction: velocity correlation between males is initiated randomly, but once it occurs individuals attempt to maintain a high correlation. Incorporation of male-male interactions in an improved mathematical characterization of the swarms significantly improves the statistical fit of the model to real swarm data. Therefore the new model provides a better null hypothesis against which to test deviations from normal swarming behavior.

Male-male interactions were not found to vary significantly between species. It has been generally observed that *An. coluzzii* males swarm over markers of contrast on the ground, such as a well or a pile of refuse, whereas *An. gambiae* males swarm over bare ground [12, 72]. In this respect, the degree of male-male interaction might be expected to vary between these species [74], since the external marker may serve as an attractor. As a result, one might predict that a higher degree of male-male interaction is required to maintain swarm cohesion for *An. gambiae*, which do not swarm over a marker in our study area, compared with *An. coluzzii*, which do. While our analysis does not support this prediction, it is possible that a better test would require a larger data set on *An. coluzzii*, similar to the one we collected for *An. gambiae*.

Genetic control of the degree of velocity matching may be through one or a

few linked loci and thus be a trait that can drive the speciation in the *An. gambiae* complex [75], in this case between *An. gambiae* and *An. coluzzii*. The genetic basis of male-male interaction will also be critical for any release-based program of malaria vector control such as one based on Sterile Insect Technique [76] or Genetic Modification [77]. Such releases will almost certainly involve colony-reared males that will have to successfully inseminate wild females, probably by mating with them in swarms. Therefore understanding and regulating the genetic basis of swarming behavior for these purposes may be critical to these programs. Future experiments could include correlations between swarming behaviors and genetics to elucidate the link between the two.

Chapter 3

Analyses and Modeling of Pursuit and Coupling Behavior

This chapter analyzes the eight data sets that include female mosquito, to study the pursuit and coupling behavior in mosquito swarms. Section 3.1 shows how male's behavior changes when the distance to the female becomes small, which we call the *close encounter*. Section 3.2 focuses on the phase right before the close encounter, and studies who is closing the distance, i.e., whether it is the male or the female who is initiating the close encounter. Section 3.3 focuses on the phase after the close encounter, and analyzes the coupling flight of the male and female. We model their relative motion as a damped-spring system with time delay, and analyze how the control gains (spring and damping constants) are modulated when they switch from swarming to coupling behavior. Inspired by the analyses of mosquito flight data, Section 3.4 extends the particle model introduced in Chapter 2 by including a particle that represents a female mosquito. The model generates three different behaviors (swarming, velocity alignment, and pursuit) by switching the model

parameters. Section 3.5 performs Lyapunov analysis of the new swarming model to study the stability of the velocity-alignment interaction that generates intermittent parallel flight studied in Chapter 2. We also study how the velocity-alignment behavior may help male’s success in pursuing the female.

3.1 Switching in Male’s Behavior

A mating swarm of mosquitoes consists almost entirely of males, and a female approaches and passes through the swarm several times until it forms a couple with a male. In the video sequences of the swarming mosquitoes, couples were found based on its size in the image [78]. By following the couples backward in time to the point when they formed, the female and its mate were identified. These two individuals were further traced backwards in time to the point where one of them had entered the field of view and the other was already a member of the swarm. The former is the female and the latter is a male which we term the *focal male*—the male who mated in the given sequence (Nicholas C. Manoukis, personal communication, July 20, 2015).

When the female moves in and out of the swarm, its velocity is higher than the males. During this phase, males do not appear to respond to the presence of the female, which we call the *swarming* phase or the *search* phase. However, once the distance to the female becomes small, which we call the *close encounter*, the male accelerates to match its velocity with the female and starts the *pursuit* (or *coupling*) phase. Figure 3.1 shows an example of the speed of a female and focal male, and the

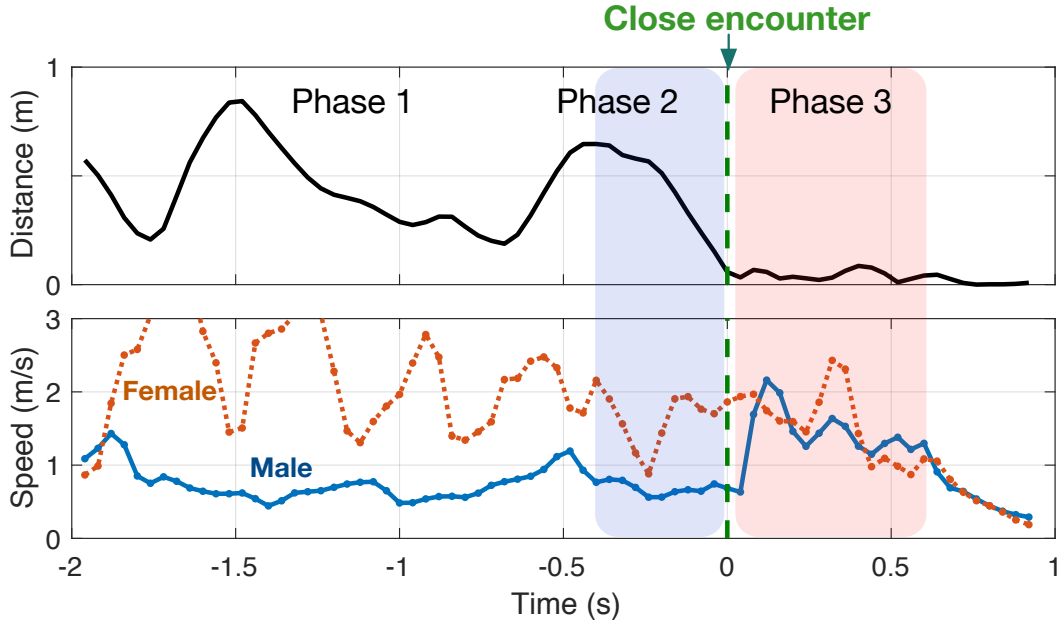


Figure 3.1: Time history of the distance and speed during the coupling flight. Close encounter is defined to be the time when the distance between the male and female becomes small for the first time, which is followed by the increase in male’s speed. Phase 1 is the swarming (or searching) phase. Phase 3 is the pursuit (or coupling) phase. Phase 2 is the transition between phases 1 and 3. The distance decreases during Phase 2, which leads to the close encounter.

distance between them. The time axis is shifted so that the close encounter occurs at 0 (s). The male’s speed increases rapidly after the close encounter, whereas the female’s speed decreases as compared to the search phase.

We have so far introduced two phases—swarming and coupling—that are labeled as Phase 1 and Phase 3 in Fig. 3.1. However, we are also interested in the mechanism that generates the close encounter between the female and the focal male, i.e., the transition between phases 1 and 3. To study this transition, we define Phase 2 to be the duration of time when the distance between the male and the female is decreasing prior to the close encounter. Note that if the close encounter occurs by pure chance, then Phase 2 does not exist, i.e., the transition from Phase 1

to Phase 3 occurs suddenly by chance. Assuming that either the female or the male (or both) is closing the distance intentionally, we study the pursuit behavior in Phase 2 next.

3.2 Initiation of Close Encounter

This section focuses on Phase 2, i.e., the transition between the swarming phase and the coupling phase (see Fig. 3.1). Assuming that the close encounter does not occur by pure chance, we first study who is initiating the close encounter—does the female approach the male, or the male approaches the female? To answer this question, we study the relation between the velocity vector and the relative position vector, in the context of some existing notions of pursuit.

3.2.1 Classical Pursuit

The first notion of pursuit we consider is called classical pursuit [79]. In classical pursuit, the pursuer’s velocity is directed towards the target. For example, if the male is the pursuer, then \mathbf{v}_M is directed from M to F (see Fig. 3.2). Classical pursuit does not require the pursuer to know the target’s velocity or absolute position, only its relative position. We use the dot product \cdot to

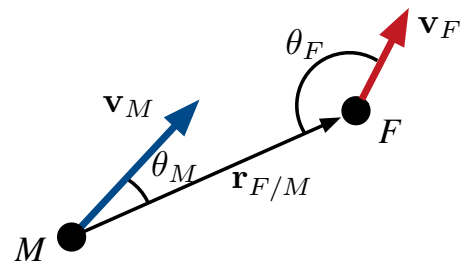


Figure 3.2: Illustration of the vectors and angles used to define the classical pursuit metric.

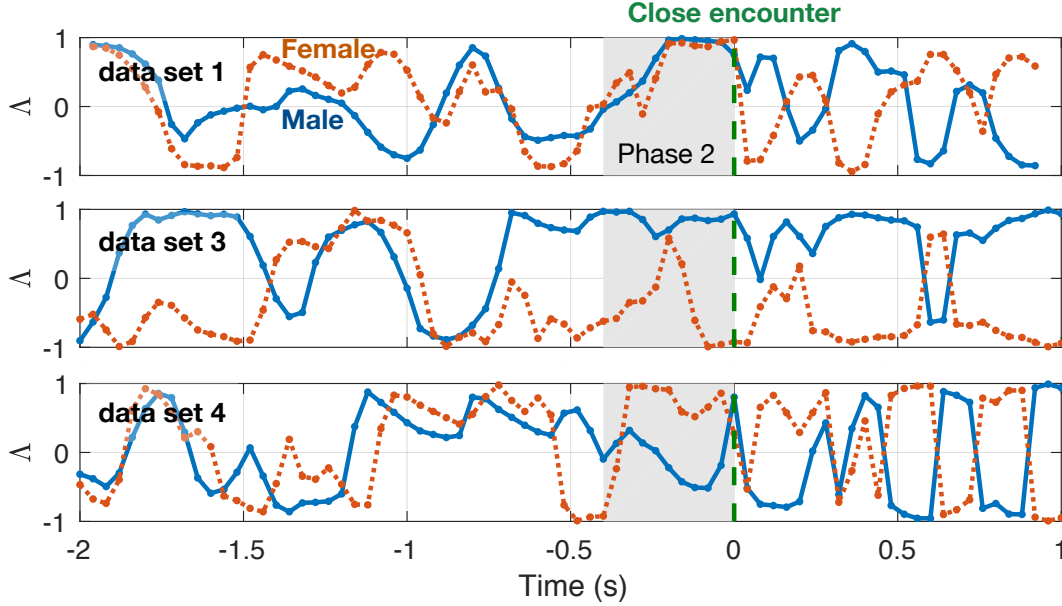


Figure 3.3: Time history of the metric for classical pursuit. Examples from three data sets are shown here. Phase 2 is shaded in grey. The three data sets support hypotheses of mutual pursuit, male pursuit, and female pursuit, respectively.

define a metric for classical pursuit. A metric for male pursuit is

$$\Lambda_{MP} = \frac{\mathbf{v}_M}{\|\mathbf{v}_M\|} \cdot \frac{\mathbf{r}_{F/M}}{\|\mathbf{r}_{F/M}\|} = \cos \theta_M,$$

where $\theta_M \in [0, \pi]$ is the angle between the velocity vector and the relative-position vector. The male-pursuit metric satisfies $\Lambda_{MP} \in [-1, 1]$, where positive values support a hypothesis of male pursuit. (Negative values support a hypothesis of male evasion.) Similarly, a metric for female pursuit is

$$\Lambda_{FP} = \frac{\mathbf{v}_F}{\|\mathbf{v}_F\|} \cdot \frac{\mathbf{r}_{M/F}}{\|\mathbf{r}_{M/F}\|} = \cos \theta_F,$$

and positive values of Λ_{FP} support a hypothesis of female pursuit.

Figure 3.3 shows the time history of Λ_{MP} and Λ_{FP} before and after the close

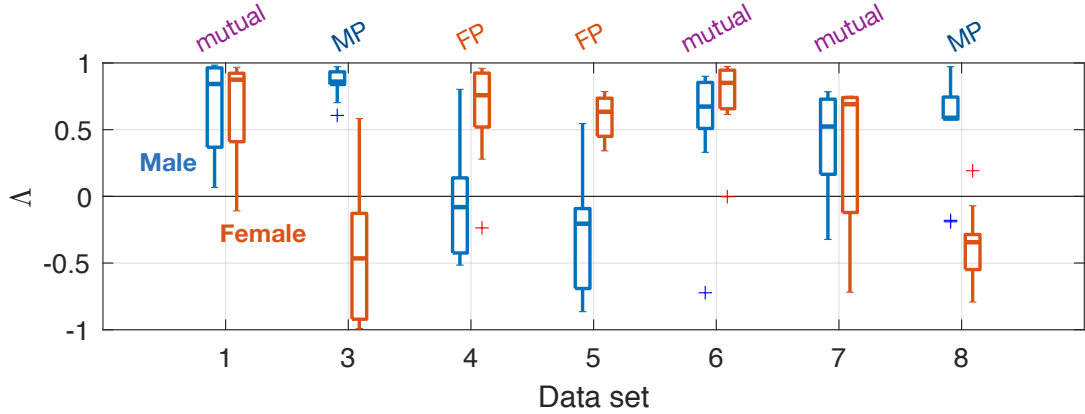


Figure 3.4: Metric for classical pursuit from seven data sets. The directionality of the pursuit (i.e., male pursuit (MP), female pursuit (FP), and mutual pursuit) derived from the data is indicated at the top.

encounter. We define Phase 2 to be the 10 video frames (0.4 s) preceding the close encounter. The duration of 10 video frames is selected based on the timing when the distance between the male and female starts decreasing (see Fig. 3.1). Figure 3.4 shows the statistics of Λ during Phase 2. (Data set 2 is excluded since the female and the focal male were already in the coupling phase (i.e., Phase 3) when they entered the camera field of view.) This analysis shows that there is no dominant direction in the pursuit. More samples of coupling flight are needed to draw a statistically significant conclusion.

3.2.2 Motion Camouflage

The second notion of pursuit that we consider is called motion camouflage [79], which is known to be a stealth strategy observed in nature. The pursuer stabilizes the line of site (LOS) in the inertial frame so that it appears stationary from the perspective of the target. In motion camouflage, the pursuer requires knowledge

of the target’s relative position and relative velocity. Once again, we use the dot product to define the metric for motion camouflage:

$$\Lambda_{MC} = \frac{\mathbf{r}_{M/F}}{\|\mathbf{r}_{M/F}\|} \cdot \frac{\mathbf{v}_{M/F}}{\|\mathbf{v}_{M/F}\|} = \cos \theta_{MC}, \quad (3.1)$$

where θ_{MC} is the angle between the relative-position vector and the relative-velocity vector. Note that this metric does not distinguish between male pursuit and female pursuit.

The motion-camouflage metric satisfies $\Lambda_{MC} \in [-1, 1]$. The LOS is stabilized when $|\Lambda_{MC}| \approx 1$, whereas $|\Lambda_{MC}| \approx 0$ indicates a pure rotation of the relative position vector $\mathbf{r}_{M/F}$. The distance between the male and female is increasing when $\Lambda_{MC} > 0$ and decreasing when $\Lambda_{MC} < 0$. Therefore, the motion camouflage hypothesis is supported by the value $\Lambda_{MC} \approx -1$. Figure 3.5 shows three examples of the time history of the metric Λ_{MC} . It shows that the metric Λ_{MC} stays negative in Phase 2 since the distance is decreasing, and also that the values are often close to -1 , indicating that the LOS is stabilized. Figure 3.6 shows the box plot obtained from the 10 data points during Phase 2 for each mating sequence. The data sets 1, 4, 6, and 7 strongly support the motion camouflage hypothesis. Although the directionality of the pursuit behavior in Phase 2 is unclear, we find an evidence that supports the motion camouflage hypothesis. This result also supports the existence of Phase 2, i.e., the close encounter occurs because either the male or the female is pursuing the other.

Finally, note that the metric Λ_{MC} oscillates rapidly in Phase 3 (see Fig. 3.5)

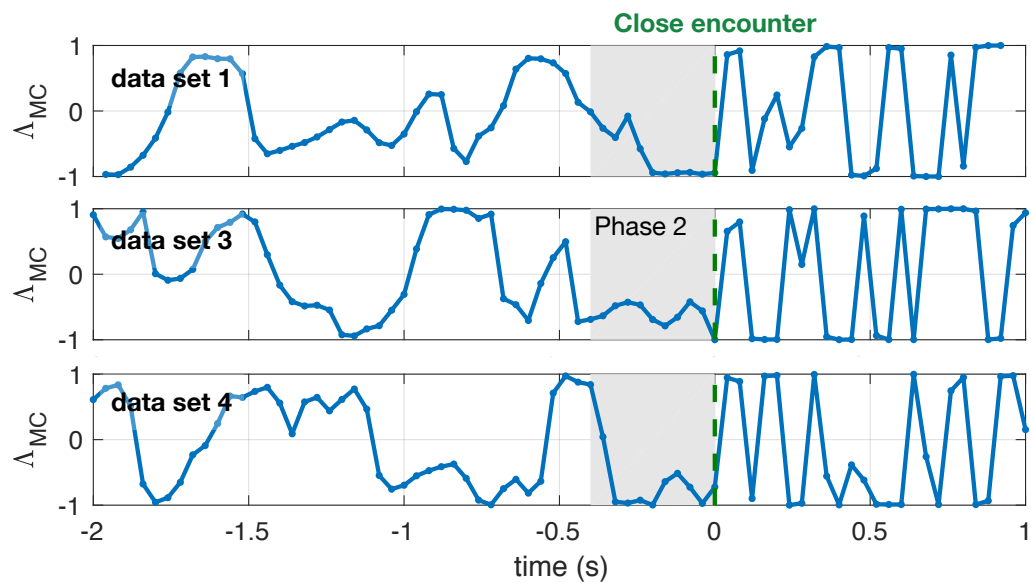


Figure 3.5: Time history of the metric for motion camouflage. Examples from three data sets are shown here. The shaded area depicts phase 2, which is defined to be the ten video frames (0.4 s) prior to the close encounter.

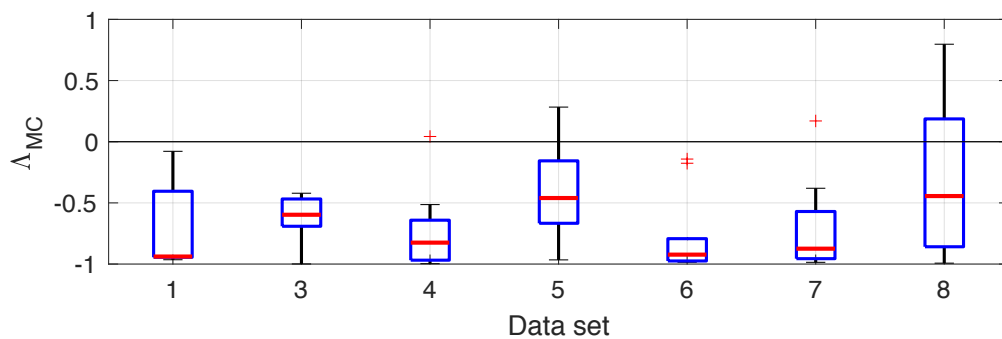


Figure 3.6: Metric for motion camouflage from seven data sets. The data sets 1, 4, 6, and 7 strongly support the hypothesis of motion camouflage with $\Delta_{MC} \approx -1$.

due to the criss-crossing type of motion during the coupling flight. This phenomenon indicates that the analyses of the velocity vector may be inappropriate to study their relative motion during the coupling phase (Phase 3), which motivates our analysis of the acceleration vector next.

3.3 Male-Female Coupling Flight

This section focuses on Phase 3 that comes after the close encounter (see Fig. 3.1). We use acceleration vectors to study the relative motion between the male and the female during their coupling flight. Since the reconstructed flight kinematics only include the positions and velocities, we numerically differentiate the velocity data using the central difference to obtain the acceleration, i.e.,

$$\mathbf{a}(n) = \frac{\mathbf{v}(n+1) - \mathbf{v}(n-1)}{2\Delta t}, \quad (3.2)$$

where n denotes the index of discrete time step (video frame), and Δt denotes the frame rate (0.4 s). Let $\mathbf{a}_{F/M} = \mathbf{a}_F - \mathbf{a}_M$ denote the relative acceleration of the female with respect to the male. We study how the relative acceleration changes as a function of the relative position $\mathbf{r}_{F/M}$ and the relative velocity $\mathbf{v}_{F/M}$. Note that the analysis of the relative acceleration lacks in the information about the directionality (who is pursuing whom), but it is robust to external effects that affect both insects, e.g., wind gust.

During the coupling flight, the male and female fly in approximately the same direction while their separation distance oscillates as though they are connected by

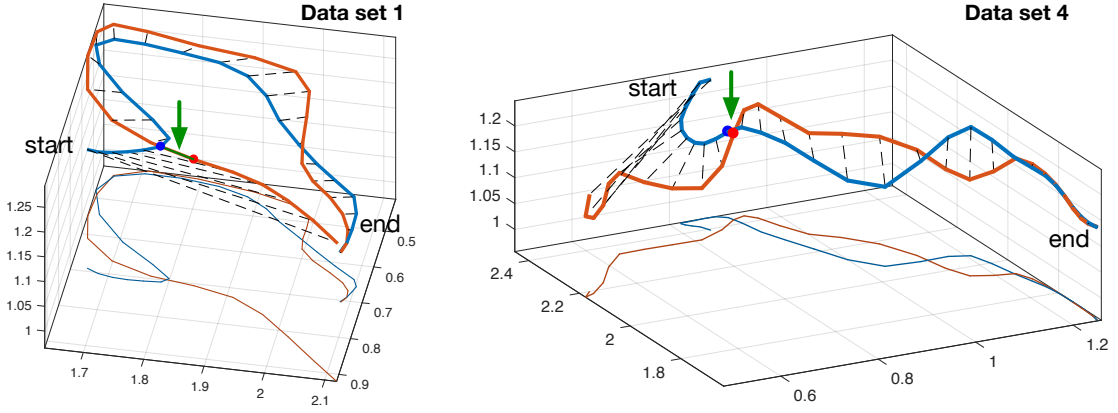


Figure 3.7: Trajectories of the male and female during the coupling flight. Arrows indicate the location of the close encounter.

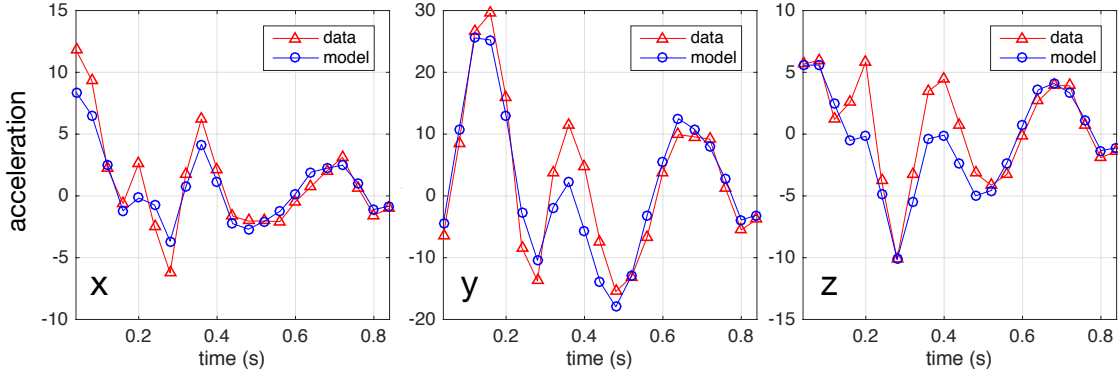


Figure 3.8: Fitted relative acceleration in three orthogonal directions.

a damped spring with zero rest length (see Fig. 3.7). Based on this oscillation, we model the relative acceleration as a force resembling a spring-damper system with time delay, i.e.,

$$\mathbf{a}_{F/M}(t) = -k\mathbf{r}_{F/M}(t - \tau) - b\mathbf{v}_{F/M}(t - \tau) \quad (3.3)$$

where k , b , and τ denote the spring constant, damping constant, and time lag, respectively. Linear regression calculates the parameters k , b and τ for each of eight coupling events. Note that τ is a multiple of 0.04 (s) which is the frame rate of the video sequences. Figure 3.8 shows the comparison between the actual acceleration

data and the acceleration predicted by the model. All eight coupling events have $\tau = 0.04$ (s) as the optimal time lag, and the spring and damping constants are plotted as red crosses in Fig. 3.9-a (adjusted $R^2 = 0.75$).

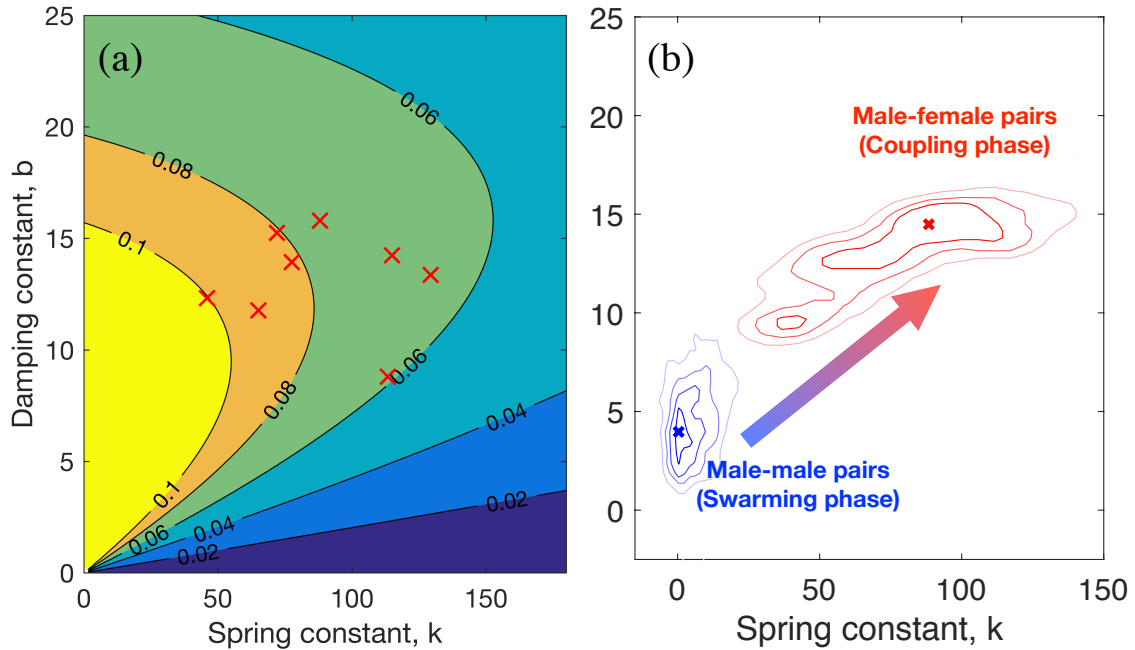


Figure 3.9: Control gains during the coupling flight. (a) The eight crosses depict the parameters (control gains) obtained from linear regression. The contour plot shows the maximum tolerable delay before the system becomes unstable. (b) Probability distribution of the control gains obtained from all eight data sets.

Now, we interpret the parameters k and b as the control gains that the mosquitoes choose. (The gains may be chosen by the male, or the female, or both.) We first study the stability of the delayed system, since time delays often destabilize the system. For the mosquito-couple case, unstable system corresponds to a couple with their separation distance increasing over time. We seek to confirm that the control gains k and b , and the time lag τ (obtained earlier by the linear regression) are consistent in terms of system stability.

Since the model (3.3) is a linear system, the value of the lag that destabilizes

the system can be obtained using techniques from linear systems theory. Here, we use the characteristic equation of the system:

$$f(\lambda) = \lambda^2 + b\lambda e^{-\lambda\tau} + ke^{-\lambda\tau} = 0, \quad (3.4)$$

where the roots $\lambda \in \mathbb{C}$ are the poles of the system (3.3). Although this transcendental equation has infinitely many roots, system stability is guaranteed if they all have negative real parts. The critical case is when there exists an imaginary root $\lambda^* = i\omega$. If we find the smallest time delay $\tau^* = \tau^*(k, b)$ that gives a solution $\omega \in \mathbb{R}$ to the following equation:

$$f(\lambda^*) = f(i\omega) = 0,$$

then we know that all values of τ satisfying $\tau < \tau^*$ give roots with negative real parts (assuming that the system without time delay is stable, i.e., k and b are positive). The contour plot in Fig. 3.9-a depicts the maximum tolerable lag τ^* . Recalling that the optimal time lag obtained from the linear regression is $\tau = 0.04$ (s), the control gains from all eight coupling sequences lie in the stable region, i.e., parameters are consistent in terms of system stability.

Finally, we study how the control gains are modulated when a focal male switches its behavior from swarming to pursuit. We obtain the control gains k and b also from the interacting male-male pairs during the swarming phase. Linear regression is performed for each pair with a moving time window, similar to how we calculate unit-velocity cross correlation in Chapter 2. Figure 3.9-b shows the prob-

ability distribution of the control gains obtained from all eight data sets combined. The gains are smaller during the swarming phase. This result indicates that the focal male may be increasing the control gains of the interaction force when it perceives a female. This switching behavior is included in the new swarming model next.

3.4 Swarm Model with Pursuit Behavior

The goal of this section is to add flexibility to the existing swarming models (see (2.5)–(2.7) in Section 2.3), in order to accommodate, with minimal complexity, the following three behaviors in a single model: swarming, velocity-matching, and pursuit.

3.4.1 Force Model

Consider the following continuous-time, dynamical model of N identical, unit-mass particles subject to forces:

$$\mathbf{a}_i = \mathbf{F}_i^{(\text{space})} + \mathbf{F}_i^{(\text{align})} + \mathbf{F}_i^{(\text{ext})} \quad (i = 1, 2, \dots, N), \quad (3.5)$$

where $\mathbf{F}_i^{(\text{space})}$ and $\mathbf{F}_i^{(\text{align})}$ are the spacing and alignment forces that arise from interactions, respectively, and $\mathbf{F}_i^{(\text{ext})}$ denotes all other external forces, including air resistance and random disturbances. One difference from prior models in Section 2.3 is that here we divide the interaction force, $\mathbf{F}_i^{(\text{int})}$, into two terms ($\mathbf{F}_i^{(\text{space})}$ and $\mathbf{F}_i^{(\text{align})}$) and combine the drag force and unknown disturbance into one term, $\mathbf{F}_i^{(\text{ext})}$.

Let $\mathbf{r}_{j/i} \triangleq \mathbf{r}_j - \mathbf{r}_i$ and $\mathbf{v}_{j/i} \triangleq \mathbf{v}_j - \mathbf{v}_i$ denote the relative position and relative

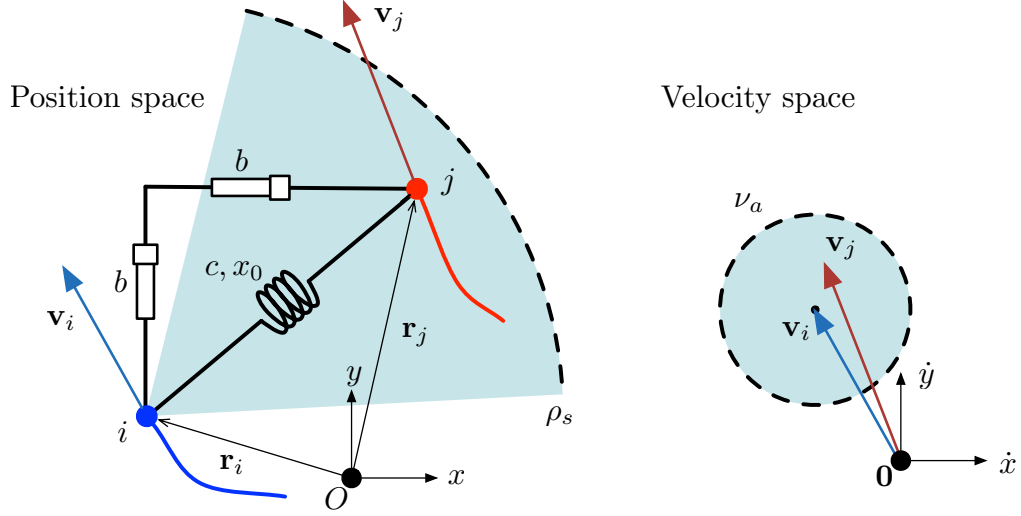


Figure 3.10: Illustration of the model parameters. Particle i is in the velocity alignment state and $j \in Q_a^{(i)}$. The velocity damper produces a force in any direction.

velocity, respectively, of particles i and j in an inertial frame. Let $Q_s^{(i)} = \{k \mid \|\mathbf{r}_{k/i}\| \leq \rho_s\}$ denote the set of particles within the perceptual range $\rho_s > 0$ of the i th particle, and $Q_a^{(i)} = \{k \mid \|\mathbf{v}_{k/i}\| \leq \nu_a, \|\mathbf{r}_{k/i}\| \leq \rho_s\}$ denote the set of particles that are also within interaction range $\nu_a > 0$ in the velocity space. We model each force term as follows:

$$\mathbf{F}_i^{(\text{space})} = c \sum_{j \in Q_s^{(i)}} (1 - x_0 / \|\mathbf{r}_{j/i}\|) \mathbf{r}_{j/i} \quad (3.6)$$

$$\mathbf{F}_i^{(\text{align})} = b \sum_{j \in Q_a^{(i)}} \mathbf{v}_{j/i} \quad (3.7)$$

$$\mathbf{F}_i^{(\text{ext})} = -d\mathbf{v}_i + \mathbf{w}_i, \quad (3.8)$$

where \mathbf{w}_i represents random noise, and c , x_0 , b , and d are the spring, rest length, damping, and drag constants, respectively. Figure 3.10 illustrates the model parameters.

In order to generate oscillatory motion, the spacing force connects interacting particles as opposed to connecting each particle to a fixed point, as was considered previously in Section 2.3 (see (2.6)). The previous model was valid for swarms that form above a fixed marker on the ground (this behavior is known to occur for only one of the two anopheline genetic types [73]). The new model accommodates swarming above a fixed point by adding a fixed, virtual particle. Noting that $\|\mathbf{r}_{j/i}\| < x_0$ results in repulsion and $\|\mathbf{r}_{j/i}\| > x_0$ in attraction, $\mathbf{F}^{(\text{space})}$ is a dynamical analogue of existing models with attraction and repulsion zones [19]. As mentioned in [21], each agent does not have to know the positions of all other agents in the swarm.

For the set $Q_a^{(i)}$, an annular region around the agent was considered in [19]. Section 2.3 determined interactions by proximity in the unit-velocity space (i.e., disagreement in the direction of motion), based on the idea that insects may be able to recognize other insects' motion and perform velocity matching only if their relative velocity is sufficiently small. The use of the dot product in Section 2.3.2 was convenient, because of the compatibility with the unit-velocity cross correlation. However, even when the distance is small in the unit-velocity space, the relative velocity can still be large if the speeds are sufficiently different. Using distance in the velocity space avoids this problem, and it is also convenient for the Lyapunov analysis presented in Section 3.5.

The relative velocity $\mathbf{v}_{j/i}$ is generally not easy to measure (e.g., by sensing) for a moving agent if it has non-zero rotational velocity. However, mosquitoes do not rely heavily on yawing when they change their direction of motion [80]. In a planar problem, this condition makes the relative velocity in a body-fixed frame equivalent

to the relative velocity in the inertial frame, which justifies the use of $\mathbf{v}_{j/i}$ in the interaction model.

The alignment force $\mathbf{F}^{(\text{align})}$ was previously modeled in (2.7) as a damper that connects interacting particles. While intuitively straightforward, its function as a velocity damper was limited because the force was constrained along the direction parallel to the line connecting those two particles. The modified model (3.7) generates the alignment force using two dampers that act independently in orthogonal directions, so that the force in the position space is arbitrary. This modification improves the velocity-matching function and also simplifies the model compared to the first term in (2.7).

3.4.2 Female Model and Pursuit

To consider pursuit behavior, we include one or more particles that represent M female mosquitoes, denoted $i = N + 1, \dots, N + M$. As mentioned in Section 3.1, a female mosquito is attracted to the swarm and typically passes through it several times before coupling with a male. Therefore, we model the female as a particle attracted to its estimate of the centroid of the swarm. Let \mathbf{r}_G denote the swarm centroid as estimated by the female: i.e., $\mathbf{r}_G = \frac{1}{n_f} \sum_{j \in \mathcal{N}_f} \mathbf{r}_j$, where $\mathcal{N}_f = \{k \mid \|\mathbf{r}_{k/f}\| \leq \rho_f\}$ denotes the set of males in the perceptual range ρ_f of the female and n_f denotes the number of elements in \mathcal{N}_f . Also let \mathbf{r}_f denote the position of the female and $\mathbf{r}_{G/f} = \mathbf{r}_G - \mathbf{r}_f$. The spacing and external forces on the female are (there is no

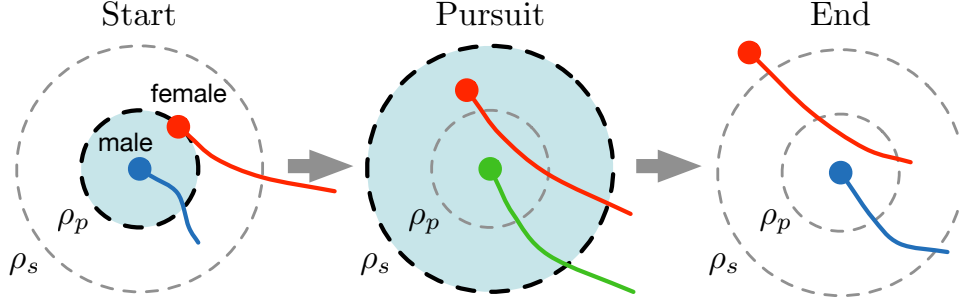


Figure 3.11: The pursuit state from start to end. Blue and red represent the male and female, respectively. The male in the pursuit state is highlighted in green.

alignment force)

$$\mathbf{F}_f^{(\text{space})} = c_f \mathbf{r}_{G/f} \quad \text{and} \quad \mathbf{F}_f^{(\text{ext})} = -d\mathbf{v}_f + \mathbf{w}_f, \quad (3.9)$$

where c_f denotes the spring constant.

Inspired by observations of coupling flight, we impose the following rules on the male's pursuit behavior. A male starts pursuit when the female is within the range ρ_p , and continues as long as the female is in the range ρ_s , where $\rho_p \leq \rho_s$. All other interactions are ignored during pursuit, i.e., $Q_s^{(i)}$ and $Q_a^{(i)}$ are replaced by $Q_p^{(i)} = \{f\}$, where f denotes the index of the pursued female. Figure 3.11 summarizes the use of parameters ρ_p and ρ_s .

3.4.3 Parameter Switching

To generate different behaviors, we switch the constants in the force model (3.6) and (3.7). Let \emptyset denote an empty set. Particle i is in the

1. swarming state, if $Q_s^{(i)} \neq \emptyset$ and $Q_a^{(i)} = Q_p^{(i)} = \emptyset$;

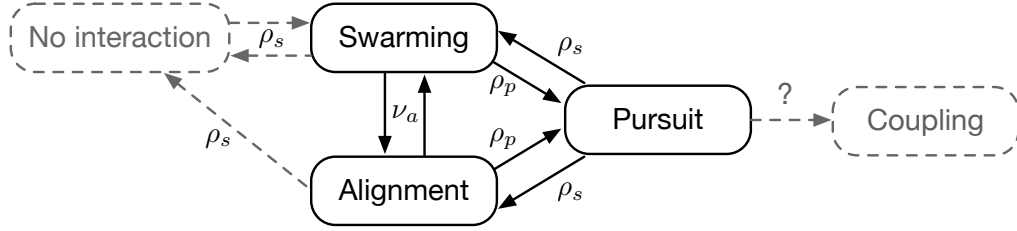


Figure 3.12: State transition diagram for male mosquito. The parameters associated with the transition are shown. The male-female coupling phase is not modeled.

Table 3.1: Parameter switching between three behavioral states.

	Swarming		Alignment		Pursuit
Spring constant (c)	c_s	=	c_s	≤	c_p
Rest length (x_0)	x_s	≥	x_a	≥	0
Damping constant (b)			b_a	≤	b_p

2. alignment state, if $Q_a^{(i)} \neq \emptyset$ and $Q_p^{(i)} = \emptyset$; and
3. pursuit state, if $Q_p^{(i)} \neq \emptyset$.

By definition, the states are mutually exclusive, and the transitions between the states are summarized with the relevant parameters in Fig. 3.12. The switching is summarized in Tab. 3.1, and Fig. 3.13 shows a simulation snapshot of each behavior generated by the model (3.5)–(3.8).

In the alignment behavior, the rest length of the spring is decreased relative to the swarming behavior (i.e., $x_a \leq x_s$). This switching is inspired by the decreased distance between interacting pairs shown in Fig. 2.5-a. When the pursuit behavior is triggered by a close encounter with the female, the spring and damping constants are increased relative to the swarming behavior (i.e., $c_p \geq c_s$ and $b_p \geq b_s$). This switching is based on the gain modulation shown in Fig. 3.9.

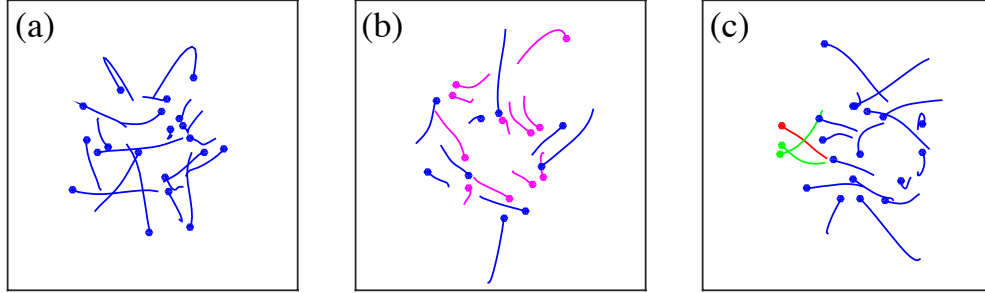


Figure 3.13: (a) Swarming behavior. The alignment behavior is turned off by choosing $\nu_a=0$. (b) Velocity-alignment behavior. Particles in the alignment state are highlighted in magenta. (c) Pursuit behavior. The red particle is the female and the green particles are in the pursuit state.

3.5 Lyapunov Stability Analysis

This section performs Lyapunov stability analysis of the swarm model. Our interest in this chapter is how the male's velocity-matching behavior affects its success in pursuing a female¹. Because the female's behavior is unknown, and because we are interested in the male's pursuit behavior, we define pursuit to be successful if a male stays close to the female for a certain duration of time:

Definition 3.1. *Consider the behavior of male i pursuing female f . Let t_{start} be the time of the close-encounter (i.e., when $\|\mathbf{r}_{f/i}\| = \rho_p$ occurs) and t_{end} be the time when f leaves the perceptual range of i (i.e., $\|\mathbf{r}_{f/i}\| > \rho_s$). Pursuit of duration $T_{dur} > 0$ is successful if*

$$\delta t \triangleq t_{end} - t_{start} > T_{dur}. \quad (3.10)$$

Note that we are interested in T_{dur} that is much larger than the time it takes for a female to accidentally pass through the perceptual region of a male, i.e.,

¹The cohesiveness of the swarm and the stability of velocity-matching interaction are also considered in [57] using Lyapunov analysis.

$T_{\text{dur}} \gg (\rho_p + \rho_s) / \|\mathbf{v}_f\|$. We show that the chance of this success may be increased by the male's alignment behavior.

Proposition 3.1. *Consider the pursuit behavior of male i and female f . Let $v_{\text{dur}} \triangleq (\rho_s - \rho_p) / T_{\text{dur}}$. Pursuit of duration T_{dur} is successful if*

$$(b_p + d)v_{\text{dur}} > c_f \rho_f + 2w, \quad \text{and} \quad (3.11)$$

$$\|\mathbf{v}_{f/i}(t_{\text{start}})\| < v_{\text{dur}}. \quad (3.12)$$

Proof. We first show that $\|\mathbf{v}_{f/i}(t)\| < v_{\text{dur}}$ for $t \in [t_{\text{start}}, t_{\text{end}}]$. Consider the Lyapunov function $V = \frac{1}{2} \|\mathbf{v}_{f/i}\|^2$. Let $\Delta_{f/i} \triangleq \mathbf{F}_f^{(\text{space})} - \mathbf{F}_i^{(\text{space})} + \mathbf{w}_f - \mathbf{w}_i$, denote the difference in the spacing and random forces acting on i and f . Since $\mathbf{F}_i^{(\text{space})} = \mathbf{0}$ in the pursuit phase, we have

$$\begin{aligned} \dot{V} &= \mathbf{a}_{f/i} \cdot \mathbf{v}_{f/i} \\ &= [c_f \mathbf{r}_{G/f} - d\mathbf{v}_f + \mathbf{w}_f - (b_p \mathbf{v}_{f/i} - d\mathbf{v}_i + \mathbf{w}_i)] \cdot \mathbf{v}_{f/i} \\ &= [-(b_p + d)\mathbf{v}_{f/i} + \Delta_{f/i}] \cdot \mathbf{v}_{f/i} \\ &\leq -\left(b_p + d - \frac{a}{2}\right) \|\mathbf{v}_{f/i}\|^2 + \frac{1}{2a} \|\Delta_{f/i}\|^2 \end{aligned}$$

where a is any positive number. Using the concept of ultimate boundedness [81], $\mathbf{v}_{f/i}$ remains in the interior of a ball with radius v_{dur} centered at $\mathbf{0}$ if

$$\begin{aligned} -\left(b_p + d - \frac{a}{2}\right) v_{\text{dur}}^2 + \frac{1}{2a} \|\Delta_{f/i}\|^2 &< 0 \\ \Leftrightarrow \|\Delta_{f/i}\|^2 &< 2a \left(b_p + d - \frac{a}{2}\right) v_{\text{dur}}^2. \end{aligned}$$

The right-hand side is maximized when $a = b_p + d$, which gives

$$\|\Delta_{f/i}\|^2 < (b_p + d)^2 v_{\text{dur}}^2.$$

One can also show that $\|\Delta_{f/i}\| < c_f \rho_f + 2w$. Now we have shown that (3.11) and (3.12) guarantees $\|\mathbf{v}_{f/i}(t)\| < v_{\text{dur}}$, for $t \in (t_{\text{start}}, t_{\text{end}})$. Then, the shortest time for f to leave the range ρ_s of i is bounded below by

$$\min\{\delta t\} > (\rho_s - \rho_p)/v_{\text{dur}} > T_{\text{dur}},$$

which completes the proof. □

The direct contribution of the velocity alignment term $\mathbf{F}^{(\text{align})}$ is seen in (3.11); i.e., condition (3.11) is satisfied if the damping constant b_p is sufficiently large. However, the more important effect is that the condition (3.12) is more likely to be satisfied if $\|\mathbf{v}_{f/i}(t_{\text{start}})\|$ is made small by the velocity-alignment behavior prior to the start of the pursuit behavior.

The following result provides conditions that guarantee the success of pursuit of any duration. Consider the Lyapunov function candidate

$$V_P = \frac{1}{2} \|\mathbf{r}_{f/i}\|^2 + \frac{1}{2c_p} \|\mathbf{v}_{f/i}\|^2. \quad (3.13)$$

Proposition 3.2. *Pursuit is stable (i.e., $\|\mathbf{r}_{f/i}\| < \rho_s, \forall t > t_{\text{start}}$) if the following are true:*

$$c_f \rho_f + 2w < (b_p + d) \|\mathbf{v}_{f/i}\|, \quad \text{and} \quad (3.14)$$

$$\|\mathbf{v}_{f/i}(t_{start})\| < \sqrt{c_p (\rho_s^2 - \rho_p^2)}. \quad (3.15)$$

Proof. Let $\Delta_{f/i} = \mathbf{F}_f^{(\text{space})} + \mathbf{w}_f - \mathbf{w}_i$. Then we have

$$\begin{aligned} c_p \dot{V}_P &= c_p \mathbf{v}_{f/i} \cdot \mathbf{r}_{f/i} + \mathbf{a}_{f/i} \cdot \mathbf{v}_{f/i} \\ &= c_p \mathbf{v}_{f/i} \cdot \mathbf{r}_{f/i} + [-(b_p + d)\mathbf{v}_{f/i} - c_p \mathbf{r}_{f/i} + \Delta_{f/i}] \cdot \mathbf{v}_{f/i} \\ &= -(b_p + d) \|\mathbf{v}_{f/i}\|^2 + \Delta_{f/i} \cdot \mathbf{v}_{f/i} \\ &\leq -\|\mathbf{v}_{f/i}\| [(b_p + d) \|\mathbf{v}_{f/i}\| - (c_f \rho_f + 2w)]. \end{aligned}$$

We have shown that (3.14) guarantees $\dot{V}_P < 0$, which gives the bound $V_P(t) < V_P(t_{start})$ for all $t > t_{start}$. Also, from (3.13) the distance between f and i is bounded by $\|\mathbf{r}_{f/i}\| \leq \sqrt{2V_P(t)}$. Noting that $\|\mathbf{r}_{f/i}(t_{start})\| = \rho_p$, (3.15) implies that

$$\begin{aligned} V_P(0) &< \frac{1}{2} \rho_p^2 + \frac{1}{2c_p} c_p (\rho_s^2 - \rho_p^2), \\ 2V_P(t) &< 2V_P(0) < \rho_s^2. \end{aligned}$$

Hence the distance never exceeds the limit ρ_s . □

Condition (3.14) is strong since the right-hand side can be arbitrarily small. However, even if the condition is violated occasionally, the result of Proposition 3.2 remains true as long as $V_P(t)$ stays less than its initial value $V_P(t_{start})$. Moreover, if the female is following a straight path and the random disturbance is ignored (i.e., $c_f = w = 0$), then the left hand side of (3.14) becomes zero, and the condition is

always satisfied. In this case, the only condition required for a stable pursuit is the initial condition (3.15).

The condition (3.15) on the initial relative velocity $\|\mathbf{v}_{f/i}\|$ highlights how the velocity-alignment behavior is useful for the success of pursuit. If a male aligns its velocity to a female prior to the pursuit phase (without knowing that it is a female), condition (3.15) is more likely to be satisfied. A more interesting case is when a male i (who does not see a female) performs velocity alignment to another male j who is pursuing the female. Through the velocity-alignment behavior, male i indirectly matches its velocity to a female, which increases the probability that the pursuit will be successful if the female eventually enters the perceptual range of male i . A similar scenario is considered later in Chapter 5, where we study cooperative pursuit strategy to capture a fast target.

Chapter 4

Mosquito-Inspired Pursuit: Single Pursuer Case

Historically, pursuit has been studied extensively for the purpose of missile guidance and navigation [31,33–36,40]. Various approaches have been taken with differing assumption including constant-speed agents, linearized dynamics about collision course, a non-maneuvering target, initially negative range rate, and knowledge of the target’s acceleration. These assumptions, especially the first two, are valid for fixed-wing vehicles or missiles, but do not apply to small and agile agents like mosquitoes or rotorcraft micro aerial vehicles (MAVs). This chapter considers a pursuit problem with assumptions and design criteria derived from the observation of the pursuit behavior in mosquito mating swarms. The results of this section advocate replacing pursuit laws developed for missile guidance with a bio-inspired algorithm designed for small, agile robotic vehicles. Section 4.1 discusses the design criteria for mosquito-inspired pursuit, formulates the problem, and introduces the hovercraft testbed used in the experiments. Section 4.2 derives the pursuit law, es-

establishes its robustness, and compares it with existing pursuit strategies. Section 4.3 presents the experimental results using the autonomous hovercraft testbed.

4.1 Background

This section discusses the design criteria for mosquito-inspired pursuit and formulates the pursuit problem as a planar particle system. Next, the section introduces the concept of ultimate boundedness, which we use to prove the robustness of the proposed control law in the sequel. The hovercraft testbed used in the experiments are also introduced in this section.

4.1.1 Design Criteria

Chapters 2 and 3 studied swarming and pursuit behaviors of mosquitoes. The motion in mosquito pursuit has two main features that do not match with the assumptions made in missile guidance literatures. First, a male accelerates once the distance to a female is sufficiently small (close encounter), which indicates that the agents have variable speed. Second, there is no well-defined collision course between a male and a female (see Fig. 4.1), instead they change their direction of motion rapidly.

To accommodate the aforementioned characteristics of the mosquito behavior, we consider a particle pursuit problem with nonlinear dynamics, allowing acceleration to be in an arbitrary direction. One closely related pursuit study used a sliding-mode controller [54] and another used a partial-stability-based controller [82]. We

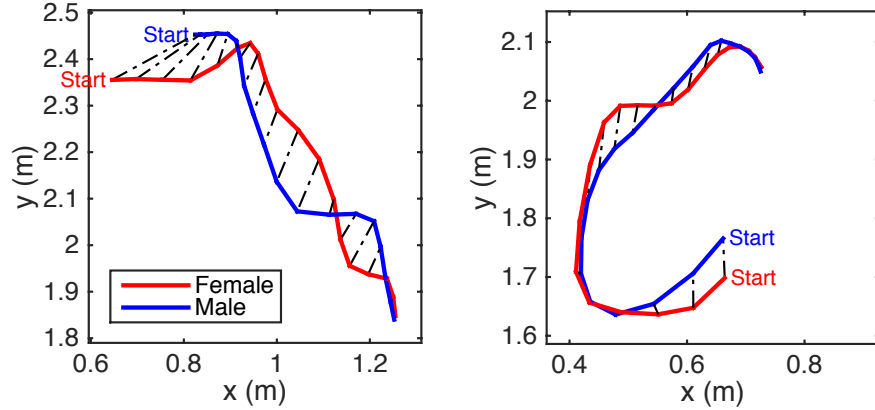


Figure 4.1: Trajectories of wild mosquitoes in coupling flight, reconstructed from stereoscopic video sequences [1]. Pursuit (possibly mutual) continues after several close encounters.

design a bio-inspired pursuit law using a Lyapunov-based approach fortified by the concept of ultimate boundedness. In addition to LOS stabilization, we consider the following design criteria.

The first criterion of bio-inspired pursuit is minimal control effort. In small vehicles—like in insects—the available control effort is restricted because of limited payload capacity, actuator size, and power/energy storage. Also, unlike missiles whose task ends at the target intercept, these pursuers may have to continue other tasks after intercept. Therefore, achieving target capture with low energy consumption is important.

Another criterion is robustness to uncertainties like sensor noise. The measurement errors of pertinent states like range, range rate, and LOS angular rate are often ignored in missile guidance. However, measurement error is an important consideration for a low-cost vehicle with rudimentary sensors.

The third design criterion arises in a near-miss scenario, i.e., how does the

pursuer behave if the pursuit continues after a near miss? The effect of wind, losing sight of the target, or an unexpectedly fast target maneuver may cause the pursuit to fail. The near-miss scenario is also seen in mosquito coupling flight (see Fig. 4.1) when the distance between two mating mosquitoes becomes very small and then grows; this cycle repeats several times before they form a couple. An important strategy may be to remain close to the target after a close encounter in order to decrease the control effort for the next attempt. The same scenario also applies if the objective of the pursuer is not to intercept the target but merely to stay close to it. In this case, the pursuer may be required to continue the pursuit for a longer duration of time. This work considers continued pursuit in the near-miss scenario, and we design the pursuit law so that it ensures robustness and efficiency.

4.1.2 Problem Formulation

Consider the following formulation of the pursuit problem as a planar system of two point particles with unit mass. Let T and P denote the target and the pursuer, respectively. Figure 4.2 depicts the relevant reference frames and coordinates, which includes the inertial frame $\mathcal{I} \triangleq (O, \hat{\mathbf{x}}, \hat{\mathbf{y}}, \hat{\mathbf{z}})$, the LOS frame $\mathcal{B} \triangleq (P, \hat{\mathbf{e}}_r, \hat{\mathbf{e}}_\theta, \hat{\mathbf{z}})$, the relative position vector $\mathbf{r} = \mathbf{r}_{T/O} - \mathbf{r}_{P/O}$, the range $r = \|\mathbf{r}\|$, and the LOS angle θ , where $\cos \theta = \hat{\mathbf{e}}_r \cdot \hat{\mathbf{x}}$.

The inertial kinematics of the two-particle system expressed as components in

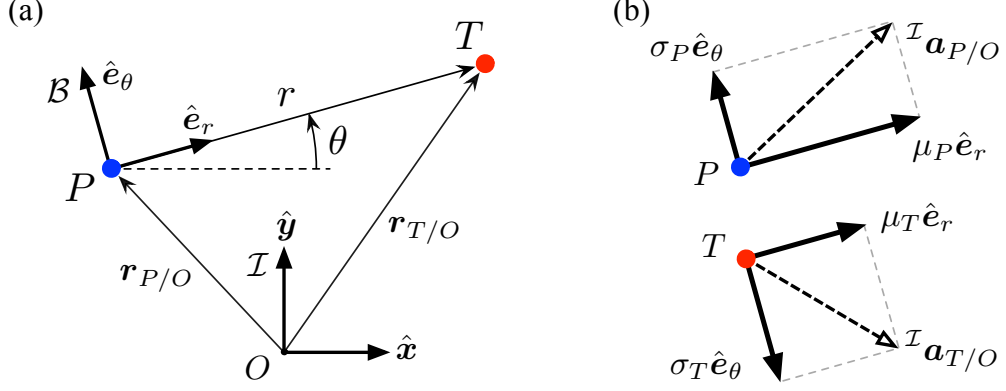


Figure 4.2: (a) The definition of line-of-sight (LOS) frame \mathcal{B} and the coordinate system (r, θ) where the pursuer P is pursuing the target T . (b) Decomposition of the acceleration into radial component μ and normal component σ in the LOS frame.

frame \mathcal{B} are [84]

$$\left[\frac{\mathcal{I} d^2}{dt^2} \mathbf{r} \right]_{\mathcal{B}} = \begin{bmatrix} \ddot{r} - r\dot{\theta}^2 \\ 2\dot{r}\dot{\theta} + r\ddot{\theta} \end{bmatrix}_{\mathcal{B}} = \begin{bmatrix} \mu_T - \mu_P \\ \sigma_T - \sigma_P \end{bmatrix}_{\mathcal{B}}, \quad (4.1)$$

where μ_T and σ_T (resp. μ_P and σ_P) denote the radial and normal components of the acceleration of T (resp. P) in frame \mathcal{B} .

The state of the system is $\mathbf{x} = [x_1, x_2, x_3]^T \triangleq [r, \dot{r}, r\dot{\theta}]^T$. The input to the system is the relative acceleration between T and P , i.e., $\mathbf{u} = [\mu, \sigma]^T \triangleq \mathbf{u}_T - \mathbf{u}_P$, where $\mathbf{u}_T \triangleq [\mu_T, \sigma_T]^T$ and $\mathbf{u}_P \triangleq [\mu_P, \sigma_P]^T$. Noting that $x_1 > 0$, we have the following state-space system on the domain $\mathcal{D} = \mathbb{R}^+ \times \mathbb{R}^2$:

$$\dot{\mathbf{x}} = \mathbf{f}(\mathbf{x}) + \mathbf{g}(\mathbf{x})\mathbf{u}, \quad \text{where} \quad \mathbf{f}(\mathbf{x}) = \begin{bmatrix} x_2 \\ x_3^2/x_1 \\ -x_2x_3/x_1 \end{bmatrix}, \quad \text{and} \quad \mathbf{g}(\mathbf{x}) = \begin{bmatrix} 0 & 0 \\ 1 & 0 \\ 0 & 1 \end{bmatrix}. \quad (4.2)$$

Let δ be a small positive constant. The statement

$$\dot{r}(t) = x_2(t) < -\delta < 0, \quad \forall t > t_f, \quad (4.3)$$

is a sufficient condition for target intercept in finite time [54]. Having a fixed LOS-angle θ or, equivalently, satisfying the condition $x_3 = 0$, is an efficient means of target intercept [31, 33–36, 40].

We seek to design a control law \mathbf{u}_P that ensures solutions of the system (4.2) converge to the domain $\mathcal{D}_2 = \{\mathbf{x} \mid x_2 < 0, x_3 = 0\}$. In doing so, we assume the following:

- (A1) either particle may accelerate in an arbitrary direction;
- (A2) the pursuer measures the state \mathbf{x} with random errors;
- (A3) the target acceleration \mathbf{u}_T is unknown, but the bound $\bar{u}_T \triangleq \max\{\|\mathbf{u}_T\|\}$ is known; and
- (A4) the particles have finite size and collide only when x_1 is less than $r_0 > 0$; $x_1 = 0$ does not occur.

Assumption (A1) may not apply to typical fixed-wing aircraft or missiles since they use control surfaces to accelerate in the direction approximately normal to the body forward axis. However, (A1) is applicable to rotorcraft such as a small-scale helicopter or quadcopter, which can change its attitude quickly and accelerate in any direction.

4.1.3 Ultimate Boundedness

We introduce the following lemmas related to ultimate boundedness [81] in order to subsequently prove robustness of the pursuit law in Section 4.2.2.

Lemma 4.1. *Consider a system $\dot{\mathbf{x}} = \mathbf{F}(t, \mathbf{x})$, where $\mathbf{x} \in \mathbb{R}^n$, $\mathbf{F}(\mathbf{x})$ is piecewise continuous and locally Lipschitz in \mathbf{x} . Let B_e denote a simply connected set that contains a point \mathbf{x}^* . Let the Lyapunov function candidate be $V(\mathbf{x}) = (\mathbf{x} - \mathbf{x}^*)^T P (\mathbf{x} - \mathbf{x}^*)$ where $P > 0$. Then the solution of the system enters the set $\Omega = \{ \mathbf{x} \mid V(\mathbf{x}) \leq c \}$ in finite time t_f and stays there for all $t > t_f$ if the following conditions are true:*

- $\dot{V}(\mathbf{x}) \leq -W(\mathbf{x})$ for all $\mathbf{x} \notin B_e$, where $W(\mathbf{x})$ is continuous and strictly positive in $\mathbf{x} \notin B_e$.
- Ω contains B_e .

Proof. Suppose the solution starts at $\mathbf{x}(t_0) = \mathbf{x}_0$, and $V(\mathbf{x}_0) < c_{max}$. Let $\Lambda = \{ \mathbf{x} \mid c \leq V(\mathbf{x}) \leq c_{max} \}$. Let $k = \min_{\mathbf{x} \in \Lambda} W(\mathbf{x}) > 0$. The minimum exists because $W(\mathbf{x})$ is continuous and Λ is compact. The solution enters Ω in finite time since

$$V(\mathbf{x}(t)) \leq V(\mathbf{x}_0) - k(t - t_0), \quad \forall \mathbf{x} \in \Lambda,$$

implies that $V(\mathbf{x}(t))$ reduces to c within the time interval $[t_0, t_0 + (c_{max} - c)/k]$.

The solution in Ω stays there for all future time since $\dot{V}(\mathbf{x}) < 0$ on the boundary of Ω (i.e., Ω is positively invariant). □



Figure 4.3: Autonomous pursuer hovercraft with onboard camera (left), and target hovercraft with IR light tower (right).

Lemma 4.2. *Using the same conditions as Lemma 4.1, if $W(\mathbf{x})$ (in the first bullet of Lemma 1) is of the form $W(\mathbf{x}) = (\mathbf{x} - \mathbf{x}^*)^T Q (\mathbf{x} - \mathbf{x}^*) - D$, where $Q = \text{diag}\{\rho_1, \rho_2, \dots, \rho_n\}$, $\rho_i > 0$, $D > 0$, then B_e is an ellipsoidal region centered at \mathbf{x}^* with axis length $\lambda_i = \sqrt{D/\rho_i}$ in each direction.*

4.1.4 Hovercraft Testbed

Existing guidance laws derived with strong assumptions have proven to be useful for real missile implementation [31], but there has not been an experimental validation of a pursuit law with small, agile vehicles. Experiments with heterogeneous teams of ground and aerial vehicles have been conducted for pursuit-evasion games [83], however our focus is on terminal guidance. We constructed an experimental testbed using custom-built, autonomous hovercraft with onboard sensing and control (see Fig. 4.3). Hovercraft are suitable to replicate flight conditions in two dimensions because, unlike most wheeled vehicles, they are holonomic and capable of rapid acceleration. These features make the hovercraft testbed a suitable preliminary

step towards implementation of three-dimensional pursuit in flight.

Both hovercraft in Fig. 4.3 participate in each experiment—one as pursuer and the other as target. We considered several objectives in the design of this platform: good representation of point-mass dynamics, i.e., full actuation and low drag; onboard target tracking and control; sturdiness to endure possible collisions during pursuit; and a small size to operate in the available lab space.

Conventional hovercraft are frequently propelled by two rear-facing fans or one fan and one or more rudders to provide forward thrust and yaw torque with a small number of fans [85, 86]. However, the conventional configuration is underactuated and rotationally asymmetric, making it ill-suited to our application. Other platforms add side-to-side thrusters to be fully actuated or use large numbers of thrusters, but these hovercraft are still rotationally asymmetric [87, 88]. Stubbs et al. [89] developed a networked hovercraft platform that is fully actuated and rotationally symmetric; however, it uses offboard cameras for position measurements and a layout of four unidirectional thrusters for propulsion.

Each hovercraft in our testbed measures 6.5 inches in diameter and weighs between 110 and 125 grams, depending on its configuration. Two lift fans carry the hovercraft and four unidirectional thrust fans arranged as in [89] accelerate and rotate it. Each hovercraft carries an ATmega32u4 processor capable of running fully autonomous target tracking and pursuit. The pursuer tracks the target using an onboard infrared (IR) camera from a Wii-mote game controller and an MPU6050 digital 6DOF Inertia Measurement Unit (IMU). The target hovercraft carries an infrared beacon consisting of two IR LED rings placed vertically three inches apart.

This arrangement allows the pursuer to autonomously track the target without the use of any offboard measurements. The camera field of view is also limited to approximately 60 degrees in azimuth. Proportional Integral Derivative (PID) control of the pursuer rotation centers the target in the camera field of view.

Target range x_1 is measured from the spacing of the IR points in the image. The range-rate x_2 is calculated by differentiating the measured range with respect to time. The angle to the target from the camera axis is differentiated with respect to time to find the LOS rotation rate in the body frame. This rate is added to the body-frame rotation rate in the inertial frame as measured by the IMU to determine the LOS angular-rate $\dot{\theta}$ in the inertial frame. Discrete low-pass filters are applied to all measured values in order to smooth out the discretized digital-image measurements and to reject erroneous single-measurement deviations.

Both hovercraft are equipped with an XBee wireless transceiver with which the pursuer transmits telemetry and the evader receives wireless commands from a ground station. The ground station uses an OptiTrack motion-capture system to track the trajectories of the pursuer and evader and to control the trajectory of the evader. In addition, the ground station logs telemetry from the pursuer and matches it to motion-capture data to record the performance (e.g., sensor measurements, controller output) of the pursuer. The pursuer's onboard sensing and control system are entirely autonomous and do not require human intervention or the motion-capture system.

4.2 Theoretical Results

This section presents a pursuit law designed with a Lyapunov-based approach and derives the conditions on the control gains to guarantee robust target intercept. We modify the pursuit law to accommodate noisy measurements. We also analytically and numerically compare the modified pursuit law to existing ones. Finally, we consider the effect of control saturation. The performance of the pursuit law is demonstrated by experiments described in Section 4.3.

4.2.1 Bio-inspired Pursuit Law

One way to satisfy the target-intercept condition (4.3) is to decrease x_2 as much as possible, as in [82]. Although this strategy may result in a short capture time, it requires a large control effort (see 4.2.4). In addition, a high closing speed may be problematic in a near-miss scenario. Another approach is to drive x_2 to a negative constant $v_{cl} < 0$ representing the desired closing speed [54]. This strategy will keep x_2 at a reasonable value and eliminate the issues raised above.

Consider the positive semi-definite Lyapunov function candidate

$$V = V_3(x_3) + V_2(x_2) \tag{4.4}$$

$$= \frac{\kappa}{2}x_3^2 + \frac{1}{2}(x_2 - v_{cl})^2, \quad \kappa > 0. \tag{4.5}$$

We first find the desired relative acceleration \mathbf{u}_{des} and then consider the actual control law \mathbf{u}_P of the pursuer.

One possible desired relative acceleration \mathbf{u}_{des} for the control Lyapunov function (4.5) was found previously using knowledge of target acceleration and Sontag's formula [90], which is proved to have optimality in minimizing the integral of control effort and states. In contrast, we make the pursuit law robust to uncertainties like unknown target acceleration by choosing

$$\mathbf{u}_{\text{des}} = \begin{bmatrix} -\frac{x_3^2}{x_1} - N_r(x_2 - v_{cl}) \\ \left(\frac{x_2}{x_1} - N_\theta\right)x_3 \end{bmatrix}, \quad N_r > 0, N_\theta > 0. \quad (4.6)$$

The robustness arises from the linear terms with sufficiently large control gains N_r and N_θ (see Proposition 4.1). The feedback control (4.6) makes the derivative of the Lyapunov function V in (4.5) negative semi-definite along solutions of (4.2), i.e.,

$$\dot{V} = -\kappa N_\theta x_3^2 - N_r(x_2 - v_{cl})^2 \leq 0. \quad (4.7)$$

The quadratic terms in (4.7) are convenient for analyzing the robustness of the pursuit law in the sequel. Note that \mathbf{u}_{des} is the desired relative acceleration, whereas $\mathbf{u} = \mathbf{u}_T - \mathbf{u}_P$ is the actual relative acceleration.

If the pursuit law is chosen to be $\mathbf{u}_P = \mathbf{u}_T - \mathbf{u}_{\text{des}}$, then the relation $\mathbf{u} = \mathbf{u}_{\text{des}}$ holds, and the closed-loop system will stabilize the equilibrium point $\mathbf{x}^* = [x_2^*, x_3^*]^T = [v_{cl}, 0]^T$, which ensures target capture in finite time. However, this pursuit law requires knowledge of the target acceleration \mathbf{u}_T . Therefore, we treat \mathbf{u}_T as an

external disturbance, $\Delta \triangleq [\Delta_r, \Delta_\theta]^T$, and consider the pursuit law

$$\mathbf{u}_P = -\mathbf{u}_{\text{des}}. \quad (4.8)$$

The relative acceleration achieved by (4.8) is

$$\mathbf{u} = \mathbf{u}_T - \mathbf{u}_P = \mathbf{u}_{\text{des}} + \Delta, \quad (4.9)$$

where $\Delta \equiv \mathbf{u}_T$. We consider the robustness of the controller to the disturbance Δ in the next section.

Remark 4.1. *One could use a disturbance observer [91, 92] to estimate the target acceleration and to incorporate the estimated value $\hat{\mathbf{u}}_T$ into the pursuit law, so that $\mathbf{u}_P = \hat{\mathbf{u}}_T - \mathbf{u}_{\text{des}}$. However, there would still be a disturbance due to the estimation error $\mathbf{u}_T - \hat{\mathbf{u}}_T$ for a time-varying \mathbf{u}_T [91] and the achieved relative acceleration would still be expressed as in (4.9), with $\Delta \equiv \mathbf{u}_T - \hat{\mathbf{u}}_T$; the robustness analysis in the next section still applies in this case.*

Remark 4.2. *The terms $-x_3^2/x_1$ and x_2x_3/x_1 in (4.6) may become large when the range x_1 becomes small, although they do not grow unbounded (see assumption (A8)). The proposed control law avoids this issue by regulating $|x_3|$ to be small. Also, for the case where large acceleration is commanded, robustness to control saturation is considered in Section 4.2.5.*

4.2.2 Robustness to Measurement Error

Robustness of the pursuit law to unknown target acceleration was studied in [54] using sliding-mode control and in [82] using partial-stability-based control. In those studies, signum functions were employed to address the possibility of unknown target acceleration, which was treated as a matching disturbance. However, the effect of measurement error was not considered in [54] or [82]. We show here that the proposed pursuit law (4.8), where \mathbf{u}_{des} is given by (4.6), is robust to both unknown target acceleration and measurement error under a proper choice of the control gains N_r and N_θ .

As observed in our experimental testbed, the measured states x_1 , x_2 and x_3 typically include some amount of noise. Let the measured states (or estimated states, see *Remark 1* above) available to the pursuer be defined as $\mathbf{x}_{\text{meas}} \triangleq \mathbf{x} + \mathbf{e}$, where $\mathbf{e} = [e_1, e_2, e_3]^T$ denotes the measurement (or estimation) error. We make the following additional assumptions regarding the error based on the experimental testbed:

(A5) the error on the range measurement e_1 may be ignored, since it is sufficiently small compared to e_2 and e_3 ;

(A6) $|e_i| \ll |x_i|$ for $i=1, 2, 3$, so the error terms that are higher than first order may be ignored; and

(A7) the magnitudes $|e_2|$ and $|e_3|$ are bounded by constants e_2^* and e_3^* respectively, where $e_2^* < |v_{cl}|$ and $e_3^* < |v_{cl}|/\sqrt{\kappa}$.

The validity of these assumptions for the experimental testbed is discussed in Section 4.3. Since the upper bound on the vehicle speed (which limits x_3) and the lower bound on the range (x_1) both exist in the physical implementation, we also assume

(A8) the absolute value of the LOS rate $|\dot{\theta}| = |x_3/x_1|$ is bounded by a constant,

$$\omega > 0.$$

The desired acceleration term, \mathbf{u}_{des} in (4.8) is implemented with the measured states \mathbf{x}_{meas} , and the input \mathbf{u} in (4.9) becomes

$$\mathbf{u} = \mathbf{u}_{\text{des}}(\mathbf{x}_{\text{meas}}) + \Delta \quad (4.10)$$

$$= \begin{bmatrix} -\frac{(x_3 + e_3)^2}{x_1 + e_1} - N_r(x_2 + e_2 - v_{cl}) + \Delta_r \\ \left(\frac{x_2 + e_2}{x_1 + e_1} - N_\theta\right)(x_3 + e_3) + \Delta_\theta \end{bmatrix}. \quad (4.11)$$

Let $\tilde{x}_2 \triangleq x_2 - v_{cl}$. The derivative of the Lyapunov function candidate in (4.7) becomes

$$\dot{V} = \dot{V}_2 + \dot{V}_3, \text{ where} \quad (4.12)$$

$$\dot{V}_2 = -N_r \tilde{x}_2^2 - N_r \tilde{x}_2 e_2 - 2\frac{x_3}{x_1} \tilde{x}_2 e_3 + \tilde{x}_2 \Delta_r, \text{ and} \quad (4.13)$$

$$\dot{V}_3 = \kappa \left(-N_\theta x_3^2 - N_\theta x_3 e_3 + \frac{x_3}{x_1} (x_3 e_2 + x_2 e_3) + x_3 \Delta_\theta \right). \quad (4.14)$$

Proposition 4.1. *The pursuit law (4.8) is robust to disturbance Δ and measurement error \mathbf{e} if the control gains are chosen to satisfy*

$$N_r > \frac{\bar{u}_T + 2\omega e_3^*}{|v_{cl}| - e_2^*} \quad \text{and} \quad (4.15)$$

$$N_\theta > \frac{\sqrt{\kappa}(2\bar{u}_T + 2\omega e_2^* + \omega e_3^* + 4\kappa\omega e_3^*)}{2|v_{cl}| - 2\sqrt{\kappa}e_3^*}. \quad (4.16)$$

Moreover, if \mathbf{e} is ignored, the conditions (4.15) and (4.16) simplify to

$$N_r > \frac{\bar{u}_T}{|v_{cl}|} \quad \text{and} \quad N_\theta > \frac{\sqrt{\kappa}\bar{u}_T}{|v_{cl}|}. \quad (4.17)$$

Proof. Since the worst case of \dot{V}_2 can be decoupled from the x_3 dynamics by Assumption (A8), we first show that x_2 is bounded in steady state using the Lyapunov function $V_2(x_2)$. The cross terms, for example $\tilde{x}_2 e_2$, may be bounded by $|\tilde{x}_2 e_2| \leq \frac{1}{2}(c_1 \tilde{x}_2^2 + e_2^2/c_1)$ using a constant $c_1 > 0$. Bounding the other cross terms using positive constants c_i , $i = 2, 3$, and using (A5), (A6) and (A8) yields

$$\dot{V}_2 \leq -N_r \tilde{x}_2^2 + \frac{N_r}{2} \left(c_1 \tilde{x}_2^2 + \frac{e_2^{*2}}{c_1} \right) + \omega \left(c_2 \tilde{x}_2^2 + \frac{e_3^{*2}}{c_2} \right) + \frac{1}{2} \left(c_3 \tilde{x}_2^2 + \frac{\bar{u}_T^2}{c_3} \right).$$

Choosing the constants to be

$$c_1 = \frac{e_2^*}{|v_{cl}|}, \quad c_2 = \frac{e_3^*}{|v_{cl}|}, \quad \text{and} \quad c_3 = \frac{\bar{u}_T}{|v_{cl}|}, \quad (4.18)$$

we have

$$\begin{aligned} \dot{V}_2 &\leq -\rho_2 (x_2 - v_{cl})^2 + D_2, \quad \text{where} \\ \rho_2 &= \left(1 - \frac{e_2^*}{2|v_{cl}|} \right) N_r - \frac{\bar{u}_T + 2\omega e_3^*}{2|v_{cl}|} \quad \text{and} \\ D_2 &= \frac{|v_{cl}|}{2} (\bar{u}_T + N_r e_2^* + 2\omega e_3^*). \end{aligned}$$

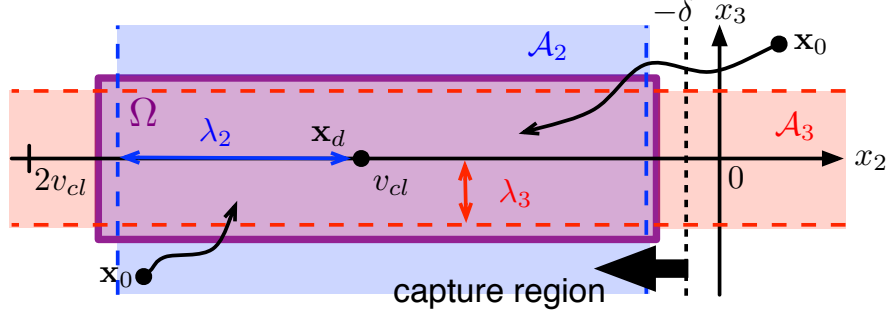


Figure 4.4: Ultimate boundedness of the solutions in the x_2x_3 -plane. The solutions starting at any initial condition \mathbf{x}_0 are guaranteed to converge to regions \mathcal{A}_2 and \mathcal{A}_3 . Convergence to the set Ω lying on the left side of $x_2 = -\delta$ ensures target capture in finite time.

Lemmas 4.1 and 4.2 apply if $\rho_2 > 0$, which is true when N_r satisfies the condition (4.15). From Lemmas 4.1 and 4.2, the solutions of the system converge to a region $\mathcal{A}_2 = \{\mathbf{x} \mid x_2 \in \Omega_2\}$, where Ω_2 is a line segment that contains the set $B_2 \triangleq \{x_2 : |x_2 - v_{cl}| \leq \lambda_2\}$ with $\lambda_2 = \sqrt{D_2/\rho_2}$, which is a one-dimensional analogue of the ellipsoidal region in Lemma 4.2.

One may choose λ_2 to be small so that x_2 converges to a small region around v_{cl} . However, in order to require less control effort, we seek to relax as much as possible the requirements on the control gain N_r . Making use of the condition (4.3), it is sufficient for solutions to fall inside the set Ω_2 lying in the left-half plane in Fig. 4.4 (strictly speaking, to the left of the line $x_2 = -\delta$). A suitable $\delta > 0$ and Ω_2 exist if $\lambda_2 < |v_{cl}|$, which is equivalent to $D_2 < |v_{cl}|^2 \rho_2$. Using the expressions for D_2 and ρ_2 above, the latter condition reduces to (4.15).

Suppose condition (4.15) is satisfied, then there exist $t_f \geq 0$ such that $x_2 \in \Omega_2, \forall t > t_f$. After entering Ω_2 , x_2 is bounded as $0 < x_2^2 < 4v_{cl}^2$. Although \dot{V}_3 includes the x_2^2 term, we use this inequality and positive constants $c_i, i = 4, 5, 6, 7$,

to bound \dot{V}_3 as

$$\begin{aligned} \frac{\dot{V}_3}{\kappa} &\leq -N_\theta x_3^2 + \frac{N_\theta}{2} \left(c_4 x_3^2 + \frac{e_3^{*2}}{c_4} \right) + \frac{1}{2} \left(c_7 x_3^2 + \frac{\bar{u}_T^2}{c_7} \right) \\ &\quad + \frac{\omega}{2} \left(4c_5 v_{cl}^2 + \frac{e_3^{*2}}{c_5} + c_6 x_3^2 + \frac{e_2^{*2}}{c_6} \right). \end{aligned}$$

Note that the above inequality is valid for $t > t_f$. Choosing the constants to be

$$c_4 = c_5 = \frac{\sqrt{\kappa} e_3^*}{|v_{cl}|}, \quad c_6 = \frac{\sqrt{\kappa} e_2^*}{|v_{cl}|}, \quad \text{and} \quad c_7 = \frac{\sqrt{\kappa} \bar{u}_T}{|v_{cl}|}, \quad (4.19)$$

we have

$$\dot{V}_3 \leq -\kappa \rho_3 x_3^2 + \kappa D_3, \quad \text{where} \quad (4.20)$$

$$\rho_3 = \left(1 - \frac{\sqrt{\kappa} e_3^*}{2|v_{cl}|} \right) N_\theta - \frac{\sqrt{\kappa} (\bar{u}_T + \omega e_2^*)}{2|v_{cl}|} \quad \text{and} \quad (4.21)$$

$$D_3 = \frac{|v_{cl}|}{2\sqrt{\kappa}} (\bar{u}_T + N_\theta e_3^* + \omega e_2^* + \omega e_3^* + 4\kappa \omega e_3^*). \quad (4.22)$$

The condition $\rho_3 > 0$ is true if N_θ satisfies the condition (4.16). By the same argument as above, we seek the condition for the convergence of the solutions to $\mathcal{A}_3 = \{\mathbf{x} \mid x_3 \in \Omega_3\}$, where the set Ω_3 contains $B_3 \triangleq \{x_3 : |x_3| \leq \lambda_3 = \sqrt{D_3/\rho_3}\}$.

Consider the condition $\lambda_3 < |v_{cl}|/\sqrt{\kappa}$, which is equivalent to $\kappa D_3 < |v_{cl}|^2 \rho_3$.

Using the expressions for D_3 and ρ_3 above, this condition reduces to (4.16). A large κ stabilizes x_3 to a small value while requiring greater control effort (see (4.16)).

Nonetheless, the solution is guaranteed to converge to the rectangular region $\Omega \triangleq$

$\{\mathbf{x} \mid x_2 \in \Omega_2, x_3 \in \Omega_3\}$ in Fig. 4.4, which completes the proof. \square

4.2.3 Modification of the Pursuit Law

Although convergence to a rectangular region provides a relaxed condition on the control gains, the required control may be large if the terms $|x_2 - v_{cl}|$ or $|x_3|$ are initially large. This problem is not restricted to the initial conditions; for example, if the measurement error is large, it may cause an erroneously large control input.

In order to avoid this issue and to keep the acceleration command small even in the presence of measurement error, we saturate the linear terms in (4.6) using the saturation function

$$\text{sat}(x) = \begin{cases} x & \text{if } |x| \leq 1, \\ 1 & \text{otherwise.} \end{cases} \quad (4.23)$$

The saturated control is

$$\mathbf{u}_{\text{des}} = \begin{bmatrix} -\frac{x_3^2}{x_1} - N'_r \text{sat}\left(\frac{x_2}{|v_{cl}|} + 1\right) \\ \frac{x_2 x_3}{x_1} - N'_\theta \text{sat}\left(\frac{\sqrt{\kappa}}{|v_{cl}|} x_3\right) \end{bmatrix}, \quad (4.24)$$

where $N'_r = N_r |v_{cl}|$ and $N'_\theta = N_\theta |v_{cl}| / \sqrt{\kappa}$. Note that the saturated terms are identical to the original terms when $|\tilde{x}_2| \leq |v_{cl}|$ and $|x_3| \leq |v_{cl}| / \sqrt{\kappa}$. The nonlinear terms are excluded from the saturation function in order to ensure cancellation of $\mathbf{f}(\mathbf{x})$ in (4.2). Note that the ultimate-boundedness property still holds after this modification, which is proved as follows.

It is sufficient to show that \dot{V}_2 and \dot{V}_3 are still negative in the region where

the linear terms are actually saturated. For the radial component V_2 , the saturated control (4.24) yields

$$\begin{aligned}
\dot{V}_2 &= \tilde{x}_2 \dot{x}_2 \\
&= \tilde{x}_2 \left(\frac{x_3^2}{x_1} - \frac{(x_3 + e_3)^2}{x_1 + e_1} - N'_r \text{sgn}(\tilde{x}_2) + \Delta_r \right) \\
&< \tilde{x}_2 \text{sgn}(\tilde{x}_2) (2\omega e_3^* - N'_r + \bar{u}_T) \\
&= -|\tilde{x}_2| (N'_r - 2\omega e_3^* - \bar{u}_T).
\end{aligned}$$

Noting that $N'_r \triangleq N_r |v_d| > 2\omega e_3^* + \bar{u}_T$ (if we choose N_r according to (4.15)), the term inside the parenthesis is positive, and we have $\dot{V}_2 < 0$. The stability of the normal component V_3 can be proved in a similar way.

4.2.4 Comparison with Existing Pursuit Laws

In order to distinguish (4.8) from other pursuit laws, let \mathbf{u}_A denote pursuit law (4.8), where \mathbf{u}_{des} is given by (4.24). We compare \mathbf{u}_A to the partial-stability-based controller [82], \mathbf{u}_B , and to the sliding-mode controller [54], \mathbf{u}_C , which are also robust to unknown target acceleration; \mathbf{u}_B and \mathbf{u}_C are

$$\mathbf{u}_B = \begin{bmatrix} \mu_B \\ \sigma_B \end{bmatrix} = \begin{bmatrix} \frac{x_3^2}{x_1} - \nu x_2 + \eta_1 \\ \left(-\frac{x_2}{x_1} + N \right) x_3 + \eta_2 \text{sat} \left(\frac{x_3}{\varepsilon} \right) \end{bmatrix} \quad (4.25)$$

and

$$\mathbf{u}_C = \begin{bmatrix} \mu_C \\ \sigma_C \end{bmatrix} = \begin{bmatrix} \frac{x_3^2}{x_1} + \eta_1 \text{sat} \left(\frac{x_2 - v_{cl}}{\varepsilon} \right) \\ -(N+1) \frac{x_2 x_3}{x_1} + \eta_2 \text{sat} \left(\frac{x_3}{\varepsilon} \right) \end{bmatrix}, \quad (4.26)$$

where $\nu, N, \varepsilon > 0$, $\eta_1 > \bar{u}_T$, and $\eta_2 > \bar{u}_T$. Also consider a naive controller, \mathbf{u}_D , whose radial acceleration is constant, i.e., $\mu_D = \mu^*$, and whose normal acceleration is $\sigma_D = \sigma_A$.

Remark 4.3. *The pursuit law μ_B requires $x_2(0) < 0$ for an initial condition [82], whereas law μ_A and the sliding-mode control μ_C are robust to $x_2(0) > 0$.*

Metrics often used in comparing pursuit strategies include the capture time, the required σ_P , and the required μ_P . There is no significant difference in the performance and control effort in the normal component between the considered pursuit laws, as can be seen in [82] and also in the numerical simulations shown below. Once $\dot{\theta} \approx 0$, short capture times are achieved by using a large μ_P , which can be seen from the dynamics (4.2), i.e., $\dot{x}_2 = \mu_T - \mu_P$ when $x_3 = 0$. Therefore, to achieve a pursuit law with a short capture time one needs simply to command the maximum available radial acceleration. Based on these observations, we focus on the radial component and compare the control effort and energy consumption required for robust target capture.

Since all of the pursuit laws except \mathbf{u}_D have the term x_3^2/x_1 , which cancels the

centrifugal acceleration in \mathcal{B} , let

$$G \triangleq \mu - \frac{x_3^2}{x_1} \quad (4.27)$$

denote the additional term on the radial component, and compare G from the three pursuit laws. For a fair comparison, we choose the smallest control gains for N_r and η_1 that guarantee robustness (strictly speaking, the limiting value, i.e., if $N > a$ is required, then we choose $N = a$). Small constants ν and ε are retained as parameters. Only the no-measurement-error case is considered since measurement error was not studied in [54, 82].

From condition (4.17) and (4.24), $N'_\theta = \bar{u}_T$. The additional term G of the control laws with minimal gains are

$$G_A = \bar{u}_T \text{sat} \left(\frac{x_2}{|v_{cl}|} + 1 \right) \quad (4.28)$$

$$G_B = -\nu x_2 + \bar{u}_T \quad (4.29)$$

$$G_C = \bar{u}_T \text{sat} \left(\frac{x_2 - v_{cl}}{\varepsilon} \right) \quad (4.30)$$

$$G_D = \mu^* - x_3^2/x_1. \quad (4.31)$$

Figure 4.5 shows G as a function of x_2 . Noting that \mathbf{u}_A ensures $\tilde{x}_2 < |v_{cl}|$, or equivalently $2v_{cl} < x_2 < 0$, after a certain amount of time, G_A has the smallest absolute value for the same states \mathbf{x} .

Remark 4.4. *The sliding mode controller μ_C becomes identical to μ_A if $\varepsilon = |v_{cl}|$. Although ε is typically a small value introduced in order to avoid the chattering from*

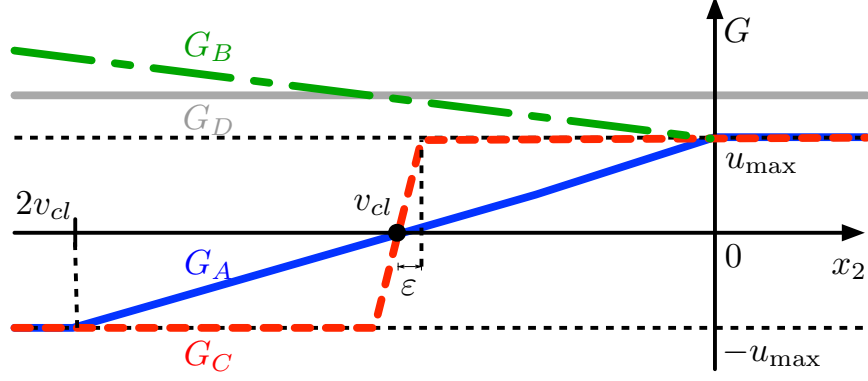


Figure 4.5: Comparison of the controller specific terms G (see (4.27)) in the radial control as a function of range rate x_2 . For simplicity, $x_3=0$ is assumed for the naive controller G_D . The pursuit law G_A has the smallest absolute value, which results in the smallest control effort.

the signum function [54], it may be as large as $|v_{cl}|$ and still guarantee robustness. In the particular case for which the smallest control gains are considered, the proposed controller μ_A can be categorized as a sliding-mode controller with sliding surface relaxed as much as possible while maintaining robustness. The comparative study shows the advantage of this design philosophy with respect to the design criteria that we consider.

Figure 4.6 shows the results of numerical simulations up to the time of the first close encounter. The open-loop trajectory of the target is specified by $\mathbf{u}_T(t) = [0.5 \sin(0.4\pi t + 0.3\pi), 0.5 \sin(\pi t + 0.4\pi)]$, and the initial conditions are $\mathbf{r}_{P/O}(0) = [0, 0]$, $\mathbf{v}_{P/O}(0) = [0, 0]$, $\mathbf{r}_{T/O}(0) = [2, 0]$, and $\mathbf{v}_{T/O}(0) = [-.5, .7]$. Parameters and control gains were $v_{cl} = -2.0$, $\kappa = 400$, $\nu = 0.1$, $N = 2$, $\varepsilon = 0.1$, and $\bar{u}_T = 0.5$, which gives $N'_r = N'_\theta = \eta_1 = \eta_2 = 0.5$. The naive control law \mathbf{u}_D is simulated with $\mu_1^* = 0.4$ and $\mu_2^* = 0.7$, denoted Naive 1 and Naive 2, respectively. Consider the energy consumption defined as $E_{tot} = \int_{t_0}^t \|\mathbf{u}(\tau)\|^2 d\tau$ [93]. Since the motor voltage is proportional

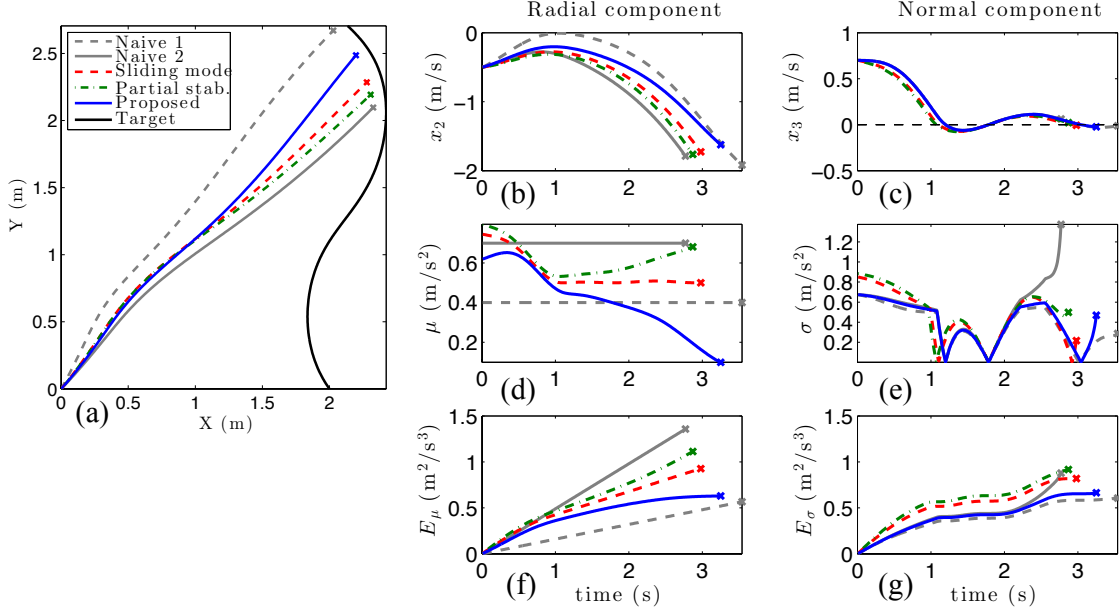


Figure 4.6: Numerical simulation until the first close encounter. (a) Trajectories from different pursuit laws against the same target (black). (b, c) States. (d, e) Absolute value of acceleration commands. (f, g) Energy expenditure calculated from the time integral of squared acceleration commands. The left column (b, d, f) and the right column (c, e, g) describe the radial and normal components in the LOS frame, respectively.

to the magnitude of the acceleration command, E_{tot} is proportional to the amount of energy consumption, assuming that the motor impedance is approximately constant. E_μ and E_σ are the radial and normal components of the energy consumption. Comparison of the normal component differs only at the end, when x_1 becomes small. In the radial component, the bio-inspired control law (blue) has the smallest maximum acceleration and energy consumption.

Figure 4.7 shows the case when the pursuit is continued after the first close encounter. This scenario corresponds to a near miss or target tracking. To quantify the performance, look at the energetic cost $J = \int_0^t \{x_1(\tau)\}^2 d\tau$ shown in Fig. 4.7-b. The bio-inspired pursuit law has the smallest J and the smallest energy consump-

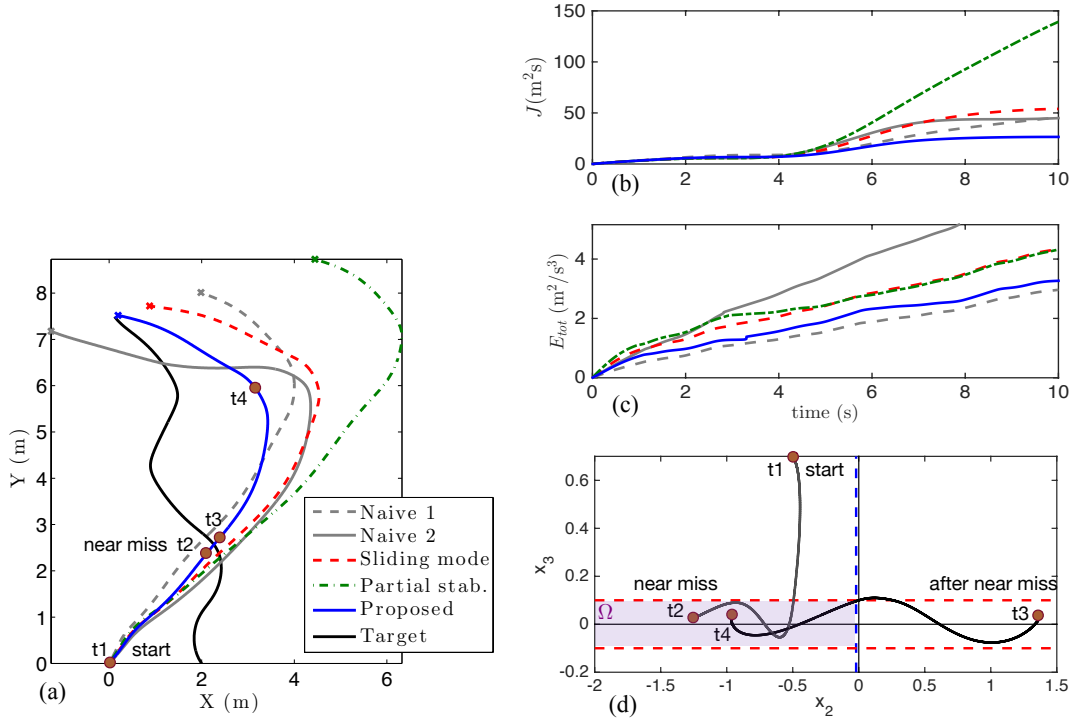


Figure 4.7: Numerical simulation of near-miss scenario. (a) Trajectories from different pursuit laws against the same target (black). (b) Energetic cost, which penalizes the deviation from the target. (c) The total energy expenditure E_{tot} . (d) Phase portrait in x_2x_3 -space for proposed controller. The time stamps t_1 to t_4 correspond to those in (a).

tion E_{tot} . Figure 4.7-d shows a phase portrait in x_2x_3 -space. At the instant of a near miss, the range rate x_2 changes sign from negative to positive, but the solution returns to the set Ω (see the proof of Proposition 4.1) in finite time.

4.2.5 Robustness to Control Saturation

In the pursuit problem considered thus far, as well as in [54, 82], the pursuer may achieve arbitrary acceleration: i.e., it can accelerate in any direction with any magnitude. Under such an assumption, the pursuit law (4.8) effectively cancels the vector field $\mathbf{f}(\mathbf{x})$ in (4.2) and adds a vector field $[-N_r\tilde{x}_2, -N_\theta x_3]^T$ that is sufficiently strong

to drive the solution of the system to \mathbf{x}^* , even in the presence of uncertainty Δ . However, the cancelation of $\mathbf{f}(\mathbf{x})$ is not always possible, e.g., in a physical implementation for which the acceleration is limited. This section considers the robustness of the pursuit law to control saturation.

To simplify the analysis, consider \mathbf{u}_{des} in (4.6) without the measurement errors, and the case where the target is under a naive evasive maneuver:

$$\mathbf{u}_T = \begin{bmatrix} \mu_T \\ \sigma_T \end{bmatrix} = \begin{bmatrix} \bar{u}_T \\ \bar{u}_T \text{sign}(x_3) \end{bmatrix}. \quad (4.32)$$

This evasive strategy increases the range rate by accelerating away from the pursuer and increasing the LOS rate. The target tries to avoid what the pursuer is trying to achieve—zero LOS rate and negative range rate.

Let \bar{u}_P denote the bound on pursuer's acceleration in each direction; i.e., $\eta_P, \sigma_P \leq \bar{u}_P$. With the pursuit strategy (4.8) and evasive strategy (4.32), the system (4.2) is described as

$$\dot{\mathbf{x}} = \begin{bmatrix} x_2 \\ x_3^2/x_1 - \bar{u}_P \text{sat}\left(\frac{h_1(\mathbf{x})}{\bar{u}_P}\right) + \bar{u}_T \\ -x_2 x_3/x_1 - \bar{u}_P \text{sat}\left(\frac{h_2(\mathbf{x})}{\bar{u}_P}\right) + \bar{u}_T \text{sign}(x_3) \end{bmatrix},$$

where $\begin{bmatrix} h_1(\mathbf{x}) \\ h_2(\mathbf{x}) \end{bmatrix} = \begin{bmatrix} x_3^2/x_1 + N_r(x_2 - v_{cl}) \\ -x_2 x_3/x_1 + N_\theta x_3 \end{bmatrix}.$

Let $\bar{u} \triangleq \bar{u}_P - \bar{u}_T > 0$. Also, let N_r^* and N_θ^* denote the limiting gain values

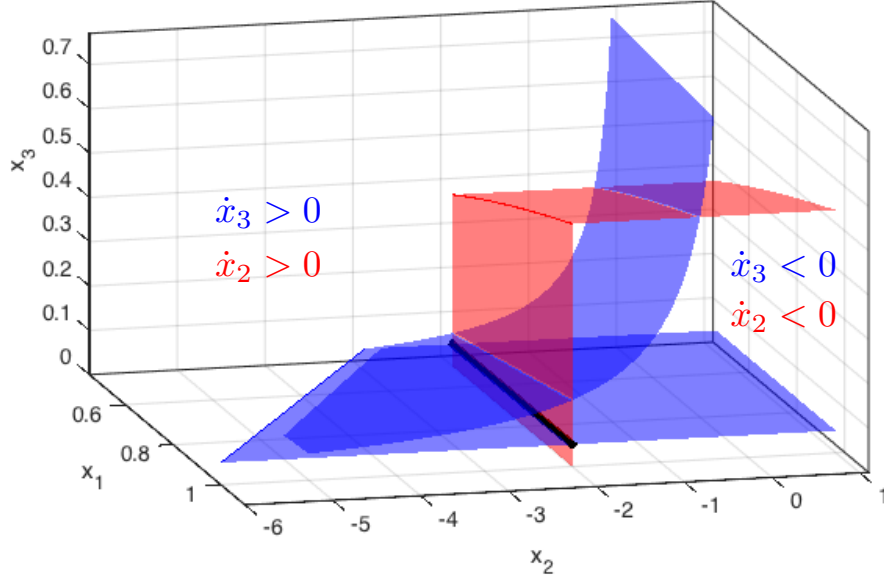


Figure 4.8: Nullclines of the system; i.e., surfaces where $\dot{x}_2 = 0$ (red) and $\dot{x}_3 = 0$ (blue). The surface for $\dot{x}_1 = 0$, which is a x_1x_3 -plane at $x_2 = 0$, is omitted for clarity.

that satisfy (4.17), i.e., $N_r^* \triangleq \bar{u}_T/|v_{cl}|$ and $N_\theta^* \triangleq \sqrt{\kappa}\bar{u}_T/|v_{cl}|$.

Proposition 4.2. *The pursuit law (4.8) is robust to control saturation and evasive maneuver (4.32) if $\bar{u} = \bar{u}_P - \bar{u}_T > 0$ and the control gains satisfy condition (4.17) and*

$$\frac{N_\theta^*}{N_\theta} \left(1 - \frac{N_r^*}{N_r} \right) \sqrt{\kappa} < 1 \quad (4.33)$$

with $\sqrt{\kappa} = |v_{cl}|/\sqrt{\bar{u}r_0}$.

Proof. Figure 4.8 shows the nullclines of the system with the proper choice of control gains. By symmetry, consider only the positive x_3 region ($x_3 = 0$ is a separatrix). From the sign of \dot{x}_2 and \dot{x}_3 in each area separated by the nullclines, observe that the black solid line is a stable manifold. Hence, the following two conditions guarantee target capture: (1) the stable manifold exists and lies in the negative x_2 region; and

(2) the stable manifold intersects the surface $x_1 = r_0$.

We express these conditions in a different way by looking at the two-dimensional slice of the nullclines for each x_1 value. Figure 4.9 shows four configurations of the nullclines arising from different choices of the control gains and x_1 . The locations of the solid lines are determined by the system parameters \bar{u} and r_0 , whereas the dashed lines are determined by the control gains v_{cl} , κ , N_r and N_θ (chosen by the pursuer). The intersecting points of the dashed and solid lines are denoted as P_2 and P_3 , respectively (right bottom in Fig. 4.9).

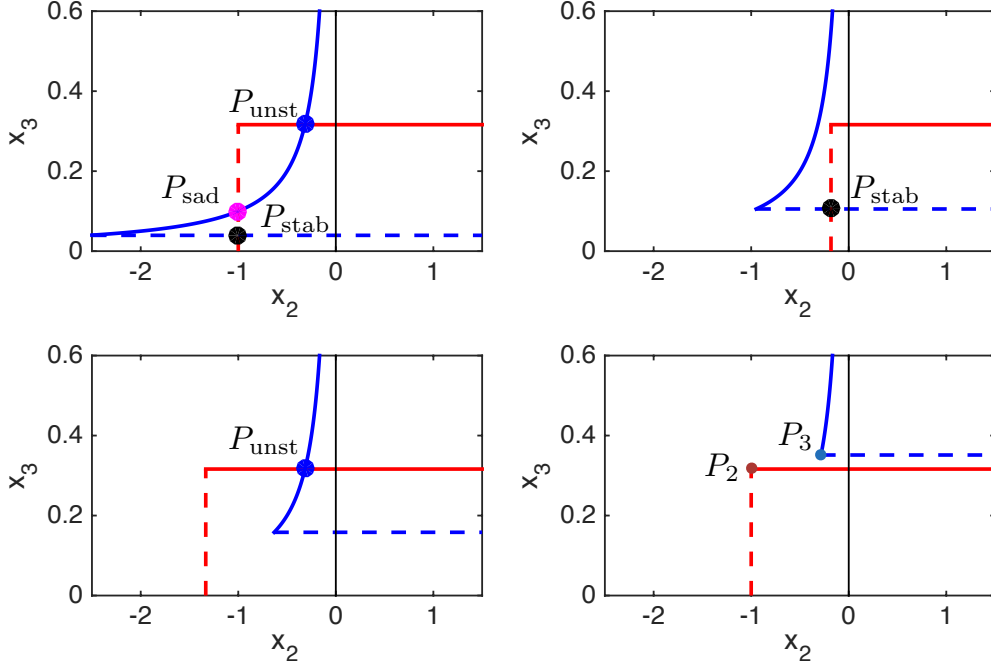


Figure 4.9: Four different configurations of nullclines. The red and blue lines correspond to nullclines for \dot{x}_2 and \dot{x}_3 , respectively. P_{stab} , P_{unst} , and P_{sad} denote stable node, unstable node, and saddle point, respectively.

The top two configurations in Fig. 4.9 have a stable manifold but the bottom two do not. The stable manifold exists if and only if point P_2 is above and to the right of point P_3 . Also, the stable node has to be in the negative x_2 region in order to

ensure target capture. The coordinates of those points are $P_2 = [v_{cl} + \bar{u}_T/N_r, \sqrt{\bar{u}x_1}]$, $P_3 = [-N_\theta x_1 \bar{u}/\bar{u}_T, \bar{u}_T/N_\theta]$, and $P_{\text{stab}} = [v_{cl} + \bar{u}_T/N_r, \bar{u}_T/N_\theta]$, assuming $\bar{u} \triangleq \bar{u}_P - \bar{u}_T > 0$.

Hence, the stability conditions required at each x_1 are

(a) the stable node must lie to the left of $x_2 = 0$, i.e.,

$$v_{cl} + \frac{\bar{u}_T}{N_r} < 0; \quad (4.34)$$

(b) P_2 must be above P_3 , i.e.,

$$\frac{\bar{u}_T}{N_\theta} < \sqrt{\bar{u}x_1}; \quad (4.35)$$

(c) and P_2 must be on the right side of P_3 , i.e.,

$$-N_\theta x_1 \frac{\bar{u}}{\bar{u}_T} < v_{cl} + \frac{\bar{u}_T}{N_r}. \quad (4.36)$$

Since conditions (b) and (c) become more stringent for smaller x_1 , the conditions are satisfied for all $x_1 > r_0$ if they are satisfied at $x_1 = r_0$. By choosing the parameter κ as $\kappa = |v_{cl}|^2/\bar{u}r_0$, the three conditions at $x_1 = r_0$ are rewritten as (a) $N_r > N_r^*$; (b) $N_\theta > N_\theta^*$; and (c) $\frac{N_\theta^*}{N_\theta} \left(1 - \frac{N_r^*}{N_r}\right) \sqrt{\kappa} < 1$. Note the first two conditions (a) and (b) are equivalent to condition (4.17). \square

Because control gains that satisfy (4.33) always exist, Proposition 4.2 ensures the pursuit law is robust to control saturation as long as the pursuer has maximum acceleration larger than the naive evader. Although we treated the effects of measurement error and control saturation separately in this section, the experimental

results presented in the following section demonstrate the robustness of the pursuit law to the combination of measurement error, unknown target maneuvers, and control saturation.

4.3 Experimental Results

The various pursuit laws described above were implemented using the autonomous hovercraft testbed. A motion-capture camera system was employed to position the vehicles to the desired initial conditions in the inertial frame, to command a repeatable trajectory for the target, and to analyze the pursuit performance by measuring the ground truth. Initial conditions and target trajectory identical to the numerical simulation were used.

4.3.1 Measurement Noise

Vision-based tracking like one used on the pursuer hovercraft is a low-power, lightweight tracking solution for a small, payload-limited platform. Measurements of the range and body-frame angle to the target from the pursuer are corrupted by limited camera resolution, occasional extraneous IR sources and reflections, and other random noise. Differentiation of this noisy signal to calculate the radial and angular velocities further exacerbates the high frequency noise. Table 4.1 shows the measurement errors across eighteen pursuit trials.

Figure 4.10-a shows an example of the measured states that are corrupted with noise. Due to the generally large size of e_2 and e_3 and infrequent extreme deviations

in e_3 , e_i often approaches x_i and even occasionally exceeds it, though the error-to-signal ratio is usually less than 0.5, as shown in Fig. 4.10-b. Hence, Assumption (A6) is marginally true for e_2 and e_3 . With the controller parameters $v_{cl} = -2$ (m/s) and $\kappa = 10$, the magnitudes of e_2 and e_3 agree with Assumption (A7) most of the time; $|e_2| > |v_{cl}|$ and $|e_3| > |v_{cl}|/\sqrt{\kappa}$ occurs only 0.42% and 0.73% of the time. We estimate the bounds as $e_2^* = 0.56$ (m/s) and $e_3^* = 0.30$ (m/s) using two standard deviations, which accommodates 97.6% and 95.4% of all errors. Assumption (A8) is reasonable since the upper bound on the vehicle speed (which limits x_3) and the lower bound on the range both exist in the hardware implementation. We estimate the maximum LOS angular rate as $\omega = 1$ (rad/s).

The control gains calculated from (4.15), (4.16) and (4.24) are $N'_r = 1.1$ and $N'_\theta = 12.4$; $N'_r = N'_\theta = 0.5$ from (4.17) when measurement error is ignored. Although the mean capture time from 10 experimental trials increased from 2.7 (s) with the former control gains to 3.2 (s) with the latter control gains, robust target capture was still achieved with the smaller gain setting, which implies that the condition to ensure robustness to measurement error may be conservative for this testbed.

Table 4.1: Characteristics of the State Measurement Errors

	Units	Mean	S.D.	Max.
e_1	m	0.023	0.031	0.14
e_2	m/s	0.112	0.289	2.26
e_3	m/s	-0.002	0.151	3.15

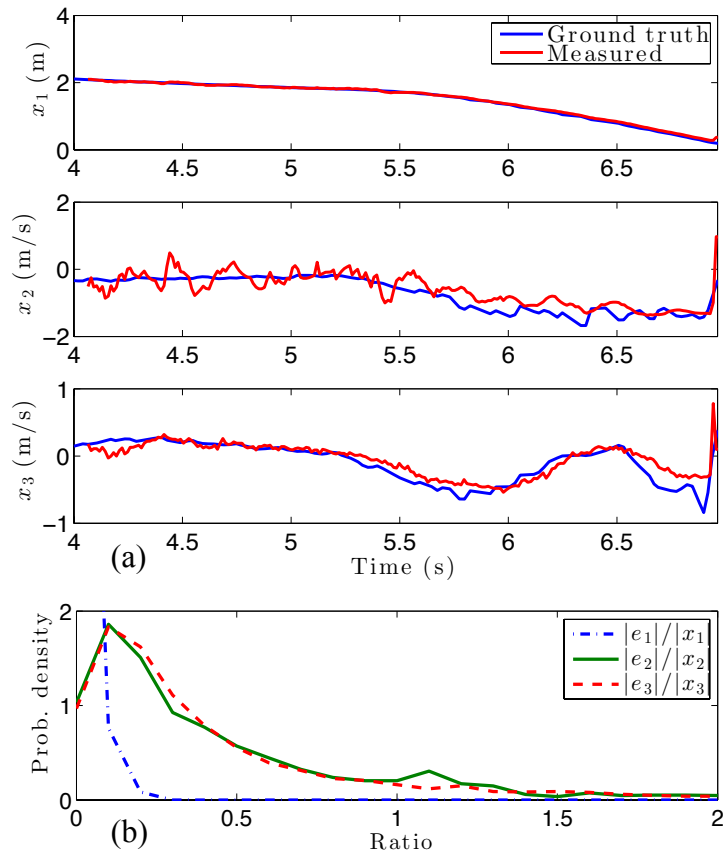


Figure 4.10: (a) Example of measured states corrupted with noise. (b) Probability density of error to signal ratio from 18 trials.

4.3.2 Comparison between Pursuit Laws

As in the numerical simulations, we ran each controller against a pre-programmed target trajectory and recorded the pursuer’s trajectory, onboard state measurements, and control effort. The parameters and control gains were identical to those in the numerical simulations. Figure 4.11 shows the results from conducting identical experimental trials for each law. Note that μ and σ in Fig. 4.11-d and -e are not the acceleration commands from the control law but those values after saturation at 1 (m/s^2) due to the limitation of the motor. We characterize controller perfor-

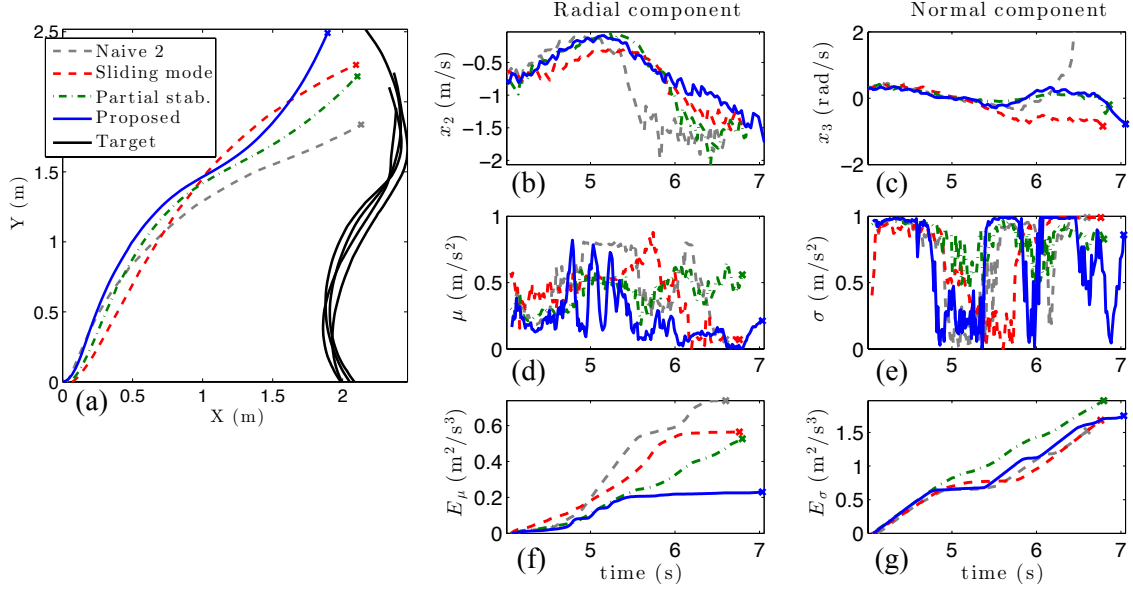


Figure 4.11: Experimental trial up until the first close encounter. Subfigures correspond to those in Fig. 4.6.

mances by capture time, maximum control command, and energy expenditure. As in Section 4.2, we are most interested in the maximum control command and energy expenditure since both the control authority and energy capacity are particularly limited on small vehicles. Each controller was run three times and the average of each of the above metrics is listed in Tab. 4.2. The symbols μ_{\max} , U_{\max} , E_{μ} , E_{tot} and T_{cap} denote maximum commanded radial acceleration, maximum commanded total acceleration, radial energy expenditure, total energy expenditure, and capture time, respectively. The bio-inspired controller has the smallest acceleration, the smallest energy expenditures, and the longest capture time. The naive pursuit law has the shortest capture time and the largest energy expenditure.

4.3.3 Comparison with Theory

Our experimental pursuit implementation revealed several insights as compared to analytical and numerically simulated results. First, the experiments provide a realistic baseline for noise in small, low-cost, vision-based sensors used in pursuit. As expected, differentiated rate measurements like x_2 and x_3 are significantly noisier than direct range or angle measurements, like x_1 , when using vision sensors such as the camera on the pursuer. Though the magnitude of the noise in x_2 and x_3 violated the theoretical assumptions, the controllers' success demonstrate that a well-designed controller may still reliably achieve target capture outside of the guaranteed operating regime.

Second, actuator saturation due to limited actuator authority changed controller performance as compared to simulation, emphasizing the importance of a low, maximum commanded acceleration. Since no bound is assumed on pursuer acceleration in the controller derivations, unachievable acceleration magnitudes might be commanded. This problem is exacerbated by sensor noise, which may produce erroneously large state measurements and corresponding large fluctuations in accel-

Table 4.2: Performance of various pursuit laws

	μ_{\max} (m/s ²)	U_{\max} (m/s ²)	E_{μ} (m ² /s ³)	E_{tot} (m ² /s ³)	T_{cap} (s)
Proposed	0.81	3.70	0.30	1.80	3.16
Partial stab.	1.18	5.46	0.53	2.48	2.90
Sliding mode	1.13	6.63	0.68	2.02	2.88
Naive	0.80	6.70	0.79	2.38	2.75

eration commands. In the experimental implementation, overly large acceleration commands are saturated by scaling down to the maximum achievable acceleration magnitude while maintaining the original direction. In particular, saturation modified the achieved acceleration when either μ or σ exceeded the maximum acceleration magnitude. This effect is observed in the experimental σ acceleration, in which the controllers differ from each other earlier in pursuit than they do in simulation. The effects of actuator limits may be avoided or mitigated by limiting the maximum commanded acceleration or by different scaling and saturating strategies when unachievable accelerations are commanded.

Chapter 5

Mosquito-Inspired Swarming for Decentralized Pursuit

The previous chapter considered an individual pursuit problem assuming that the target is always perceived by the pursuer. Using the definition in Chapter 3, the previous problem corresponds to *Phase 3* in the mosquito pursuit behavior, i.e., the phase after the close encounter. This chapter considers a pursuit problem that also includes the *swarming phase*, where male mosquitoes have not yet perceived the female mosquito. We study how swarming motion in autonomous vehicles helps the success of target capture, by considering the scenario in which multiple guardians with limited perceptual range and bounded acceleration are deployed to protect an area from an intruder. Section 5.1 introduces the novel pursuit problem inspired by the collective behaviors in mosquito swarms. Section 5.2 performs analyses of the problem to quantify how difficult it is to capture the target depending on the system parameters. Section 5.3 presents various swarming strategies that are designed to maximize the probability of capturing the intruder, and illustrates the perfor-

mance with numerical simulations. Section 5.4 validates the theoretical results with experiments using an indoor quadrotor swarm.

5.1 Background

This section introduces a novel pursuit problem involving a swarm of guardians and intruders. We begin by discussing how this problem is inspired by the collective behaviors in mosquito swarms.

5.1.1 Inspiration from Mosquitoes

Section 1.2.2 categorized pursuit problems by the definition of capture (intercept or tracking) and the agents' capabilities (dynamics and sensing). Wild swarms of malarial mosquitoes show an interesting combination of these categories, which motivates the formulation of a new type of pursuit problem. Male mosquitoes aggregate and form mating swarms to attract female mosquitoes that fly faster than the males. In this stage, which we call the *swarming phase*, male mosquitoes cooperate with one another to increase the chance of encounter with a female. When the female enters the swarm, male's pursuit behavior is triggered only when the distance to the female becomes small, which we call the *close encounter*. This switching in the male's behavior indicates that they have limited perceptual range to detect the female.

After the pursuit phase, the male and the female exhibit coupling flight during which they fly in approximately the same direction while their separation distance

oscillates—as though they are connected by a damped spring with zero rest length (see Chapter 3). For a male to achieve this flight, simply intercepting a female is insufficient; he also has to align his velocity with the female. For this reason, the objective of the mosquito pursuit is a combination of target tracking and intercept. In addition, since the female flies faster than a swarming male, a male has to accelerate after the close-encounter in order to successfully track the female. Therefore, the mosquito pursuit has to be modeled with agents with variable speed.

The combination of limited perceptual range and the dynamical model of the agent raises the importance of quick response, i.e., when a male detects a female, it has to speed up and match the velocity of a fast female in time so that the female does not escape from its perceptual range. The velocity matching may also require favorable initial conditions for the male, i.e., its initial velocity should be relatively aligned with female. This observation motivates our investigation below of swarming rather than static guardians.

Although the pursuit law that governs the motion of mosquitoes in the pursuit phase is an interesting topic, we focus on the swarming phase in this work. (See Chapter 4 for the work on pursuit after detection.) A key characteristic of insect swarms is their unpolarized oscillatory motion [23], in contrast to fish schools [6], bird flocks [3], and formation controls inspired by those animals [26, 94]. The oscillatory motion and the interactions between males have been studied in Chapter 2, and it was suggested in Chapter 3 that this motion may increase the sensitivity to external stimuli, for example, to respond quickly to a female that enters the swarm (also see the discussion in [9]).

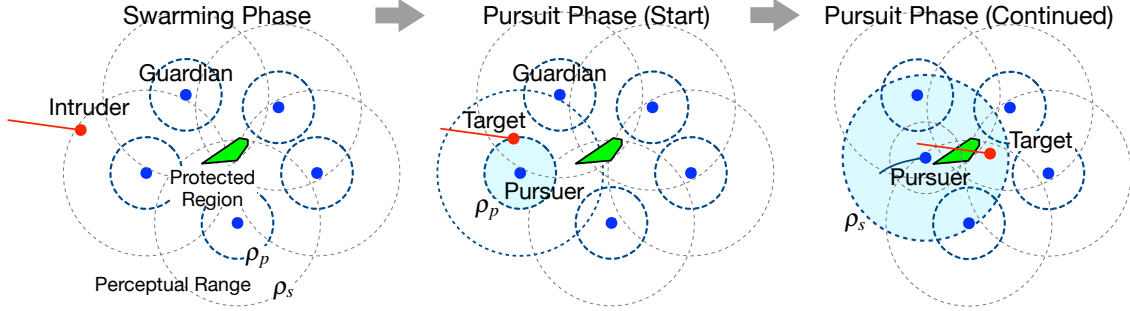


Figure 5.1: Illustration of the swarming and pursuit scenario. In the swarming phase, an intruder (red) is approaching the protected region (green). The guardians (with static formation here for clarity) are deployed to wait for the intruder. Once the intruder enters the perceptual range, the guardian turns into a pursuer and the intruder becomes the target.

Inspired by the mosquito behavior, we study how swarming motion may be useful in a scenario where multiple pursuers with limited perceptual range wait for a fast target that comes from an unknown direction at an unknown time. The goal of the pursuers is to track the target, so simply blocking the target by constructing a wall-like formation will not achieve the goal. Instead, the pursuer has to match its velocity with the target.

5.1.2 Problem Formulation

Consider a planar system of point particles with unit mass representing N_P guardians and N_T intruders (we use the subscripts T and P to denote the intruder/target and guardian/pursuer, respectively). The intruders seek to pass through a protected region that is known to the guardians. Figure 5.1 illustrates the case where only one intruder is seen in the picture. The timing and the direction of the intruder trajectories are unknown to the guardians. Once the intruder enters the perceptual range of a guardian, the roles of the agents change—the intruder becomes a target and the

guardian becomes a pursuer. The goal of the pursuer is to capture the target (i.e., approach the target and stay close to it). Although the difference between target capture that occurs before and after the intrusion is important to some applications, and is a subject of our ongoing work (see Section 6.2 for our preliminary work), we do not distinguish between those two cases here.

Consider the case where the protected region is sufficiently small to be approximated as a point O . Let O to be the origin of the inertial frame; \mathbf{r}_i , \mathbf{v}_i , and \mathbf{a}_i denote the position, velocity, and acceleration of particle i in the inertial frame. The agents have second-order dynamics, i.e., $\dot{\mathbf{r}}_i = \mathbf{v}_i$ and $\dot{\mathbf{v}}_i = \mathbf{a}_i$. We assume the following capabilities of the guardians:

- (A1) The magnitude of the guardian’s acceleration is bounded according to $\|\mathbf{a}_P\| \leq \bar{u}_P$; and
- (A2) Each guardian perceives the position and velocity of all other agents within the range ρ_s .

We also introduce another perceptual range that determines when the pursuit behavior is triggered:

- (A3) Each guardian becomes a pursuer once the distance to an intruder becomes less than ρ_p .

The threshold ρ_p is inspired by the observation that the pursuit behavior of a male mosquito is triggered by the *close encounter* with a female (see the swarm model in Section 3.4). We also note that the parameter ρ_p allows two interpretations.

First, it can be interpreted as the limitation of the guardians to distinguish between a friendly guardian vehicle and the intruder, i.e., guardian i does not know whether an agent j (in its perceptual range) is an intruder or not if $\rho_p < \|\mathbf{r}_{j/i}\| < \rho_s$, where $\mathbf{r}_{j/i} = \mathbf{r}_j - \mathbf{r}_i$. Second, ρ_p may be a control parameter that the guardian can choose; i.e., the guardian will ignore the intruder unless it gets closer than the distance ρ_p . In either case, the value of ρ_p will not exceed ρ_s .

In contrast to target *intercept* where pursuers aim to collide into the target, we consider target *tracking*, defined as follows.

Definition 5.1. Let $\mathbf{r}_{T/P} = \mathbf{r}_T - \mathbf{r}_P$ denote the relative position of the target with respect to the pursuer. Let $r_{\text{cap}} > 0$ denote the capture threshold. Target capture is successful if there exists t_{cap} such that $\|\mathbf{r}_{T/P}\| < r_{\text{cap}}$, for all $t > t_{\text{cap}}$.

From assumption (A2), the pursuit can last as long as the target is in the range ρ_s . Therefore, we choose the threshold in Definition 5.1 to be $r_{\text{cap}} = \rho_s$.

The capture problem can be separated into two parts. The first is the *swarming phase* in which the guardian does not know where the intruder is. Once the intruder enters the circle with radius ρ_p around a guardian, the *pursuit phase* starts. Although we discuss the control law for the pursuit phase in Section 5.2.2, our focus here is on the swarming phase. The success of target capture depends on how quickly a guardian can respond (i.e., close the distance and match the velocity) to the intruder once it is in perceptual range ρ_p . If the response is too slow, then the target will escape from the range ρ_s . We seek to find a strategy for how the guardians should prepare for the intruder to maximize the probability of target capture.

Table 5.1: List of system parameters and their nominal values.

Symbol	Description	Nominal Value
N_P	Number of guardians	10
\bar{u}_P	Maximum acceleration	2.7
ρ_s	Perceptual range	1
ρ_p	Threshold for close encounter	0.5
N_T	Number of intruders	1
v_T	Intruder speed	3

To focus on the guardians' strategy, assume that the intruder moves with a constant velocity $\|\mathbf{v}_T\| = v_T$ on a straight path that passes through O . Note that even with this simplification, the intruders can take variety of different strategies in terms of the directions from which they approach O , and also the timing of their arrival. Let t_j^{int} and ψ_j^{int} denote the time and azimuthal direction that the j th intruder arrives at O (assuming it is not captured), and let $T_j^{\text{int}} = t_{j+1}^{\text{int}} - t_j^{\text{int}}$ denote the time interval between two successive intruders. The sets $\{\psi_j\}$ and $\{T_j^{\text{int}}\}$ significantly affect the success rate of pursuit. This chapter studies the case where T_j^{int} is sufficiently large that each intruder may be considered separately. This scenario can be approximated as a single-intruder case, i.e., $N_T = 1$. (The effects of $\{\psi_j\}$, $\{T_j^{\text{int}}\}$, and N_T are subjects of ongoing work. Our preliminary results can be found in [95].) Table 5.1 lists the parameters that are introduced in this section.

5.2 Control Theoretic Analysis

This section describes a condition for when the target capture fails by a static guardian, and introduces nondimensional parameters that describe the difficulty

of target capture. We then derive sufficient conditions for target capture, which motivate the swarming algorithms in the sequel.

5.2.1 Limitation of Static Guardian

A naive strategy is to uniformly distribute stationary guardians around the protected area as in Fig. 5.1 and wait for the intruder. However, if the intruder is too fast, the guardian may not react (i.e., speed up and align its velocity) in time to keep the intruder in the perceptual range. We first find the necessary condition for a static guardian to achieve target capture.

Proposition 5.1. *A guardian who is stationary at the beginning of the pursuit phase never achieves target capture if*

$$\bar{u}_P < \frac{v_T^2}{2(\rho_p + \rho_s)}. \quad (5.1)$$

Proof. Consider the easiest case for the pursuer: the target trajectory passes through the pursuer’s position. Let $t_f = v_T/\bar{u}_P$ denote the time required for the pursuer to reach the speed v_T . The target escapes if it can travel a distance longer than $\rho_p + \rho_s + \frac{1}{2}\bar{u}_P t_f^2$ within a duration of time t_f . The inequality $v_T t_f > \rho_p + \rho_s + \frac{1}{2}\bar{u}_P t_f^2$ reduces to (5.1). \square

The above condition is given in terms of the intruder’s speed v_T and the guardian’s capability \bar{u}_P , ρ_s , and ρ_p . To explore this parameter space efficiently in

Table 5.2: List of nondimensionalized system parameters that describe the difficulty of target capture and their nominal values.

Symbol	Description	Nominal Value
N_P	Number of guardians	10
Γ	Guardian acceleration	0.9
α	Pursuit activation distance	0.5

the following sections, we introduce the following two nondimensional parameters:

$$\alpha = \frac{\rho_p}{\rho_s} \quad \text{and} \quad \Gamma = \frac{2\bar{u}_P(\rho_s + \rho_p)}{v_T^2}. \quad (5.2)$$

The first parameter $\alpha \in (0, 1]$ is the *pursuit activation distance*, which describes the ratio between the two perceptual ranges defined in assumptions (A2) and (A3). The second parameter Γ is the nondimensionalized *guardian acceleration*, which describes the ratio between the guardian’s capability and the intruder’s speed. Noting that Γ is obtained from the limiting case in (5.1), a static guardian will fail to capture a target if $\Gamma < 1$. (We introduce an augmented version of Γ considering the effect of time delay in Section 5.4.3.)

For the case with infrequent intruders (or equivalently $N_T = 1$), the difficulty of target capture can be completely described by the two nondimensional parameters α and Γ and the number of guardians N_P , which we summarize in Tab. 5.2 with nominal values derived from the dimensional parameters in Tab. 5.1. For the frequent-intruders case, the number of intruders N_T as well as their strategies ($\{\psi_j^{\text{int}}\}$ and $\{T_j^{\text{int}}\}$, see Section 5.1.2) determine the difficulty of target capture.

5.2.2 Sufficient Conditions for Target Capture

Next, we derive a sufficient condition for target capture. Since the condition will be given for the relative velocity $\mathbf{v}_{T/P}$ at the time of *close encounter* (i.e., the initial condition of the pursuit phase), it applies to any guardian strategy in the swarming phase. Based on this general condition, we consider two cases: a static swarm and a swarm with a circling motion.

As a pursuit law, $\mathbf{a}_P = \mathbf{F}_P^{(\text{pursuit})}$, following the mosquito-inspired swarm model in Chapter 3, consider a force resembling a damped-spring attached to the target, i.e.,

$$\mathbf{F}_P = c\mathbf{r}_{T/P} + b\mathbf{v}_{T/P},$$

where c and b are positive constants. The spring term alone never exceeds the acceleration limit \bar{u}_P with the following constraint:

$$0 < c < \frac{\bar{u}_P}{\rho_s}. \quad (5.3)$$

In this case, there always exists a scaling factor $\beta \in (0, 1]$ such that

$$\|c\mathbf{r}_{T/P} + \beta b\mathbf{v}_{T/P}\| \leq \bar{u}_P. \quad (5.4)$$

In this way, the actual pursuit force is saturated as follows:

$$\mathbf{F}_P^{(\text{pursuit})} = c\mathbf{r}_{T/P} + \beta b\mathbf{v}_{T/P}, \quad (5.5)$$

$$\beta = \begin{cases} 1 & \text{if } \|\mathbf{c}\mathbf{r}_{T/P} + \mathbf{b}\mathbf{v}_{T/P}\| < \bar{u}_P, \\ \beta^* & \text{otherwise,} \end{cases}$$

where $\beta^* > 0$ is the maximum value of β that satisfies the equality in (5.4). The value of β^* as a function of $\mathbf{r}_{T/P}$, $\mathbf{v}_{T/P}$, c and b can be obtained using Stewart's theorem in geometry (see Appendix A.1). Although mosquitoes exhibit underdamped oscillation (see Chapter 3), for the application to guardians, a large number for b (i.e., an over-damped spring) gives good performance since velocity alignment is necessary for target capture. (Instability caused by the time delay also has to be taken into account for the gain tuning, in practice.) However, the following proposition gives a sufficient condition for target capture, which is independent of the choice of c and b as long as (5.3) is satisfied.

Proposition 5.2. *Consider a pursuer under (5.5) with the gain c satisfying (5.3).*

Let t_0 denote the time when $\|\mathbf{r}_{T/P}\| = \rho_p$ (i.e., the time when the pursuit phase starts). The target capture is guaranteed if

$$\|\mathbf{v}_{T/P}(t_0)\| \leq v_0, \quad \text{where } v_0 = v_T \sqrt{\frac{\Gamma(1-\alpha)}{2}}. \quad (5.6)$$

Proof. Consider the energy function

$$V = \frac{1}{2} \|\mathbf{r}_{T/P}\|^2 + \frac{1}{2c} \|\mathbf{v}_{T/P}\|^2.$$

Since the target is not accelerating, the time derivative of V satisfies

$$\begin{aligned}
c\dot{V} &= \mathbf{c}\mathbf{r}_{T/P} \cdot \mathbf{v}_{T/P} + \mathbf{v}_{T/P} \cdot (\mathbf{a}_T - \mathbf{a}_P) \\
&= \mathbf{c}\mathbf{r}_{T/P} \cdot \mathbf{v}_{T/P} - \mathbf{v}_{T/P} \cdot (\mathbf{c}\mathbf{r}_{T/P} + \beta b \mathbf{v}_{T/P}) \\
&= -\beta b \|\mathbf{v}_{T/P}\|^2.
\end{aligned}$$

Thus, V is nonincreasing for all $t > t_0$. It follows that

$$\frac{1}{2} \|\mathbf{r}_{T/P}(t)\|^2 \leq V(t) \leq V(t_0) = \frac{1}{2} \rho_p^2 + \frac{1}{2c} \|\mathbf{v}_{T/P}(t_0)\|^2.$$

We obtain $\|\mathbf{r}_{T/P}(t)\| \leq \rho_s$ for all $t > t_0$ if the right hand side of the above inequality is bounded by $\frac{1}{2} \rho_s^2$, i.e.,

$$\begin{aligned}
\frac{1}{2} \rho_p^2 + \frac{1}{2c} \|\mathbf{v}_{T/P}(t_0)\|^2 &\leq \frac{1}{2} \rho_s^2 \\
\|\mathbf{v}_{T/P}(t_0)\| &\leq \sqrt{c(\rho_s^2 - \rho_p^2)}
\end{aligned}$$

Noting (from definitions of Γ and α) that

$$\frac{\bar{u}_P}{\rho_s} (\rho_s^2 - \rho_p^2) = v_T^2 \frac{\Gamma(1 - \alpha)}{2},$$

the above inequality is equivalent to (5.6) with the constraint (5.3). \square

If the pursuer's velocity $\mathbf{v}_P(t_0)$ at the time of close encounter lies in the circle

$$B_{v_0}(\mathbf{v}_T(t_0)) \equiv \{\mathbf{v} \mid \|\mathbf{v} - \mathbf{v}_T(t_0)\| \leq v_0\},$$

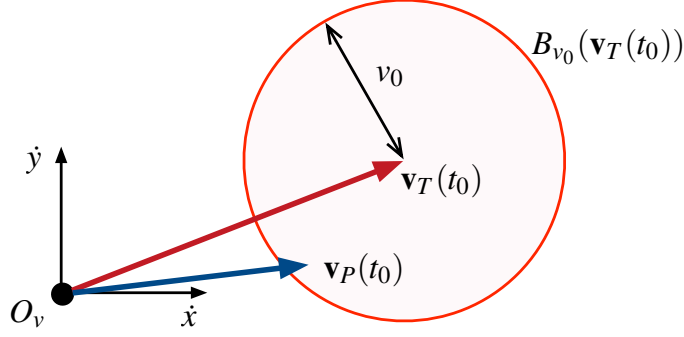


Figure 5.2: Sufficient condition on the initial velocity for target capture depicted in the velocity space. Target capture is guaranteed if the pursuer’s velocity (blue arrow) lies in the red circle at the beginning of the pursuit phase.

which is centered at $\mathbf{v}_T(t_0)$ with radius v_0 (see Fig. 5.2), the target capture is guaranteed. If Γ is sufficiently large that the origin of the velocity space (O_v in Fig. 5.2) is included in $B_{v_0}(\mathbf{v}_T(t_0))$, even a static pursuer can guarantee target capture. This case is stated in the following result.

Corollary 5.1. *Target capture is guaranteed by a pursuer that is stationary at the beginning of the pursuit phase if the following condition is satisfied:*

$$\Gamma > \frac{2}{1 - \alpha}. \quad (5.7)$$

Proof. From Proposition 5.2 and the discussion above, the sufficient condition is $v_0 > v_T$, which reduces to (5.7). \square

One strategy to achieve the velocity alignment derived in Proposition 5.2 is to use a circling motion. The target capture is guaranteed if the circling motion has (i) a radius less than ρ_p so that O is always in the perceptual range; (ii) sufficient speed such that $\|\mathbf{v}_P\| \in (v_T - v_0, v_T + v_0)$; and (iii) there are sufficiently many guardians

so that there exists one whose direction of motion is approximately aligned with \mathbf{v}_T when the intruder passes through O . Assuming (iii) is true, the conditions (i) and (ii) give the following result.

Corollary 5.2. *Assuming that there are sufficiently many guardians so that there always exists one whose direction of motion is approximately aligned with \mathbf{v}_T , a circular motion around O guarantees target capture if*

$$\sqrt{\frac{\Gamma}{2}} \left(\sqrt{\frac{\alpha}{1+\alpha}} + \sqrt{1-\alpha} \right) > 1. \quad (5.8)$$

Proof. Given the smallest required speed $v_T - v_0$ and the acceleration bound \bar{u}_P , the radius of the circular orbit has to be greater than $(v_T - v_0)^2 / \bar{u}_P$ to be able to counteract the centrifugal acceleration. From condition (i), the radius also has to be smaller than ρ_p . Therefore, the condition is $\rho_p > (v_T - v_0)^2 / \bar{u}_P$, which is equivalent to (5.8). \square

The analysis on the required number of guardians for condition (iii) to hold is presented in the Appendix A.2.

The necessary and sufficient conditions (5.1), (5.7) and (5.8) are summarized in Fig. 5.3. Region \mathcal{R}_1 is where a static swarm fails to achieve target capture. Region \mathcal{R}_3 is where a static swarm is guaranteed to achieve target capture, assuming that the intruder encounters at least one guardian. The region $\mathcal{R}_2 \cup \mathcal{R}_3$ is where a circling swarm is guaranteed to achieve target capture. The circling motion guarantees target capture with lower Γ as compared to a static swarm. If Γ is below the red

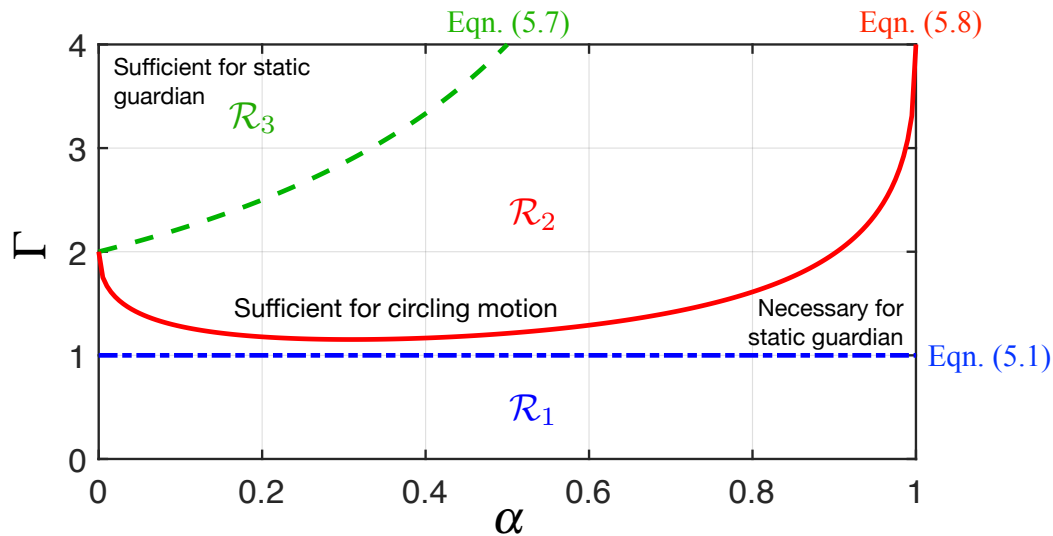


Figure 5.3: Conditions for target capture in the nondimensional parameter space: \mathcal{R}_1 is where the static formation never achieves target capture; \mathcal{R}_2 is where target capture is guaranteed by circling formation; \mathcal{R}_3 is where the static formation guarantees target capture.

curve in Fig. 5.3, guardians cannot achieve the desired circular motion; i.e., either the radius is too large or the speed is too low. The following section proposes strategies for the guardians so that they can achieve target capture even inside of the region \mathcal{R}_1 .

5.3 Algorithms and Simulation Results

This section considers the strategies for the guardians in the swarming phase to achieve target capture even when $\Gamma < 1$. We describe the probabilistic nature of the problem, and state the objectives of the swarming motion. The first strategy considers various orbiting motion around O . Next, we propose strategies inspired by mosquito behavior: random oscillatory motion and velocity-alignment behavior. The performance of the strategies, in terms of the probability of target capture, is

studied with numerical simulations.

5.3.1 Orbiting Strategy

In the previous section, Proposition 5.2 showed that target capture can be achieved if the velocities of the guardian and the target at the time of close encounter are aligned so that the relative velocity is sufficiently small. This condition suggests the importance of the guardians maintaining sufficiently high velocity during the swarming phase. In addition, the condition prerequisite to velocity matching is that the close encounter occurs. Therefore, the two key objectives of the swarming motion are to (i) maintain high density around O where the intruder passes through; and (ii) maintain high speed that can lie in the circle $B_{v_0}(\mathbf{v}_T)$.

Note that now the problem of target capture is probabilistic. Each guardian may encounter an intruder with probability P_{enctr} , and the velocity at the time of close-encounter may lie in $B_{v_0}(\mathbf{v}_T)$ with probability P_{align} . Since target capture occurs if those two occur for any of the guardians, the probability of target capture P_{cap} is dictated by P_{enctr} and P_{align} . For the same number N_P of guardians, P_{cap} may be increased by improving P_{enctr} and P_{align} , as discussed below.

The control law for the guardian is described by the combination of artificial forces \mathbf{F}_i that generates the desired acceleration \mathbf{a}_i of the agent. The overall forcing on agent i is given by

$$\mathbf{a}_i = \mathbf{F}_i = (1 - \lambda_i^P) \mathbf{F}_i^{(\text{swarm})} + \lambda_i^P \mathbf{F}_i^{(\text{pursuit})}, \quad (5.9)$$

where the switching parameter $\lambda_i^P \in \{0, 1\}$ takes the value $\lambda_i^P = 0$ (resp. 1) in the swarming (resp. pursuit) phase. The pursuit term $\mathbf{F}_i^{(\text{pursuit})}$ is defined in (5.5).

We first consider a central force $\mathbf{F}_i^{(\text{swarm})} = \mathbf{F}_i^{(\text{cent})}$ that generates oscillatory motion of the guardians around O , where $\mathbf{F}_i^{(\text{cent})} = -k_c \mathbf{r}_i$. Since the guardian's acceleration is bounded, the central force on agent i will be saturated as follows:

$$\mathbf{F}_i^{(\text{cent})} = \begin{cases} -k_c \mathbf{r}_i & \text{if } \|k_c \mathbf{r}_i\| \leq \bar{u}_P, \\ -\bar{u}_P \mathbf{r}_i / \|\mathbf{r}_i\| & \text{otherwise.} \end{cases} \quad (5.10)$$

For simplicity, consider the case where k_c is sufficiently large that $\mathbf{F}_i^{(\text{cent})}$ is always saturated. Depending on the initial condition, the central force $\mathbf{F}_i^{(\text{cent})}$ produces various orbiting motions characterized by the speed v_{\max} and the distance from the center $R_{\min} \in [0, v_{\max}^2 / \bar{u}_P]$ when the agent is closest to the center (see Fig. 5.4-a). Two extreme cases are (i) $R_{\min} = 0$, corresponding to a pure radial motion, and (ii) $R_{\min} = v_{\max}^2 / \bar{u}_P$, corresponding to a pure circular motion. The set (R_{\min}, v_{\max}) not only affects the shape of the orbit, but also modulates the speed and the density of the swarm. Figure 5.5-c and -d shows P_{cap} obtained from numerical simulation with $N_P = 12$, $\alpha = 0.5$, and two values of Γ : 0.5 and 0.9. Although Γ is in region \mathcal{R}_1 for both cases, target capture is achieved with nonzero probability if the set (R_{\min}, v_{\max}) is chosen properly. Although the probability is higher with larger Γ , the optimal (R_{\min}, v_{\max}) varies with Γ . In particular, for $\Gamma = 0.5$, circling motion is not optimal; the probability of capture is maximized for a blended motion in Fig. 5.4-b.

To further investigate how the optimal orbiting motion varies with Γ and α ,

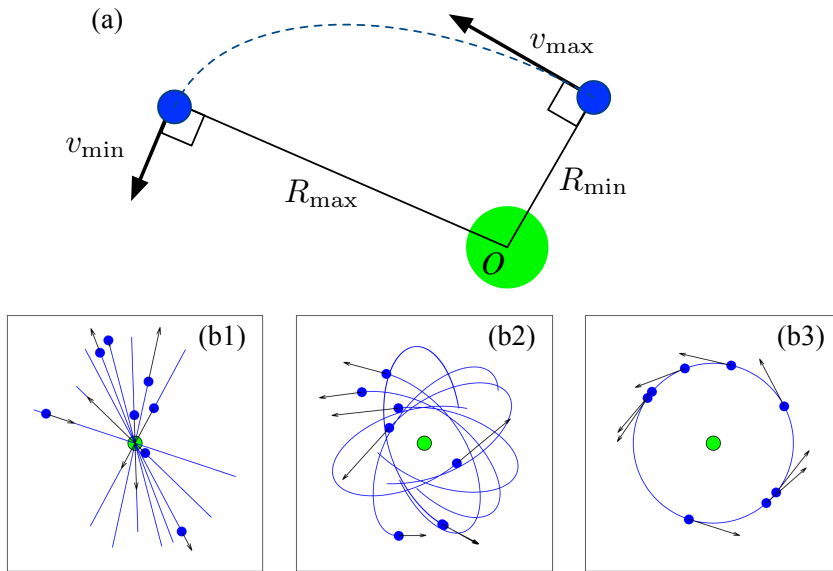


Figure 5.4: Effect of initial conditions on the orbiting motion. (a) The definition of v_{\max} and R_{\min} ; guardians' trajectories in (b1) radial motion; (b2) general case; (b3) circular motion.

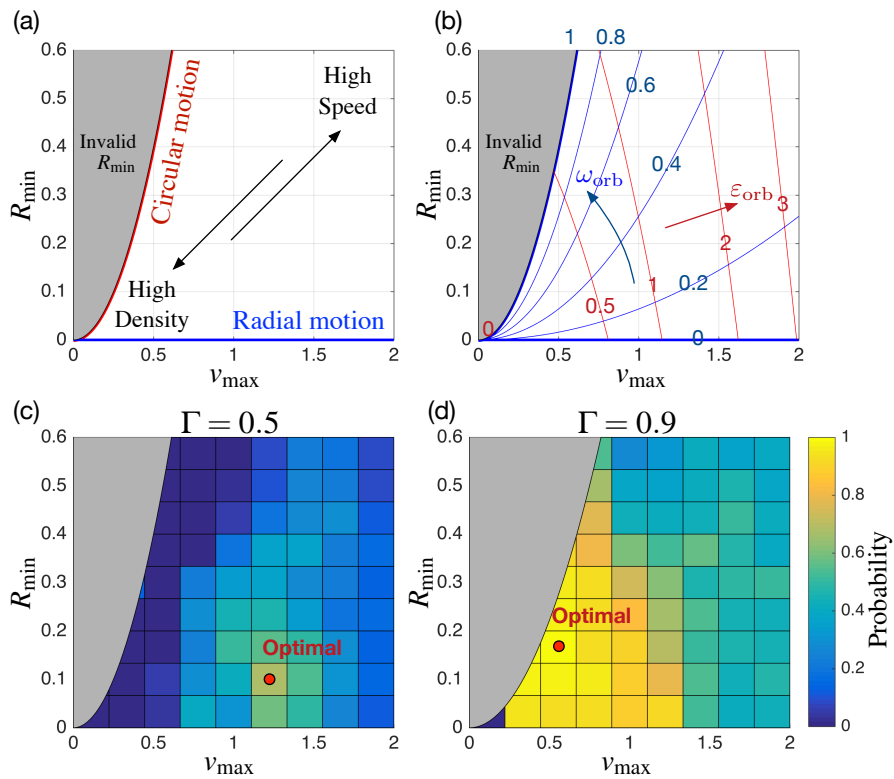


Figure 5.5: Effect of swarming motion on the probability of target capture. The boundary of the gray region is where the motion is circular.

two nondimensional parameters describe the energy and roundness of the orbits.

Consider the following energy function:

$$E(v, \rho) = \frac{1}{2}v^2 + U(\rho), \quad (5.11)$$

where positive semidefinite function $U(\rho)$ denotes the potential energy. Since a large k_c so that $\|\mathbf{F}_i^{(\text{cent})}\| = \bar{u}_P$ is assumed, we choose $U(\rho) = \bar{u}_P \rho$. Now, consider the baseline energy $E_0 = E(v_T - v_0, \rho_p)$ corresponding to the circling motion considered in Corollary 5.2. The nondimensional parameter $\varepsilon_{\text{orb}} > 0$ describes the energy of the given orbit normalized by the baseline energy, i.e.,

$$\varepsilon_{\text{orb}} \triangleq \frac{E(v_{\text{max}}, R_{\text{min}})}{E_0} = \frac{E(v_{\text{max}}, R_{\text{min}})}{E(v_T - v_0, \rho_p)}. \quad (5.12)$$

Remark 5.1. *If k_c is sufficiently small so that $\mathbf{F}_i^{(\text{cent})}$ is never saturated, then we choose $U(\rho) = \frac{k_c}{2}\rho^2$. For a general case we can use*

$$U(\rho) = \begin{cases} \frac{k_c}{2}\rho^2 & \text{if } |\rho| < \bar{u}_P/k_c, \\ \bar{u}_P \left(\rho - \frac{\bar{u}_P}{2k_c} \right) & \text{otherwise.} \end{cases}$$

For the roundness of the orbit, consider the speed required to achieve a pure circular motion, i.e., $v_{\text{max}}^* = \sqrt{\bar{u}_P R_{\text{min}}}$. The nondimensional parameter $\omega_{\text{orb}} \in [0, 1]$ defined by

$$\omega_{\text{orb}} \triangleq \frac{v_{\text{max}}^*}{v_{\text{max}}} = \frac{\sqrt{\bar{u}_P R_{\text{min}}}}{v_{\text{max}}} \quad (5.13)$$

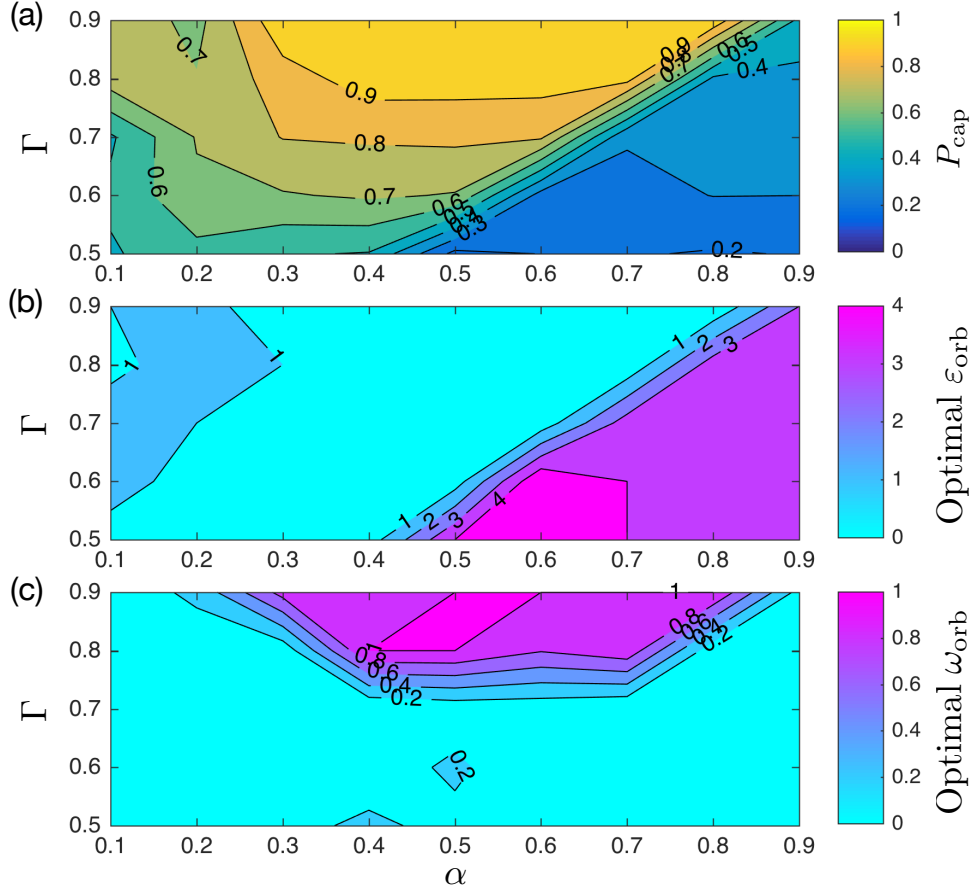


Figure 5.6: Optimal orbiting motion as a function of system parameters Γ and α : (a) P_{cap} achieved with optimal orbiting motion; (b) optimal energy ε_{orb} ; (c) optimal roundness ω_{orb} .

describes the degree of roundness scaled between 0 (pure radial motion) and 1 (pure circular motion). The level curves of ε_{orb} and ω_{orb} are depicted in Fig. 5.5-b.

Remark 5.2. *A point in $(v_{\text{max}}, R_{\text{min}})$ -space is mapped to a unique point in $(\varepsilon_{\text{orb}}, \omega_{\text{orb}})$ -space and vice versa through (5.12) and (5.13), except for the origin, which is mapped to the line $\varepsilon_{\text{orb}} = 0$.*

Figure 5.6 shows the optimal values of ε_{orb} and ω_{orb} as a function of the system parameters α and Γ . Figure 5.6-b shows that the swarm has to increase the energy, ε_{orb} , for small Γ and large α . Since the energy is increased at the cost of swarm

density (which causes a drop in P_{enctr}), we see low values of P_{cap} in the corresponding region in Fig. 5.6-a. Figure 5.6-c shows that the pure circular motion is only optimal in the subset of the (α, Γ) -space.

Consider the case where guardian-vehicles have fixed values of α and \bar{u}_P , and intruders may have different speeds v_T that are approximately known a priori. For the guardians to respond optimally to different intruders (i.e., different Γ values), the swarm has to be able to change the orbiting motion between radial and circular. A control law that can modulate the balance between the radial and rotational component of the swarming motion while avoiding collisions is presented with some earlier version of the experimental results in [61] and [<https://youtu.be/Hova4bMiVZg>].

5.3.2 Random-Swarming Strategy

The orbiting motion enables the guardians to capture the target even when $\Gamma < 1$, however, the approach has two disadvantages. First, for orbits that are close to radial motion, there is a high risk of collision near the center. Second, since the orbiting motion is deterministic (except for the initial conditions), the strategy and its weaknesses may be detected by the intruders in practice (e.g., intruder may try to approach O on the side opposing the direction of rotation). To overcome these disadvantages, this section presents another swarming algorithm.

The swarming algorithm $\mathbf{F}_i^{(\text{swarm})}$ consists of three forces; central, spacing, and random force, i.e.,

$$\mathbf{F}_i^{(\text{swarm})} = \mathbf{F}_i^{(\text{cent})} + \mathbf{F}_i^{(\text{spac})} + \mathbf{F}_i^{(\text{rand})}. \quad (5.14)$$

The central force $\mathbf{F}_i^{(\text{cent})}$ resembling a damped spring attached to O maintains the cohesiveness of the swarm:

$$\mathbf{F}_i^{(\text{cent})} = -k_c \mathbf{r}_i - b_c \mathbf{v}_i, \quad (5.15)$$

where positive constants k_c and b_c are the spring and damping constants.

The spacing force $\mathbf{F}_i^{(\text{spac})}$, which also resembles a damped spring, generates attraction, repulsion, and alignment behavior between the agents:

$$\mathbf{F}_i^{(\text{spac})} = -k_s \sum_{j \in S_i^{(\rho_0)}} \left(1 - \frac{x_0}{\|\mathbf{r}_{i/j}\|} \right) \mathbf{r}_{i/j} - b_s \mathbf{v}_{i/j}. \quad (5.16)$$

The positive parameter x_0 denotes the rest length of the spring, and the set $S_i^{(\rho_0)} = \{ j \mid \|\mathbf{r}_{i/j}\| \leq \rho_0 \}$ consists of all the agents within the range ρ_0 from agent i . By choosing x_0 to satisfy $(\rho_0 - x_0)/\rho_0 \ll 1$, the guardians may form a crystalized formation shown in Fig. 5.8-a (the formation is called an α -lattice in [26]). However, the convergence to crystalized formations depends on the amount of energy dissipation in the system. Therefore, random swarming motion may be generated even with the selection $x_0 \approx \rho_0$.

The spacing term can be used to control the density of the swarm by modulating the inter-agent distance. In addition, another important purpose of the spacing term is to avoid collisions between guardians. Therefore, the selection of ρ_0 (and x_0) may depend on the relative size of the vehicle with respect to the perceptual range ρ_s , i.e., a small value of ρ_0 may be sufficient to guarantee collision avoidance

if the vehicle size is small. Instead of introducing another parameter to describe the vehicle size, we make a conservative choice: $\rho_0 = \rho_s$.

The random force $\mathbf{F}_i^{(\text{rand})}$ has a constant magnitude $K_r \bar{u}_P$ in a random direction θ_i , i.e.,

$$\mathbf{F}_i^{(\text{rand})} = K_r \bar{u}_P [\cos \theta_i, \sin \theta_i]^T, \quad (5.17)$$

where $K_r \in [0, 1)$. The random variable θ_i is generated by the following process:

$$\dot{\theta}_i = W w_i, \quad (5.18)$$

where w_i denotes the unit-intensity white noise, and $W > 0$ is a parameter describing the intensity. The intensity W determines how much (on average) the force $\mathbf{F}_i^{(\text{rand})}$ changes its direction in each time step.

The main purposes of the random forcing $\mathbf{F}_i^{(\text{rand})}$ are (i) to make the trajectories of the guardians unpredictable to the intruders (unlike the orbiting motion studied in the previous section); and (ii) to propel the guardians to maintain sufficiently high speed during the swarming phase (recall the second objective of swarming stated in Section 5.3.1). For the latter purpose, we seek to use W that maximizes the mean speed of the guardians during the swarming phase. Figure 5.7 shows how the mean speed (average taken over agents and time) varies with W for different K_r . The mean velocities are obtained from numerical simulations performed with nominal parameters shown in Tab. 5.1 and 5.3. Figure 5.7 shows that for every choice of K_r , there exists an optimal W that maximizes the mean speed. The figure also shows

Table 5.3: List of parameters in the swarming algorithm and their nominal values.

Force		Description	Nominal Value
$\mathbf{F}^{(\text{cent})}$	k_c	Spring constant	1
	b_c	Damping constant	0.5
$\mathbf{F}^{(\text{spac})}$	ρ_0	Interaction range	ρ_s
	k_s	Spring constant	4
	x_0	Rest length	ρ_s
	b_s	Damping constant	0
$\mathbf{F}^{(\text{rand})}$	K_r	Magnitude	0.5
	W	Intensity of white noise	0.13

that the magnitude K_r positively affects the mean velocity of the guardians.

Treating W as a function of K_r , the random force only has a single parameter K_r . Figure 5.8 shows the snapshot of the swarm with different values of K_r . The edges indicate the link defined by the proximity-based interaction used in $\mathbf{F}_i^{(\text{spac})}$. A crystalized formation (α -lattice) forms for small values of K_r , whereas the links are broken and the swarm becomes more random for larger values of K_r . The trajectories extending from the particles indicate the velocities that they have, i.e., guardians have higher velocities for larger K_r . The figure also shows that there is a tradeoff between the two objectives of the swarm—high density and high speed. (Although it is possible to modulate the spring constant k_c to maintain a fixed swarm density while the speeds of the agents are increased with K_r , we allow the swarm density to decrease here in order to reduce the risk of collision.)

Finally, note that the magnitude of $\mathbf{F}_i^{(\text{swarm})}$ can exceed the limit \bar{u}_P , in which

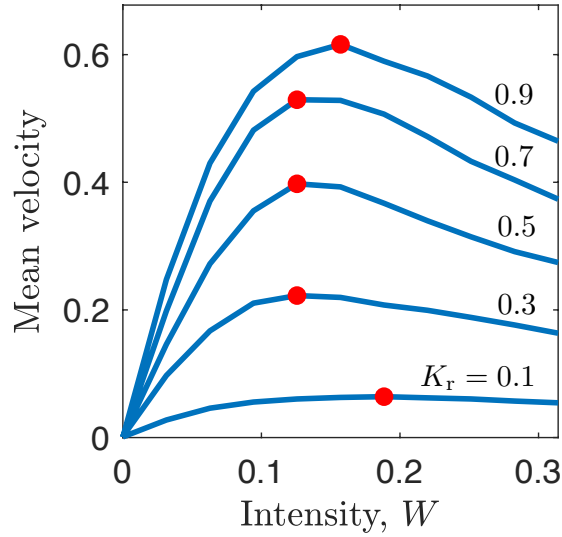


Figure 5.7: Mean velocity in the swarming phase as a function of the intensity of the white noise, W , that drives the direction of the random forcing. Different lines are generated from different magnitudes, K_r , of the random forcing. The red circles highlight the critical points.

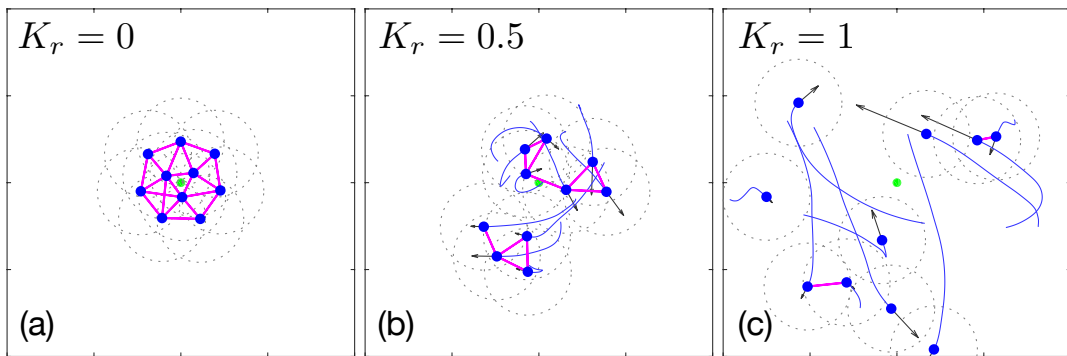


Figure 5.8: Snapshots of the swarm showing how the strength of random forcing, K_r , changes the swarm from crystallized formation to random oscillatory motion. The edges connect the agents within the range ρ_s .

case the control is saturated while preserving its direction, i.e.,

$$\mathbf{F}_i = \frac{\bar{u}_P \mathbf{F}_i^{(\text{swarm})}}{\|\mathbf{F}_i^{(\text{swarm})}\|}. \quad (5.19)$$

The next section studies how the random swarming motion affects the probability of target capture.

5.3.3 Optimal Randomness

We introduced various control parameters in Section 5.3.2 that are listed in Tab. 5.3. However, we are most interested in how the random oscillatory motion plays a role in the target capture scenario. Therefore, we choose K_r to be the independent parameter of the swarming motion, and study how the random forcing affects the probability of target capture.

Numerical simulations calculate the probability of target capture P_{cap} by counting the number of successful pursuits. In the simulation, the success of target capture (see Definition 5.1) is assessed using the energy function introduced in the proof of Proposition 5.2, i.e., the target is captured if the quantity $V_i = \frac{1}{2}\|\mathbf{r}_{T/i}\|^2 + \frac{1}{2c}\|\mathbf{v}_{T/i}\|^2$ becomes less than $\frac{1}{2}\rho_s^2$ at any point in time for any guardian i .

Figure 5.9 shows how P_{cap} varies as a function of K_r for different sets of parameters. The critical points are highlighted with circles. The left figure shows the effect of Γ , and the right figure shows the effect of N_P . The trend on the optimal K_r can be explained by the two objectives of the swarming: density and speed (see the discussion in Section 5.3.1). For a larger K_r , the guardians have

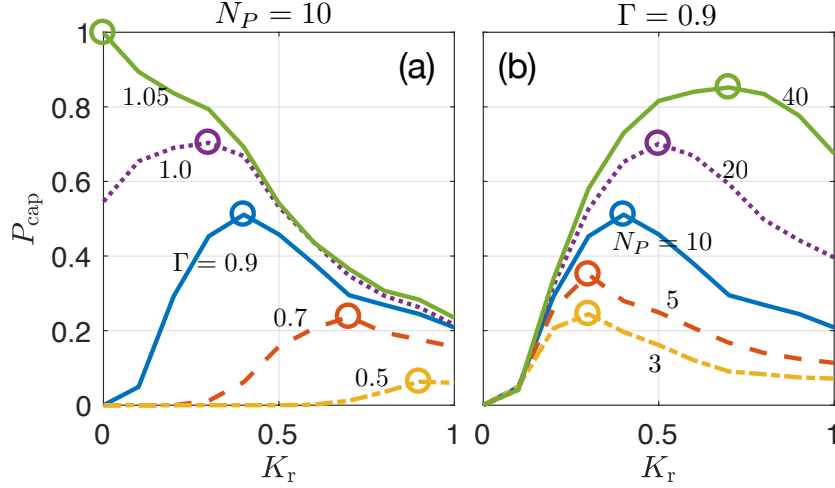


Figure 5.9: Probability of target capture as a function of K_r (the strength of random forcing). The nondimensionalized guardian acceleration Γ is varied in (a), whereas the number of pursuers N_P is varied in (b).

higher speed by sacrificing the density of the swarm, and vice versa. Therefore, the optimal K_r increases with increasing N_P , because a larger swarm inherently has a high probability of target encounter, P_{enctr} , and is able to sacrifice the density. On the other hand, the optimal K_r reduces with increasing Γ because guardians with higher Γ do not have to rely on their initial speed for successful pursuit (i.e., they inherently have high P_{align}), and therefore, increasing the density is more important than maintaining high velocity. The specific values of K_r that give optimal P_{cap} will vary if we tweak the other parameters in Tab. 5.3, however, the aforementioned trends are preserved.

5.3.4 Gain Modulation

This section discusses some of the strategies for the guardians to adapt to different situations by tuning their control gains in the swarming phase.

Recall that the expression of nondimensionalized guardian acceleration Γ in (5.2) involves target speed v_T . This implies that for intruders with different speeds, the value of Γ will be different for each of them even if the guardians' capabilities (\bar{u}_P , ρ_s and ρ_p) are fixed. The immediate application of simulation results in the previous section (Fig. 5.9-a) is to modify K_r according to the a priori knowledge about the speeds of incoming intruders. If the intruder is expected to be slow (i.e., $\Gamma > 1$), the guardians should wait with crystalized formation using $K_r = 0$. On the other hand, if the intruder is expected to be fast (i.e., $\Gamma \ll 1$), the guardians should increase their speed by using $K_r \approx 1$.

Consider another situation where the number of guardians change over time. For example, if the guardians leave the swarm as they successfully track the intruders, the number of guardians that remain in the swarm decreases over time. If more guardian vehicles are deployed to join the swarm, the number N_P may increase over time. In either case, the guardians should modulate the gain K_r according to the result in Fig. 5.9-b; i.e., increase (resp. decrease) K_r when N_P increases (resp. decreases). (Estimation of N_P without a centralized control system is an interesting problem, but it is out of the scope of this work.)

Finally, consider another situation where the guardians have some a priori knowledge about the azimuthal direction of the intrusion ψ_j^{int} ; e.g., the probability density function of ψ_j^{int} . The guardians can increase P_{cap} by modifying the central

force $\mathbf{F}_i^{(\text{cent})}$ as follows. Let R denote a rotation matrix

$$R(\hat{\psi}) = \begin{bmatrix} \cos \hat{\psi} & \sin \hat{\psi} \\ -\sin \hat{\psi} & \cos \hat{\psi} \end{bmatrix}, \quad (5.20)$$

and Λ denote a diagonal matrix

$$\Lambda(\sigma) = \begin{bmatrix} 1/\sigma & 0 \\ 0 & \sigma \end{bmatrix}, \quad (5.21)$$

where additional parameter $\hat{\psi}$ describes the expected direction of intrusion, and $\sigma > 1$ describes the confidence in that direction. The swarm is elongated in the $\hat{\psi}$ direction by the following modification:

$$\mathbf{F}_i^{(\text{cent})} = R(\hat{\psi})^T \Lambda(\sigma) R(\hat{\psi}) (-k_c \mathbf{r}_i - b_c \mathbf{v}_i), \quad (5.22)$$

Figure 5.10 shows the snapshots from simulation. The elongated swarm increases both P_{enctr} and P_{align} if $\hat{\psi}$ is sufficiently close to the actual ψ^{int} .

We introduced ways in which guardians can utilize a priori knowledge about the intruders to maximize the probability of target capture. The next section introduces a simple communication between the guardians to enable cooperation, and show how it significantly improves the probability of target capture.

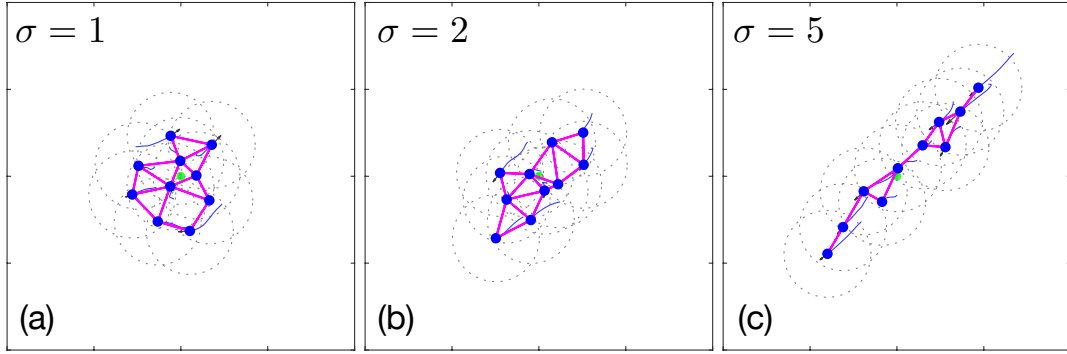


Figure 5.10: Snapshots of the swarm showing how the elongation of the swarm is controlled by the parameter σ . The expected direction of intrusion is $\hat{\psi} = \pi/4$, and the randomness is chosen to be $K_r = 0.3$.

5.3.5 Velocity-Alignment Strategy

The swarming algorithms introduced in Section 5.3.1 and 5.3.2 focused on the individual motion of the guardians. This section adds cooperation among the guardians to further improve the target-capture capability. In particular, we consider a collaboration that is generated from a velocity-alignment behavior.

The employment of velocity-alignment behavior is inspired by swarms of male mosquitoes. Chapter 2 analyzed the flight data of wild mosquitoes and observed their intermittent velocity-alignment behavior. Although the reason for the velocity-alignment behavior is unknown, one hypothesis is that the male mosquitoes may be transmitting information about the presence of a female mosquito in the swarm.

Since male mosquitoes are competing against each other to mate with the female, the male that sees a female will not broadcast that information to other males. Instead, it is the other males that try to sense male behavior changes to recognize the presence of a female. On the other hand, the guardian vehicles are cooperating with each other, so it is reasonable for them to actively communicate

to share the information about the presence of the intruder.

Consider a one-digit binary signal (i.e., communication of “Yes” or “No,” instead of a serial communication like “010010...”) that each vehicle can broadcast to other vehicles within the range ρ_s . The signal from vehicle i tells other vehicles whether it is in a *regular* swarming state or in an *alerted* state, which is the union of pursuit phase and velocity-alignment phase. In practice, the signal can be based on vision or acoustic sensing received by cameras or microphones, for example. Although there exist more sophisticated communication schemes that may carry richer information—like target position and/or velocity—we show how this one-digit binary signal can be used to significantly improve performance.

The algorithm for the velocity-alignment behavior is as follows. Let $S^{(\text{alert})}$ be the set of guardians that are either in pursuit phase or velocity-alignment phase. A guardian i in the swarming phase switches to velocity-alignment phase if it sees any guardian in the set $S^{(\text{alert})}$, i.e., if the following set is nonempty:

$$S_i^{(\text{align})} = \{ j \mid \|\mathbf{r}_{i/j}\| \leq \rho_s, j \in S^{(\text{alert})} \}. \quad (5.23)$$

The velocity-alignment phase will terminate in one of the following two ways: (i) guardian i switches back to the swarming phase when $S_i^{(\text{align})} = \emptyset$; or (ii) it switches to the pursuit phase when it encounters the target, i.e., $\|\mathbf{r}_{T/i}\| < \rho_p$.

Additional forcing for guardian i in the velocity-alignment phase is

$$\mathbf{F}_i^{(\text{align})} = b_a \sum_{j \in S_i^{(\text{align})}} \mathbf{v}_{j/i}, \quad (5.24)$$

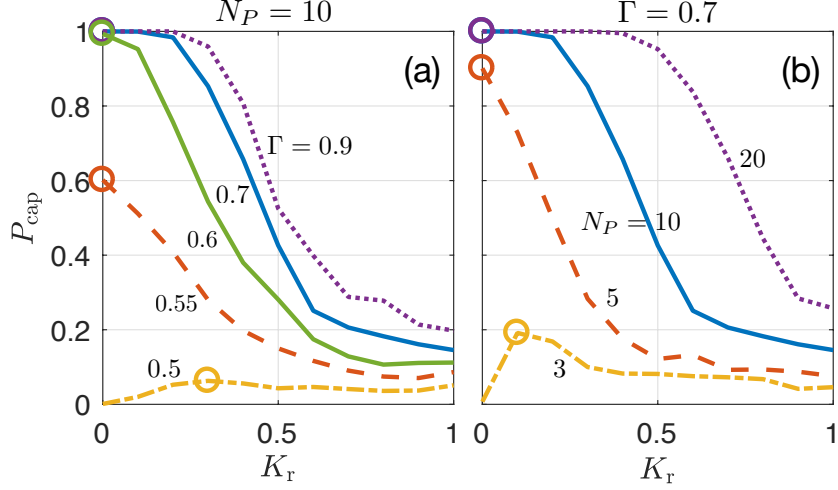


Figure 5.11: Probability of target capture with velocity-alignment behavior. (Note that $\Gamma = 0.7$ instead of 0.9 is used in (b).)

which is equivalent to changing the damping constant b_s in the spacing term $\mathbf{F}^{(\text{spac})}$ to b_a , only for those guardians in the set $S_i^{(\text{align})}$. The constant $b_a (> b_s)$ is sufficiently large that it dominates the other control terms during the the velocity-alignment phase.

If the guardian in pursuit phase aligns its velocity to the target, and if the velocity-alignment interaction propagates through the swarm, guardians that are far from the target can start moving in the direction that matches the velocity of the target. This mechanism allows the guardians to effectively increase their perceptual range ρ_p to the size of the swarm in order to gain favorable initial conditions for pursuit.

Figure 5.11 shows P_{cap} with varying K_r . For fixed $N_P = 10$, the target is always captured (i.e., $P_{cap} = 1.0$) for Γ greater than 0.7. Similarly for fixed $\Gamma = 0.7$, target capture is guaranteed for $N_P > 10$. This improvement is significant compared to the results from the random-swarmer case in Fig. 5.9. (Note that $\Gamma = 0.9$ was used

for Fig. 5.9-b.) The figure also shows that $P_{cap} = 1.0$ is achieved with a crystalized formation ($K_r = 0$), because high connectivity is necessary for the guardians to propagate the velocity-alignment interaction.

Note, guardians perceive only the velocities of nearby agents, and this information is not transmitted through communication. Therefore, for the velocity-alignment strategy to work properly in the target-capture scenario, it is necessary that the guardians in the spanning tree of the interaction graph quickly adjust their velocities in the correct direction (i.e., the direction of target’s motion). Otherwise, the error in the direction may propagate through the interaction network, and guardians far from the target may end up accelerating in the wrong direction. (The issue of velocity-alignment in erroneous directions occurs in the experiments due to the slow response of the guardians caused by latency in the closed-loop system. Section 5.4.5 addresses this issue and augment the velocity-alignment behavior by adding a directionality constraint to their interaction.)

5.4 Experimental Results

This section experimentally validates the results in Section 5.2 and 5.3 using a quadrotor swarm. Additional challenges that arise in the experimental implementation are discussed, and algorithms are augmented to overcome those challenges.

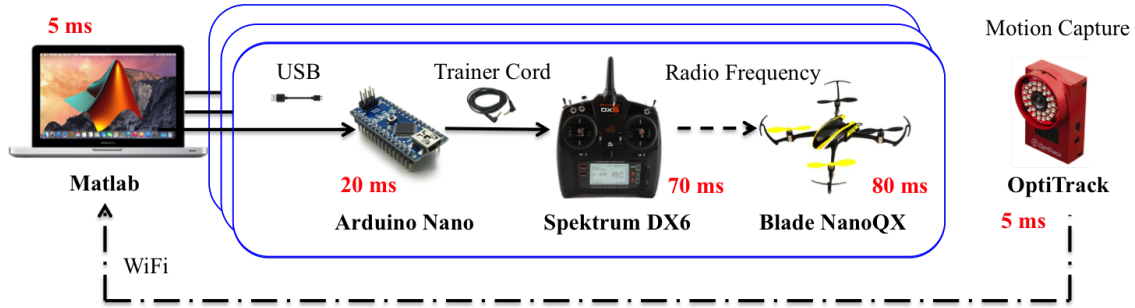


Figure 5.12: The architecture of the experimental setup. The red numbers indicate the approximate time delay from each component. The blue box is duplicated according to the number of vehicles.

5.4.1 Experimental Testbed

We conducted experiments using a group of small quadrotors in an indoor motion-capture environment. We used six BLADE Nano QX, a commercially available quadrotor. The architecture of the experiments is summarized in Fig. 5.12. The commands are computed on a desktop computer and sent to an Arduino Nano via USB serial communication. The Arduino Nano converts the received serial signal into a PPM (Pulse Position Modulation) command and sends it to the trainer port of a Spektrum DX6 transmitter which sends RF (Radio Frequency) commands to the vehicle. The OptiTrack motion-capture system tracks the position and attitude of the vehicle and streams them to the computer. When it is sent out from the computer, the control law proposed in Section 5.3 is converted to a desired stick input (see [96] for details).

One additional challenge in our experimental setup is the time delay caused by the vehicle dynamics and the communication between Matlab and the Nano QX. It takes approximately 170 ms for the commands from the computer to affect the

vehicle acceleration. Another limitation is the size of the test area. The horizontal footprint of the vehicle is 18.2×18.2 cm, whereas the horizontal area of the volume tracked by the motion-capture system is approximately 3×3 m.

5.4.2 Disturbance Observer

Achieving the desired position or velocity can be accomplished by various techniques including PID or LQR control. However, our control law in Section 5.3.2 is given in terms of the desired acceleration, and achieving a specified acceleration is a nontrivial problem. First, we do not have access to the IMU (Inertial Measurement Unit) data on the vehicle, and also the position data from motion capture system is too noisy to estimate the acceleration. Second, because of the reflective markers mounted on the vehicle, there is an offset in the position of the center of mass, and trimming cannot completely eliminate the effect of this offset. Third, even if each vehicle is trimmed very accurately, the battery usage significantly affects the conversion from stick input to the achieved acceleration.

This work elects to use an adaptive disturbance observer to estimate the discrepancy between the desired and achieved acceleration. (A more general version of this observer was introduced in [97] for the application to friction compensation in mechanical systems.) Let $\mathbf{d} \triangleq \mathbf{a}'_{\text{actual}} - \mathbf{u}_{\text{des}}$ be the disturbance, i.e., the difference between the actual and desired acceleration of the vehicle. The goal is to estimate \mathbf{d} and augment the control input as

$$\mathbf{u}'_{\text{des}} = \mathbf{u}_{\text{des}} - \hat{\mathbf{d}}, \quad (5.25)$$

where $\hat{\mathbf{d}}$ denotes the estimated disturbance. The actual acceleration then becomes $\mathbf{a}_{\text{actual}} = \mathbf{u}_{\text{des}} + \mathbf{d} - \hat{\mathbf{d}}$. For the case where \mathbf{d} is constant the following observer drives the estimation error $\mathbf{e} = \mathbf{d} - \hat{\mathbf{d}}$ to zero:

$$\hat{\mathbf{d}} = \mathbf{z} + k_O \mathbf{v}, \quad (5.26)$$

$$\dot{\mathbf{z}} = -k_O(\mathbf{u}_{\text{des}} + \hat{\mathbf{d}}), \quad (5.27)$$

where $k_O > 0$ denotes the observer gain and \mathbf{z} denotes the observer states. (To see the convergence to zero, use the Lyapunov function $V = \frac{1}{2}\|\mathbf{e}\|^2$.) Although the disturbance due to battery usage is time varying, it is sufficiently slow compared to the vehicle dynamics that we treat it as a constant.

5.4.3 Effect of Time Delay

The nondimensionalized guardian acceleration Γ quantifies the difficulty of target capture problem. Since we have time delay in the experimental testbed, the guardian can only respond to the intruder $\tau = 0.17$ (s) after the close encounter. Modifying the proof of Proposition 5.1, we define the augmented version of the pursuer acceleration Γ' as follows.

The time it takes from the close encounter to the time that the guardian reaches the speed v_T is now $t'_f = v_T/\bar{u}_P + \tau$. The intruder has to travel the distance $\rho_s + \rho_p + \frac{1}{2}\bar{u}_P t_f^2$ in order to escape. The condition for escape is now $v_T t'_f > \rho_s + \rho_p + \frac{1}{2}\bar{u}_P t_f^2$, and this condition gives rise to the following time-delayed guardian

acceleration:

$$\Gamma' \triangleq \Gamma - \frac{2\bar{u}_P\tau}{v_T}. \quad (5.28)$$

The effective advantage on the guardian’s side reduces proportionally to the time delay τ . Extending the theoretical analysis in Section 5.2.1, we expect that a static guardian with $\Gamma' < 1$ will never capture the target in the experiment.

We confirmed this extension with experiments using a virtual target simulated in Matlab. The maximum acceleration of the vehicle is approximately $\bar{u}_P = 6.0$ (m/s²). By varying v_T , we tested pursuit with different values of Γ . For a static guardian with $\alpha = 0.67$, where $\rho_s = 0.6$ (m) and $\rho_p = 0.4$ (m), we simulated the easiest-case scenario considered in the proof of Proposition 5.1, i.e., the case where the intruder’s trajectory passes through the guardian’s position. Although the original theory predicts that $\Gamma > 1$ will enable target capture for this easiest case, the experiment required $\Gamma > 1.78$ (or equivalently $v_T < 2.6$ (m/s)) due to the latency in the system. However, using the definition (5.28) with the time delay in our system $\tau = 0.17$ (s), we obtain $\Gamma' = 0.99$ which is close to 1, as expected.

5.4.4 Optimal Randomness

We conducted experiments of the swarming and pursuit scenario with six guardians to validate the simulation results in Section 5.3.3. Based on the analysis in the previous section, we use Γ' as the index to describe the difficulty of the pursuit problem. Specifically, we chose $\rho_s = 1.0$ (m), $\rho_p = 0.5$ (m), $\bar{u}_P = 2.0$ (m/s²), and $v_T = 2.23$ (m/s), which corresponds to $\Gamma' = 0.9$.

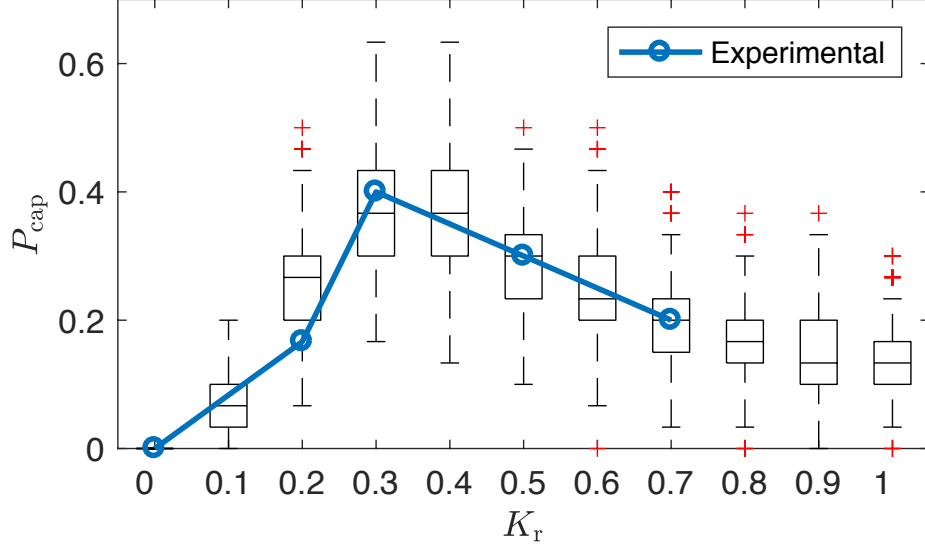


Figure 5.13: Probability of target capture as a function of the strength of random forcing. For each K_r , experimental results are calculated from 30 trials. The animation is available at [<https://youtu.be/Cnz75WZ88rI>]. Γ greater than 0.7 are not tested due to the constraint in the motion-capture area. The box plot is obtained from computer simulation; i.e., 200 sets of 30 trials are used to see the variance that we expect from 30 experimental runs.

The swarming algorithm in Section 5.3.2 is extensible to three dimensions, except for the random forcing term. Since we only consider the case where the target speed has zero vertical component, pursuit behavior is considered in the horizontal direction only. Although we give guardians the reference altitudes with 0.15 (m) interval, the spacing term $\mathbf{F}^{(\text{spac})}$ is important to ensure collision avoidance and to avoid the downwash from the vehicles above.

The perceptual ranges ρ_s and ρ_p , as well as the intruder, are represented virtually in Matlab. The pursuit is defined to be successful if the following two conditions are satisfied: (i) a guardian is in pursuit phase when the target reaches the boundary of the motion-capture arena; and (ii) at that time, the energy function satisfies $V \triangleq \frac{1}{2}\|\mathbf{r}_{T/P}\|^2 + \frac{1}{2c}\|\mathbf{v}_{T/P}\|^2 < \frac{1}{2}\rho_s^2$, as was considered in the simulation study.

We ran 30 experiments for each of 4 values of K_r and obtained the probability of target capture. Due to the limitation in the motion-capture area, the values of Γ greater than 0.7 could not be tested (recall that the size of the swarm increases with K_r). Figure 5.13 shows the comparison of the experimental data with the simulation results. The 6000 trials from the simulation results are partitioned into 200 sets of 30 trials to compute the variance in P_{cap} we expect from the experiments (see the box plot in Fig. 5.13). For the values of K_r that are tested, the experimental results show the same trend as the simulation results; i.e., the experimental results support the existence of the optimal random forcing at around $K_r = 0.3$ for this set of Γ , α and N_P . The agreement between simulation and experimental results also supports the validity of the augmented parameter Γ' .

5.4.5 Velocity-Alignment Strategy

We tested the velocity-alignment behavior with a swarm of six guardians. Following the simulation results in Section 5.3.5, we only study the case with $K_r = 0$, which gives the optimal performance. The sensing and communication, as well as the intruder motion are represented virtually in Matlab.

A major challenge in the experimental setting is highlighted in Fig. 5.14. In the simulation, all guardians instantaneously respond to the target through velocity-alignment behavior, and their acceleration (see the forcing vector in Fig. 5.14-a) point in the same direction that matches the target velocity. However, in the experiment forcing vectors point in various directions (see Fig. 5.14-b).

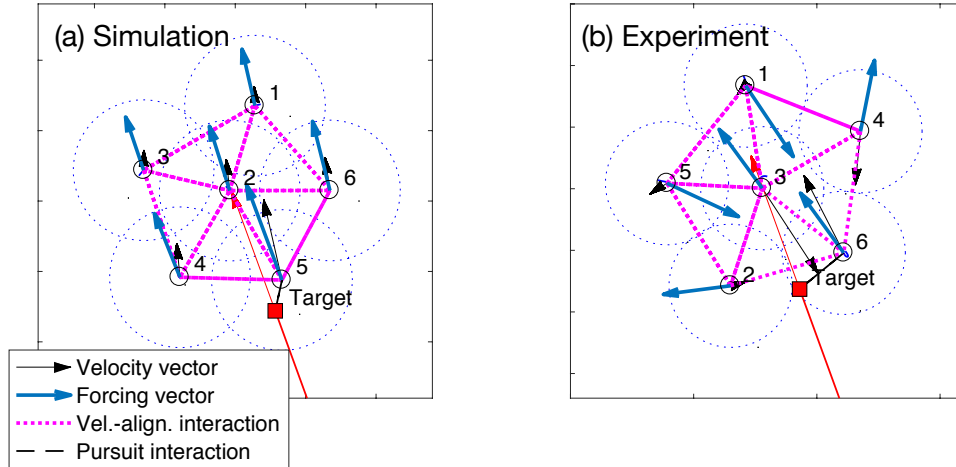


Figure 5.14: Comparison of the velocity-alignment forcing in simulation and experiment. All guardians quickly respond in the desirable direction in the simulation, whereas the guardians have forcing in various directions in the experiment. Note that the velocity vectors for guardians are scaled six times larger than the intruder for clarity.

The velocity-alignment forcing in erroneous directions are caused by the delay in individual velocity-matching interaction. In simulation, guardians 2, 4 and 6 are already aligned with guardian 5. However, in the experiment, guardians 2, 3 and 4 are not yet aligned with guardian 6. As a result, guardian 1 is accelerating towards the right bottom at this moment, since it is matching its velocity to guardians 3, 4 and 5 who have their velocities in the wrong directions. The velocity-matching in the experiment is slower than the simulation because (i) the latency in the closed-loop system delays the response to alerted neighbors; and (ii) the latency also generates velocity oscillation during crystalized formation, which may give unfavorable initial conditions, e.g., see guardian 3 in Fig. 5.14-b.

To reduce the velocity-alignment in erroneous directions, we augment the algorithm by introducing directionality in the communication. The directionality is added to both the transmitter side and the receiver side. First, a guardian i in the

alerted state now sends signal to j only if

$$\hat{\mathbf{v}}_i \cdot \hat{\mathbf{r}}_{j/i} < \cos \phi_1, \quad (5.29)$$

where $\hat{\mathbf{v}}$ denotes a unit vector, i.e., $\hat{\mathbf{v}} = \mathbf{v}/\|\mathbf{v}\|$. Second, a guardian j receives signal from an alerted guardian i only if

$$\hat{\mathbf{v}}_i \cdot \hat{\mathbf{v}}_j < \cos \phi_2. \quad (5.30)$$

These two constraints help the guardians to propagate the signal in the desirable direction. Small values for ϕ_1 and ϕ_2 increase the accuracy of the velocity information carried through the interaction, but will also reduce the connectivity. Since securing sufficient connectivity is important for a small swarm, we choose $\phi_1 = 150^\circ$ and $\phi_2 = 90^\circ$ for the experimental results presented next.

Figure 5.15 shows the snapshots from a single experimental trial. System parameters were chosen so that $\Gamma' = 0.90$ and $\alpha = 0.5$. Due to the velocity-alignment behavior, guardian 2 on the far side starts accelerating in the direction of target's motion even though it does not perceive the target itself (see the forcing \mathbf{F}_2 in Fig. 5.15-a). This behavior generates a favorable initial condition at the time of close encounter (see \mathbf{v}_2 and \mathbf{v}_T in Fig. 5.15-b). This initial condition enables guardian 2 to successfully capture the target (Fig. 5.15-c). As was done in the simulation and in the random-swarmer case, we define target capture by looking at the the energy function introduced in the proof of Proposition 5.2. It has a

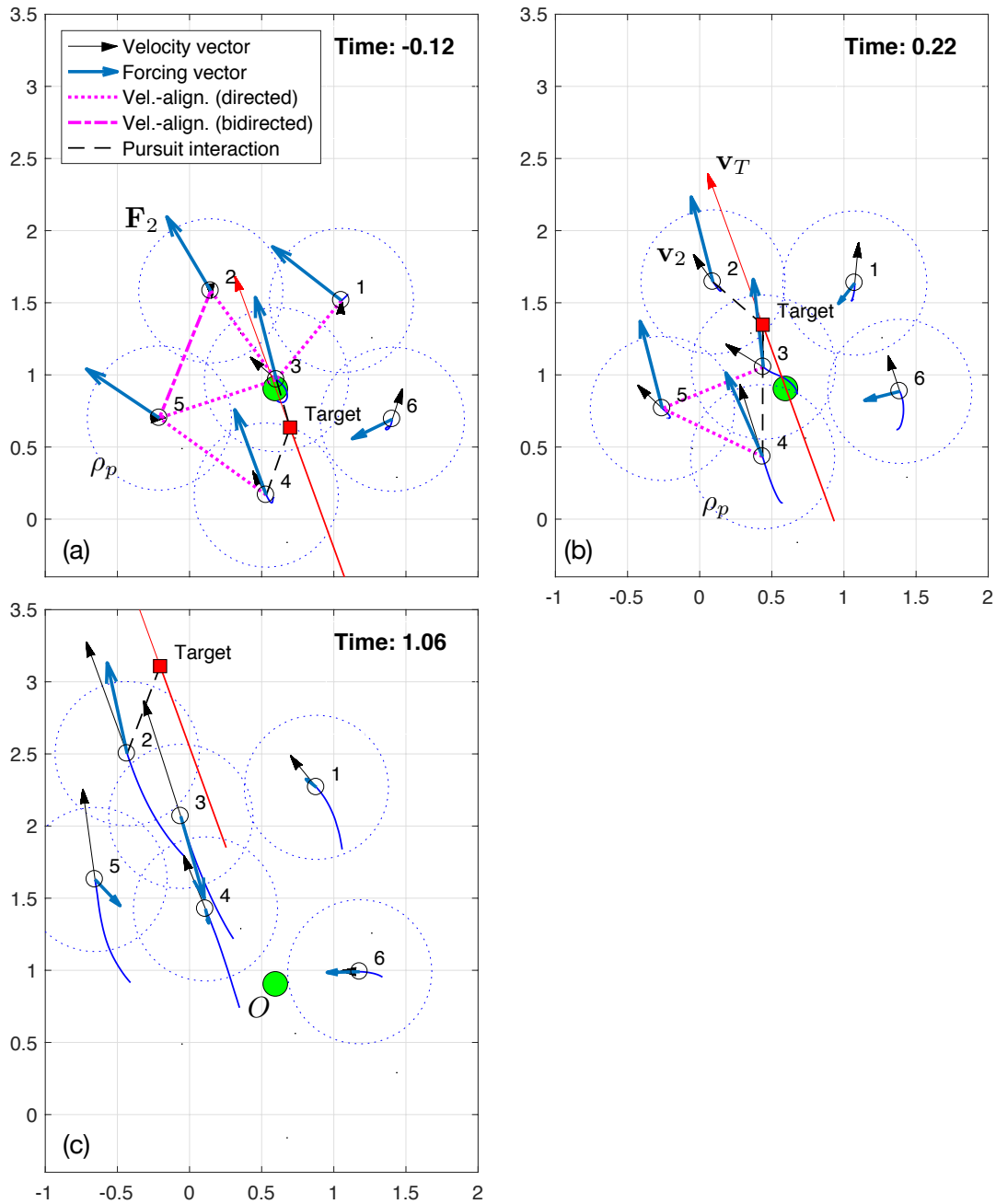


Figure 5.15: Snapshots of pursuit scenario with velocity-alignment strategy. The animation is available at [<https://youtu.be/Cnz75WZ88rI>]. An intruder approaches from right bottom of the figure. (a) Guardian 3 and 4 are in pursuit phase, and there is a network of velocity alignment interaction also involving guardians 1, 2 and 5. As a result, guardian 2 is already accelerating towards the top left corner (see the forcing \mathbf{F}_2), which matches with the direction of target velocity. (b) At the time guardian 2 encounters the target, its velocity \mathbf{v}_2 is well aligned with the target velocity \mathbf{v}_T . Note that guardian 4 is still in pursuit phase since the target is still within the range ρ_s (but not ρ_p). (c) Guardian 2 successfully tracks the target, while other guardians are returning to O (i.e., their accelerations are pointing towards O).

value $V = 0.26$ for guardian 2, which is less than the criterion $\frac{1}{2}\rho_s^2 = 0.50$, i.e., the Lyapunov analysis in Proposition 5.2 predicts that the target will stay within the range ρ_s of guardian 2 indefinitely.

The target was captured 15 times out of 18 trials, which gives the success rate of $P_{cap} = 0.83$. This probability is lower compared to the simulation result ($P_{cap} = 1.0$), mainly due to the velocity-alignment in the wrong directions caused by the latency in the system (see earlier discussion). Nonetheless, the success rate is improved as compared to the case without velocity-alignment interaction, which validates the advantage of utilizing the communication of binary information.

Chapter 6

Conclusion

6.1 Summary

This dissertation analyzes the collective behaviors in mosquito mating swarms and considers their application to pursuit problems with autonomous rotorcraft. The tools from engineering help the analysis and modeling of the biological data (i.e., the flight kinematics of mosquito), and in turn, inspirations from mosquito behavior help formulating and solving engineering problems (i.e., pursuit with small and agile rotorcraft).

For the analysis of swarming behavior, we develop a correlation function that quantifies the degree of velocity alignment for a given pair of mosquitoes. We propose a procedure to define a threshold on the correlation value to classify whether a given pair of males are interacting or not. The time-varying interaction graphs show that the mosquitoes form subgroups in the swarm whose size and membership change rapidly. The results indicate that the mosquitoes interact with each other instead of flying around independently around the swarm marker, which is how

insect aggregation was previously modeled. We augment the existing particle model by including a local interaction represented by damping of relative velocity between males. The augmented model shows good agreement with the correlation data from real swarms.

For the analysis of the pursuit behavior, we consider two phases: the flight before and after the close encounter. Our interests in the flight before close encounter are the directionality of pursuit (i.e., who is closing the distance) and the strategy used to close the distance. Using the metric for classical pursuit we show that the pursuit may occur in both directions. We also show an evidence supporting the hypothesis that mosquitoes use motion-camouflage pursuit.

The flight after the close encounter, which we call the coupling phase, is modeled using delay differential equations. We interpret the model parameters as the control gains that the mosquitoes may be modulating, and analyze the stability of the delayed system. Inspired by the gain modulation observed in the data, we design a particle model that replicates three behaviors: swarming, velocity alignment and pursuit. The Lyapunov stability analysis of this model showed that males' velocity-matching behavior may help them generate good initial conditions to start pursuing the female.

Inspirations from mosquito behavior are applied to pursuit problems. The first pursuit problem corresponds to the phase after the close encounter, in which the pursuer has already perceived the target. The main focus is to address the discrepancy between the pursuit law necessary for small and agile agents and laws that were developed for the application to missile guidance and navigation. We propose

a bio-inspired pursuit law based on the agent dynamics and design criteria that are suitable for rotorcraft MAVs. We show that the pursuit law is robust to unknown target maneuvers, state measurement errors (sensor noise), and control saturation. We perform analytical, numerical, and experimental comparison of various pursuit laws and show that the proposed law has the least energy consumption—while staying closest to the target in a near-miss scenario—among all those considered, including a sliding-mode controller and a partial-stability-based controller.

The second pursuit problem considers a swarming strategy for multiple guardians to defend a protected zone from an intruder. The scenario is inspired by aggregation of male mosquitoes preparing for the encounter with a female. We are interested in how swarming motion in autonomous vehicles helps the success of target capture. We show that a static guardian requires high capability to guarantee target capture, whereas swarming motion relaxes the requirement. Guardians maximize the probability of target capture by balancing the swarm density and their speed. Inspired by the swarming behavior of male mosquitoes, a random swarming motion is studied, and ways in which control parameters may be optimized are discussed. In addition, velocity-alignment strategy is considered for the case where guardians communicate with each other. Even with a communication of only one digit of binary information, the probability of target capture is significantly increased when used with the velocity-alignment strategy, both in simulation and in experiment.

6.2 Ongoing Work and Proposed Work

This dissertation makes contribution in two directions: analysis of mosquito behavior, and control design for autonomous rotorcraft. However, there is still much work to be done to fully understand the collective behaviors in mosquito swarms, and there are also various directions to extend the pursuit problems considered in this dissertation. Section 6.2.1 discusses one of the key aspects in mosquito behavior that needs to be studied—the difference between successful and unsuccessful males—and some approaches that may be taken. The planar pursuit problem studied in Chapter 4 is an intermediate step towards pursuit with flying vehicles. Section 6.2.2 discusses how the work may be extended to pursuit in three dimensions. The guardian-intruder problem introduced in Chapter 5 is just the beginning of a new research involving competing swarms of autonomous vehicles. Section 6.2.3 presents some ongoing work to formulate the problem with game-theoretic approach, and discusses how the multi-intruder scenario will make the game more interesting and also challenging.

6.2.1 Mosquito Mate Selection

One of the broader impacts of mosquito data analysis is its application to release-based program of malaria vector control such as Sterile Insect Technique [76]. To contribute to such an application, it is important to know the characteristics of the males that are successful in mating with females.

Previous works have hypothesized that the female is captured by one of the

males in the swarm [98]. However, the hypothesis of female choice in *An. gambiae* is reasonable given the large difference in potential reproductive rates between males and females [99], and that the females in this species mate once for life (Nicholas C. Manoukis, personal communication, July 20, 2015).

To test the hypothesis of female choice, additional data collection and analyses must be performed. First, the flight data used in this dissertation is limited by its frame rate, which is 25 Hz. This time resolution is insufficient to detect the lag information in the male-female interaction, i.e., whether the male is matching its velocity to the female or the other way around. With the video sequences with higher frame rates, we may be able to take a closer look at what is happening before and after the close encounter.

To characterize the behavior of males who successfully mate with the female, it will be useful to compare them against flight data of unsuccessful pursuit. We observed only a few of such unsuccessful flights in the current data set. Increasing the number of data sets that include the formation of couple will help us draw statistically justified conclusions. If we still observe significantly less occurrences of unsuccessful pursuit, that would imply that the close encounter is not only necessary but also sufficient to form a couple. It would also indicate that female choice (if any) is already made at the time of close encounter.

Combining sensory data with kinematic data will add another dimension to the data analysis. It is known that acoustic interaction plays an important role in mosquito mating [67, 100, 101]. Males detect a female by her specific flight tone, and coupling male and female synchronize their wing-beat frequencies. If the flight

tones in the free flight can be measured, we may be able to find the relation between wing-beat frequency and the flight speed of the mosquito. This relation may shed light on the mechanism and the meaning of velocity-alignment behavior.

6.2.2 Rotorcraft Pursuit in Three Dimensions

Pursuit algorithms have been considered for agents that move in three-dimensional space. For missile guidance and navigation, the LOS stabilization in three-dimensions using proportional navigation is considered in [35, 102, 103]. The motion-camouflage pursuit was extended to three dimension in [104]. For the pursuit algorithm designed in Chapter 4, the polar coordinates may be modified to spherical coordinates for the extension to three dimension. (Similar approach can be found in [105]) However, to avoid singularities in this extension, some other formulation that uses quaternions or $SE(3)$ matrix group to describe the relative motion of the target with respect to the pursuer may be appropriate.

With the dynamics in three dimensions, an important direction for future research is to consider a more realistic problem for counter UAS applications, i.e., capture a multirotor helicopter using another multirotor helicopter. This scenario is similar to air-combat, which was studied extensively for the application to fixed-wing aircraft [106–108]. In air-combat, various maneuvering strategies were proposed to achieve the desired condition for the pursuer (attacker), which is to stay behind the target.

For air-combat with small and agile rotorcraft, the problem needs to be for-

mulated with different assumptions. First, the dynamics (maneuvering capabilities) of rotorcraft are different from fixed-wing aircraft. Also, the sensing capability of unmanned rotorcraft MAVs will be different from the visibility that human pilot has in the cockpit of an aircraft. Moreover, the desired condition for the pursuer (attacker) depends on the tools that it uses to capture the target. For example, if the pursuer shoots a net to capture the target, it may be easier to aim from above or in front of the target, rather than behind or below the target. The necessity to avoid the downwash may also require specific paths when approaching the target from below. These additional constraints may lead to pursuit and evasion strategies that are specific to rotorcraft MAVs.

6.2.3 Competition between Two Swarms

The guardian-intruder problem studied in Chapter 5 has a potential for various extensions. A direct extension is the scenario with multiple intruders. The problem now becomes a competition between two swarms of autonomous vehicles: intruders and guardians. A closely related problem is the *multiplayer reach-avoid game*, which deals with a scenario where one group seeks to reach an area quickly while the other group tries to delay or prevent it [109–111].

One example of a reach-avoid game is the so-called *Capture-the-Flag* [112]. In this game, each team owns a flag, and their goal is to capture the opponent's flag and safely return. This game has a pursuit-evasion aspect, since an agent can be intercepted by its opponent in the opponent's territory. However, the capture-the-

flag problem is very complex because it also involves an attacking-defending aspect and, possibly, switching of the agent roles, as well as the assignment problem to decide which agent should pursue which opponent agent. Some works have tackled this complex problem by combining the tools from differential games and graph theory [109, 112], whereas some other works made simplifying assumptions on the attackers' dynamics and used optimization techniques [110, 111].

Ongoing Work

Our preliminary work [95] formulates the intruder-guardian problem from a game-theoretic perspective to accommodate intruders' strategies, and also to distinguish between the capture that occurs before and after the intrusion. Let the intruder-guardian competition be a zero-sum game by considering the payoff function J_I and $J_G = -J_I$ associated to the team of intruders and guardians respectively. The payoff for the intruder team is the sum of the individual payoff for each intruder, i.e.,

$$J_I = \sum_i^{N_T} J_i, \quad (6.1)$$

where J_i is the payoff function associate to i th intruder. (Note that the payoff for individual guardian is not defined, because the performance is considered in terms of the entire guardian swarm.)

The value of J_i is determined as described in the payoff matrix in Fig. 6.1. Successful intrusion, corresponding to the first row of the matrix, is the case where intruder i reaches O without being captured by any of the guardians. (Note, this

		Guardian swarm	
		No capture	Capture
Intruder	Intrusion	$V_{int}(t)$	$V_{int}(t) - \eta$
	No intrusion	0	$-\eta$

Figure 6.1: Value of individual intruder payoff J_i depending on the performance of i th intruder and the guardian swarm.

definition is independent from the capture that might occur *after* the intrusion.)

Once the intruder successfully reaches O , it scores $V_{int}(t)$, which is a decreasing function of time defined as follows:

$$V_{int}(t) = e^{-(t-t_0)/\tau}, \quad (6.2)$$

where t_0 is the start time of the game and τ is the *intruder-payoff time constant*. If the intruder i misses O , or if it is captured by any of the guardians before reaching O , it does not score $V_{int}(t)$, corresponding to the second row of the matrix.

The parameter $\tau > 0$ models the risk of waiting incurred by the intruder's team. Consider, for example, the Capture-the-Flag problem [112] where two teams (A and B) divide their members into offensive and defensive players. The problem studied here can be considered as the competition between team A 's offensive players (intruders) and team B 's defensive players (guardians). In this case, there is another identical game played simultaneously where team A is guarding their flag against team B 's offensive players. The decaying payoff $V_{int}(t)$ with the time constant τ quantifies the risk that A 's flag is attacked by B within the duration of time $t - t_0$.

The use of an exponential function in (6.2) is inspired by the Poisson distribution [63], which is often used to model the probability of an event occurring in a fixed interval of time (e.g., earthquake, customer entering a store). In our problem, we are modeling the attack from B 's offensive players as a Poisson process, i.e., the probability that A 's flag is *not* attacked by B decays exponentially. Furthermore, with this Poisson-process assumption, the time constant τ corresponds to the expected time interval between successive attacks from B . Therefore, higher risk on team A (intruder's side) can be modeled by a smaller value of τ , i.e., faster decay in $V_{int}(t)$. Note, if the game is one sided and A does not have to defend their flag, then the constant can be set to $\tau = \infty$ so that $V_{int}(t) \equiv 1$.

Next, consider the performance of the guardian swarm. If any of the guardian captures the intruder i , then the guardian swarm scores $\eta > 0$ (equivalently, i th intruder scores $-\eta$), which corresponds to the second column in Fig. 6.1. Note that capture may be before or after the intrusion. The parameter η describes the penalty on the intruder swarm to lose its vehicles. Depending on the value of η , the scenario can be categorized into the following three cases:

$\eta = 0$: Pure guarding scenario. Guardians cannot win the game, but they lose unless they capture every intruder before intrusion.

$0 < \eta < 1$: The payoff $J_i = V_{int}(t) - \eta$, which corresponds to capture after intrusion, changes its sign from positive to negative during the game.

$\eta > 1$: The payoff $J_i = V_{int}(t) - \eta$ is already negative at the beginning of the game. There is no benefit for intruders to approach O unless they can

escape without capture.

Various intrusion-capture scenario can be modeled by the proper choices of parameters η and τ . As one example, consider a scenario where guardian vehicles are protecting an area against bombers or missiles. What happens after the intrusion is not so important (guardians have to capture the intruders *before* they attack the area), so we use $\eta \ll 1$ for this case. Another example is the scenario where intruders are manned aircraft for a reconnaissance mission. The penalty for losing a vehicle will be particularly high if it is manned, so we use $\eta > 1$ for this case. Consequently, intruders will only attempt to approach if probability of capture is sufficiently low. The other parameter τ can be chosen to model how sensitive the intruder's mission is to time.

Based on this payoff function, theoretical prediction on the outcome of the game as well as the effect of intrusion frequency (i.e., $\{T_j^{\text{int}}\}$ defined in Section 5.1.2) are presented in [95]. We also considered a naive strategy for the intruder team to group the intruders to simultaneously approach the protected region, which showed improvement in the intruders' payoff.

Proposed Work

The preliminary work in [95] showed an approach to formulate the intruder-versus-guardian problem, but the strategy introduced for the intruders was a naive one. One approach to design intruders' strategy more rigorously may be to use the idea of system identification. If a guardian swarm has a fixed strategy, the input to the

system are the intrusion time interval $\{T_j^{\text{int}}\}$ and the direction of intrusion $\{\psi_j^{\text{int}}\}$. The output of the system may be the payoff J_I or the probability of capture before and after the intrusion. If the intruders can predict the output of the system from the input that they control, they may be able to optimize their strategies.

However, the estimation of the input-output relation is challenging because the system is highly nonlinear, and not only the individual T_j^{int} and ψ_j^{int} , but the preceding values (T_i^{int} and ψ_i^{int} for $i = j - 1, j - 2, \dots$) affect the output. Even if we use numerical simulations to estimate the input-output relation, the design of useful test cases is a non-trivial problem. For example, say we want to estimate the output corresponding to the following input: $\{T_j^{\text{int}}\} = \{3, 5, 3, 5\}$ and $\{\psi_j^{\text{int}}\} = \{0, \pi, 0, \pi, 0\}$. (Note, there are 4 time intervals for a group of 5 intruders.) What kind of general simulation results will help us predict the output? Simulation results with $\{T_j^{\text{int}}\} = \{3, 3, 3, 3, \dots\}$ and $\{\psi_j^{\text{int}}\} = \{5, 5, 5, 5, \dots\}$ will probably help, but with how many intruders and with what $\{\psi_j^{\text{int}}\}$? More generally, what is the set of simulation results needed to estimate the output from any arbitrary choice of $\{T_j^{\text{int}}\}$ and $\{\psi_j^{\text{int}}\}$? One has to develop a systematic way of running numerical experiments to explore the input-output relation.

The suboptimality of the strategy is also true for guardians' swarming algorithm presented in Chapter 5. We showed improvements in the target-capture capability using mosquito-inspired strategies, but their optimality or theoretical predictions were not considered. In addition, frequent intrusion (or equivalently, multiple-intruder scenario) and the choice of parameters in the payoff function (i.e., η and τ) significantly affect the guardian team's performance. Much work has to be

done to design swarming strategies that address these aspects.

Appendix A: Supplemental Theoretical Results

A.1 Calculation of β^*

Figure A.1 depicts the case where the damping term $b\mathbf{v}_{T/P}$ has to be saturated to give $\mathbf{F}_P^{(\text{pursuit})} = u_{max}$. Let $n = \beta^* \|b\mathbf{v}_{T/P}\|$, $m = (1 - \beta^*) \|b\mathbf{v}_{T/P}\|$, $A = n + m$, $B = \|\mathbf{c}\mathbf{r}_{T/P}\|$, $C = \|\mathbf{c}\mathbf{r}_{T/P} + b\mathbf{v}_{T/P}\|$, and $D = \mathbf{F}_P^{(\text{pursuit})} = u_{max}$. Stewart's theorem states that

$$B^2 m + C^2 n = A(D^2 + mn). \quad (\text{A.1})$$

Using (A.1) and $A = m + n$, we can solve for n to obtain

$$n = \frac{E \pm \sqrt{E^2 + F}}{2A}, \quad (\text{A.2})$$

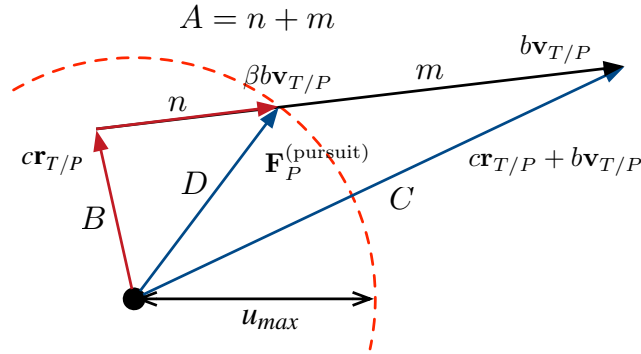


Figure A.1: Computing the saturation factor β to obtain the control law $\mathbf{F}_P^{(\text{pursuit})}$.

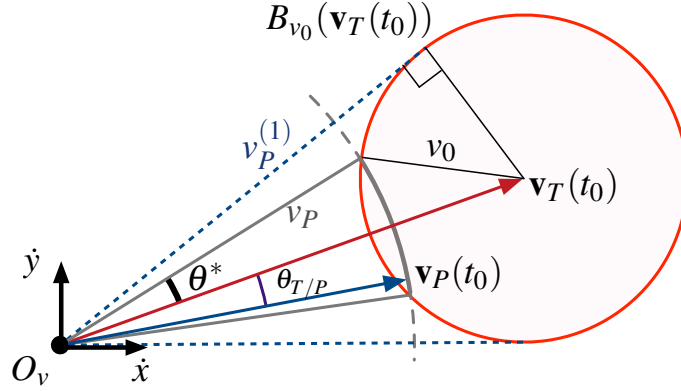


Figure A.2: Definitions of angles and speeds in the velocity space.

where $E = A^2 + B^2 - C^2$ and $F = 4A^2(D^2 - B^2)$. Noting that F is always positive, the one with $+$ is the only valid solution. The scaling factor is $\beta^* = n/A$, i.e.,

$$\beta^* = \frac{E + \sqrt{E^2 + F}}{2A^2}. \quad (\text{A.3})$$

A.2 Required N_P for Circling Strategy

Consider a circling motion with radius ρ_p . Let v_P denote the circling speed. Let $\theta_{T/P} = \cos^{-1} \left(\frac{\mathbf{v}_T \cdot \mathbf{v}_P}{\|\mathbf{v}_T\| \|\mathbf{v}_P\|} \right)$ denote the difference between the direction of motion of the target and the pursuer. First, we seek to find the maximum angle θ^* such that $\mathbf{v}_P \in B_{v_0}(\mathbf{v}_T(t_0))$. See Fig. A.2 for the definitions of the relevant quantities. For a given guardian speed v_P , the angle θ^* is the maximum allowable difference in the direction of motion to guarantee target capture. From Fig. A.2 and the law of cosines, we have

$$\theta^* = \cos^{-1} \left(\frac{v_P^2 + v_T^2 - v_0^2}{2v_P v_T} \right). \quad (\text{A.4})$$

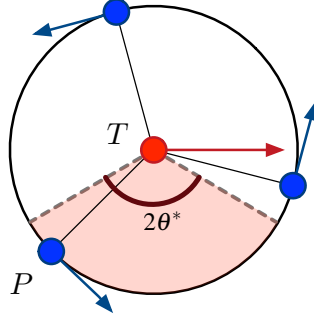


Figure A.3: Example of circling motion where $\theta^* = \pi/3$. Guardians are uniformly spaced and there is always one guardian in the fan-shaped region. When the target reaches the center, the velocity of the pursuer in the fan-shaped region satisfies $\theta_{T/P} < \theta^*$.

The angle θ^* is maximized when the limiting \mathbf{v}_P is tangent to the circle $B_{v_0}(\mathbf{v}_T)$, i.e., the blue dashed line in Fig. A.2. This geometry is achieved when v_P satisfies

$$v_P = v_P^{(1)} = \sqrt{v_T^2 - v_0^2} = v_T \sqrt{1 - \Gamma(1 - \alpha)/2}. \quad (\text{A.5})$$

However, because of the centrifugal acceleration, the achievable circling speed v_P is bounded as

$$v_P \leq v_P^{(2)} = \sqrt{\rho_p u_{max}} = v_T \sqrt{\frac{\Gamma\alpha}{2(1 + \alpha)}}. \quad (\text{A.6})$$

We choose the circling speed v_P to be

$$v_P = \min\left(v_P^{(1)}, v_P^{(2)}\right), \quad (\text{A.7})$$

i.e., use $v_P^{(1)}$ when it is achievable, otherwise, use maximum possible speed which is $v_P^{(2)}$. If the guardians are uniformly distributed on the circle, and if the number of

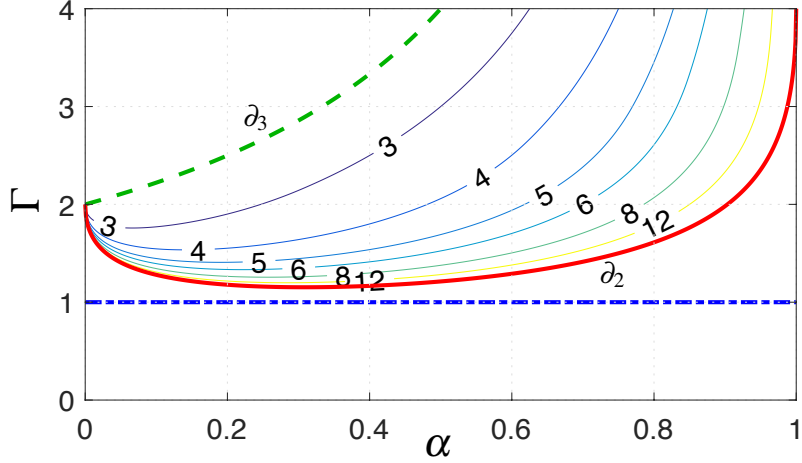


Figure A.4: Sufficient number of guardians to guarantee target capture with circling motion.

guardians N_P satisfies

$$N_P > \frac{\pi}{\theta^*}, \quad (\text{A.8})$$

there will be at least one guardian whose direction of motion satisfies $\theta_{T/P} < \theta^*$. See Fig. A.3 for the illustration of the case with $N_P = 3$. When the target reaches the center, the velocity of the pursuer in the fan-shaped region satisfies $\theta_{T/P} < \theta^*$. If the condition (A.8) is satisfied, then there is always at least one guardian in the fan-shaped region.

Figure A.4 shows the required number of guardians obtained from conditions (A.4), (A.7) and (A.8). Close to the boundary ∂_2 , the angle $\theta^* \rightarrow 0$ and the sufficient number $N \rightarrow \infty$. Close to the boundary ∂_3 , the angle $\theta^* \rightarrow \pi$ and the sufficient number $N \rightarrow 2$.

Bibliography

- [1] S. Butail, N. Manoukis, M. Diallo, J. M. Ribeiro, T. Lehmann, and D. A. Paley, “Reconstructing the flight kinematics of swarming and mating in wild mosquitoes,” *J. R. Soc. Interface.*, vol. 9, no. 75, pp. 2624–2638, 2012.
- [2] M. Ballerini, N. Cabibbo, R. Candelier, A. Cavagna, E. Cisbani, I. Giardina, A. Orlandi, G. Parisi, A. Procaccini, M. Viale, and V. Zdravkovic, “Empirical investigation of starling flocks: a benchmark study in collective animal behaviour,” *Animal Behaviour*, vol. 76, no. 1, pp. 201–215, 2008.
- [3] A. Cavagna, A. Cimarelli, I. Giardina, G. Parisi, R. Santagati, F. Stefanini, and M. Viale, “Scale-free correlations in starling flocks,” *Proc. Natl. Acad. Sci. USA*, vol. 107, no. 26, pp. 11 865–70, 2010.
- [4] M. Nagy, Z. Akos, D. Biro, and T. Vicsek, “Hierarchical group dynamics in pigeon flocks.” *Nature*, vol. 464, no. 7290, pp. 890–893, 2010.
- [5] I. Couzin, C. Ioannou, G. Demirel, T. Gross, C. Torney, A. Hartnett, L. Conradt, S. Levin, and N. Leonard, “Uninformed individuals promote democratic consensus in animal groups.” *Science*, vol. 334, no. 6062, pp. 1578–1580, 2011.
- [6] C. Becco, N. Vandewalle, J. Delcourt, and P. Poncin, “Experimental evidences of a structural and dynamical transition in fish school,” *Physica A*, vol. 367, pp. 487–493, 2006.
- [7] S. S. Killen, S. Marras, J. F. Steffensen, and D. J. McKenzie, “Aerobic capacity influences the spatial position of individuals within fish schools.” *Proc. R. Soc. B*, vol. 279, no. 1727, pp. 357–364, 2012.
- [8] U. Lopez, J. Gautrais, I. D. Couzin, and G. Theraulaz, “From behavioural analyses to models of collective motion in fish schools,” *Interface focus*, vol. 2, no. 6, pp. 693–707, 2012.

- [9] A. Attanasi, A. Cavagna, L. Del Castello, I. Giardina, S. Melillo, L. Parisi, O. Pohl, B. Rossaro, E. Shen, E. Silvestri, and M. Viale, “Collective behaviour without collective order in wild swarms of midges,” *PLoS Comput. Biol.*, vol. 10, no. 7, pp. 1–10, 2014.
- [10] D. Kelley and N. Ouellette, “Emergent dynamics of laboratory insect swarms.” *Scientific reports*, vol. 3, pp. 1–7, 2013.
- [11] M. Coetzee, R. H. Hunt, R. Wilkerson, A. D. Torre, M. B. Coulibaly, and N. J. Besansky, “*Anopheles coluzzii* and *Anopheles amharicus*, new members of the *Anopheles gambiae* complex,” *Zootaxa*, vol. 3619, no. 3, pp. 246–274, 2013.
- [12] A. Diabaté, A. Yaro, A. Dao, M. Diallo, D. Huestis, and T. Lehmann, “Spatial distribution and male mating success of *Anopheles gambiae* swarms.” *BMC Evol. Biol.*, vol. 11, no. 1, p. 184, 2011.
- [13] P. S. Sawadogo, M. Namountougou, K. H. Toé, J. Rouamba, H. Maïga, K. R. Ouédraogo, T. Baldet, L. C. Gouagna, P. Kengne, F. Simard, C. Costantini, G. Gibson, A. Diabaté, R. S. Lees, J. Gilles, and K. R. Dabiré, “Swarming behaviour in natural populations of *Anopheles gambiae* and *An. coluzzii*: Review of 4 years survey in rural areas of sympatry, burkina faso (west africa),” *Acta Trop.*, pp. S42–S52, 2013.
- [14] P. I. Howell and B. G. Knols, “Male mating biology,” *Malaria J.*, vol. 8, p. S8, 2009.
- [15] R. J. Prokopy and J. Hendrichs, “Mating behavior of *Ceratitits capitata* on a field-caged host tree,” *Ann. Entomol. Soc. Am.*, vol. 72, no. 5, pp. 642–648, 1979.
- [16] D. W. Snow, *A field study of the black and white Manakin*, *Manacus manacus*, in *Trinidad*. N. Y. Zool. Soc., 1962.
- [17] B. M. Beehler and M. S. Foster, “Hotshots, hotspots, and female preference in the organization of lek mating systems,” *Amer. Nat.*, pp. 203–219, 1988.
- [18] T. Vicsek, A. Czirók, E. Ben-Jacob, I. Cohen, and O. Shochet, “Novel type of phase transition in a system of self-driven particles,” *Phys. Rev. Lett.*, vol. 75, no. 6, pp. 1226–1229, 1995.
- [19] I. D. Couzin, J. Krause, R. James, G. D. Ruxton, and N. R. Franks, “Collective memory and spatial sorting in animal groups.” *J. Theor. Biol.*, vol. 218, pp. 1–11, 2002.
- [20] W. Scott and N. E. Leonard, “Pursuit, herding and evasion: A three-agent model of caribou predation,” *Proc. Amer. Control Conf.*, pp. 2984–2989, 2013.

- [21] V. Gazi and K. Passino, “A class of attraction/repulsion functions for stable swarm aggregations,” *Proc. IEEE Conf. Decision Control.*, vol. 3, no. 18, pp. 1567–1579, 2002.
- [22] A. Okubo, “Dynamical aspects of animal grouping: swarms, schools, flocks, and herds,” *Adv Biophys.*, vol. 22, 1986.
- [23] S. Butail, N. Manoukis, and M. Diallo, “The dance of male *Anopheles gambiae* in wild mating swarms,” *J. Med. Entomol.*, vol. 50, no. 3, pp. 552–559, 2013.
- [24] N. E. Leonard and E. Fiorelli, “Virtual leaders, artificial potentials and coordinated control of groups,” *Proc. IEEE Conf. Decision Control.*, vol. 3, pp. 2968–2973, 2001.
- [25] D. Paley, N. E. Leonard, and R. Sepulchre, “Collective motion: Bistability and trajectory tracking,” *Proc. IEEE Conf. Decision Control.*, vol. 2, pp. 1932–1937, 2004.
- [26] R. Olfati-Saber and R. Murray, “Flocking with obstacle avoidance: cooperation with limited information in mobile networks,” *42nd IEEE Conf. Decision Control*, pp. 2022–2028, 2003.
- [27] V. Gazi, “Swarm aggregations using artificial potentials and sliding-mode control,” *IEEE Trans. Rob.*, vol. 21, no. 6, pp. 1208–1214, 2005.
- [28] C. Robin and S. Lacroix, “Multi-robot target detection and tracking : taxonomy and survey,” *Auton. Robot.*, vol. 40, no. 4, pp. 729–760, 2016.
- [29] T. H. Chung and G. A. Hollinger, “Search and pursuit-evasion in mobile robotics a survey,” *Auton. Robot.*, vol. 31, no. 4, pp. 299–316, 2011.
- [30] R. Isaacs, *Differential games: a mathematical theory with applications to warfare and pursuit, control and optimization*. Courier Corporation, 1999.
- [31] P. Zarchan, “Tactical and strategic missile guidance,” *Prog. Astronaut. Aeronaut.*, vol. 176, 2002.
- [32] E. Justh and P. Krishnaprasad, “Steering laws for motion camouflage,” *Proc. R. Soc. A Math., Phys. Eng. Sci.*, vol. 462, no. 2076, pp. 3629–3643, 2006.
- [33] F. Nesline and P. Zarchan, “A new look at classical vs modern homing missile guidance,” *J. Guid., Control, and Dyn.*, pp. 78–85, 1981.
- [34] S. Ghawghawe and D. Ghose, “Pure proportional navigation against time-varying target manoeuvres,” *IEEE Trans. Aerosp. Electron. Syst.*, vol. 32, no. 4, pp. 1336–1347, 1996.
- [35] F. Adler, “Missile guidance by three-dimensional proportional navigation,” *J. Appl. Phys.*, vol. 27, no. 5, pp. 500–507, 1956.

- [36] E. Kreindler, “Optimality of proportional navigation,” *AIAA J.*, vol. 11, no. 7, pp. 878–880, 1973.
- [37] H. Cho, C. K. Ryoo, and M.-J. Tahk, “Closed-form optimal guidance law for missiles of time-varying velocity,” *J. Guid., Control, and Dyn.*, vol. 19, no. 5, pp. 1017–1022, 1996.
- [38] T. L. Song and T. Y. Um, “Practical guidance for homing missiles with bearings-only measurements,” *IEEE Trans. Aerosp. Electron. Syst.*, vol. 32, no. 1, pp. 434–443, 1996.
- [39] D. Zhou, C. Mu, and W. Xu, “Adaptive sliding-mode guidance of a homing missile,” *J. Guid., Control, and Dyn.*, vol. 22, no. 4, pp. 589–594, 1999.
- [40] Y. B. Shtessel, “Guidance and control of missile interceptor using second-order sliding modes,” *IEEE Trans. Aerosp. Electron. Syst.*, vol. 45, no. 1, pp. 110–124, 2009.
- [41] K. Ghose, T. Horiuchi, P. Krishnaprasad, and C. Moss, “Echolocating bats use a nearly time-optimal strategy to intercept prey,” *PLoS Biol.*, vol. 4, no. 5, pp. 865–873, 2006.
- [42] R. Olberg, A. Worthington, and K. Venator, “Prey pursuit and interception in dragonflies,” *J. Comp. Physiol. A Neuroethol. Sens. Neural. Behav. Physiol.*, vol. 186, no. 2, pp. 155–162, 2000.
- [43] J. Lee, R. Huang, A. Vaughn, and X. Xiao, “Strategies of path-planning for a UAV to track a ground vehicle,” *AINS Conf.*, 2003.
- [44] T. H. Kim and T. Sugie, “Cooperative control for target-capturing task based on a cyclic pursuit strategy,” *Automatica*, vol. 43, no. 8, pp. 1426–1431, 2007.
- [45] S. D. Bopardikar, F. Bullo, and J. P. Hespanha, “A cooperative homicidal chauffeur game,” *Automatica*, vol. 45, no. 7, pp. 1771–1777, 2009.
- [46] J. A. Marshall, M. E. Broucke, and B. A. Francis, “Formations of vehicles in cyclic pursuit,” *IEEE Trans. Autom. Control*, vol. 49, no. 11, pp. 1963–1974, 2004.
- [47] K. S. Galloway, E. W. Justh, and P. Krishnaprasad, “Portraits of cyclic pursuit,” *Decision and Control and Europ. Control Conf.*, pp. 2724–2731, 2011.
- [48] S. Hara, T.-H. Kim, and Y. Hori, “Distributed formation control for target-enclosing operations based on a cyclic pursuit strategy,” *IFAC Proc. Volumes*, vol. 41, no. 2, pp. 6602–6607, 2008.
- [49] J. L. Ramirez-Riberos, M. Pavone, E. Frazzoli, and D. W. Miller, “Distributed control of spacecraft formations via cyclic pursuit: Theory and experiments,” *J. Guid., Control, and Dyn.*, vol. 33, no. 5, pp. 1655–1669, 2010.

- [50] A. Antoniadis, H. J. Kim, and S. Sastry, “Pursuit-evasion strategies for teams of multiple agents with incomplete information,” *42nd IEEE Conf. Decision Control*, pp. 756–761, 2003.
- [51] J. W. Durham, A. Franchi, and F. Bullo, “Distributed pursuit-evasion without mapping or global localization via local frontiers,” *Auton. Robot.*, vol. 32, pp. 81–95, 2012.
- [52] R. M.-c. U. Ruiz, J. Luis, M. J.-p. Laumond, and S. Hutchinson, “Tracking an omnidirectional evader with a differential drive robot,” *Auton. Robot.*, vol. 31, pp. 345–366, 2011.
- [53] Y. Tian and N. Sarkar, “Game-based pursuit evasion for nonholonomic wheeled mobile robots subject to wheel slips,” *Adv. Rob.*, vol. 27, pp. 1087–1097, 2017.
- [54] J. Moon, K. Kim, and Y. Kim, “Design of missile guidance law via variable structure control,” *J. Guid., Control, and Dyn.*, vol. 24, no. 4, pp. 659–664, 2001.
- [55] W. Li and S. Member, “A dynamics perspective of pursuit-evasion : Capturing and escaping when the pursuer runs faster than the agile evader,” *IEEE Trans. Autom. Control*, vol. 62, no. 1, pp. 451–457, 2017.
- [56] D. Shishika, N. C. Manoukis, S. Butail, and D. A. Paley, “Male motion coordination in anopheline mating swarms,” *Sci. Rep.*, vol. 4, pp. 1–7, 2014.
- [57] D. Shishika and D. A. Paley, “Lyapunov stability analysis of a mosquito-inspired swarm model,” *Proc. IEEE Conf. Decision Control.*, pp. 482–488, 2015.
- [58] D. Shishika, J. K. Yim, and D. A. Paley, “Robust Lyapunov control design for bioinspired pursuit with autonomous hovercraft,” *IEEE Trans. Control Syst. Technol.*, vol. 25, no. 99, pp. 1–12, 2016.
- [59] D. Shishika and D. A. Paley, “Mosquito-inspired quadrotor swarming and pursuit for cooperative defense against fast intruders,” (*Submitted to*) *Auton. Robot.*, 2017.
- [60] D. Shishika, J. K. Yim, and D. A. Paley, “Bio-inspired pursuit with autonomous hovercraft using Lyapunov-based control,” *Proc. Amer. Control Conf.*, 2015.
- [61] D. Shishika and D. A. Paley, “Mosquito-inspired swarming algorithm for decentralized pursuit,” (*To appear in*) *Proc. Amer. Control Conf.*, 2017.
- [62] E. Bullmore and O. Sporns, “Complex brain networks: graph theoretical analysis of structural and functional systems.” *Nat. Rev. Neurosci.*, vol. 10, pp. 186–198, 2009.

- [63] R. O. Duda, P. E. Hart, and D. G. Stork, *Pattern Classification*. John Wiley & Sons, 2012.
- [64] P. Holme and J. Saramäki, “Temporal networks,” *Phys. Rep.*, vol. 519, pp. 1–28, 2012.
- [65] C. D. Godsil and G. Royle, *Algebraic Graph Theory*. New York: Springer, 2001.
- [66] S. Kirkpatrick, “Optimization by simulated annealing: Quantitative studies,” *J. Stat. Phys.*, vol. 34, pp. 975–986, 1984.
- [67] C. Pernetier, B. Warren, K. R. Dabiré, I. J. Russell, and G. Gibson, ““Singing on the wing” as a mechanism for species recognition in the malarial mosquito *Anopheles gambiae*.” *Curr. Biol.*, vol. 20, no. 2, pp. 131–136, 2010.
- [68] W. Takken and B. G. J. Knols, “Odor-mediated behavior of afrotropical malaria mosquitoes,” *Annu. Rev. Entomol.*, vol. 44, no. 1, pp. 131–157, 1999.
- [69] C. E. Shannon, “A mathematical theory of communication,” *ACM SIGMOBILE MC2R*, vol. 5, pp. 3–55, 2001.
- [70] K. Lorenz, “Ritualized fighting,” *The Natural History of Aggression*, vol. 7, 1964.
- [71] R. W. Matthews and J. R. Matthews, *Insect Behavior*. Springer, The Netherlands, 2010.
- [72] J. W. Bradbury, “The evolution of leks,” *Natural selection and social behavior*, pp. 138–169, 1981.
- [73] N. C. Manoukis and A. Diabate, “Structure and dynamics of male swarms of *Anopheles gambiae*,” *J. Med. Entomol.*, vol. 46, no. 2, pp. 227–235, 2009.
- [74] A. Diabaté, A. Dao, A. S. Yaro, A. Adamou, R. Gonzalez, N. C. Manoukis, S. F. Traoré, R. W. Gwadz, and T. Lehmann, “Spatial swarm segregation and reproductive isolation between the molecular forms of *Anopheles gambiae*.” *Proc. R. Soc. B*, vol. 276, pp. 4215–22, 2009.
- [75] N. C. Manoukis, J. R. Powell, M. B. Touré, A. Sacko, F. E. Edillo, M. B. Coulibaly, S. F. Traoré, C. E. Taylor, and N. J. Besansky, “A test of the chromosomal theory of ecotypic speciation in *Anopheles gambiae*,” *Proc. Natl. Acad. Sci. USA*, vol. 105, no. 8, pp. 2940–2945, 2008.
- [76] E. F. Knipling, “The basic principles of insect population suppression and management,” *Agriculture hand-book*, vol. 512, 1979.
- [77] K. S. Aultman, B. J. Beaty, and E. D. Walker, “Genetically manipulated vectors of human disease: a practical overview,” *Trends in Parasitology*, vol. 17, pp. 507–510, 2001.

- [78] S. Butail, “Motion reconstruction of animal groups: From schooling fish to swarming mosquitoes,” Ph.D. dissertation, 2012.
- [79] E. Wei, E. W. Justh, and P. Krishnaprasad, “Pursuit and an evolutionary game,” *Proc. Roy. Soc. London Ser. A: Math. Phys. Eng. Sci.*, vol. 465, no. 2105, pp. 1539–1559, 2009.
- [80] S. M. Iams, “Characterizing Mosquito Flight Using Measurement and Simulation,” no. January, p. 136, 2014.
- [81] H. Khalil and J. Grizzle, *Nonlinear Systems*. Upper Saddle River: Prentice hall, 2002.
- [82] T. Binazadeh and M. Yazdanpanah, “Robust partial control design for nonlinear control systems: a guidance application,” *Proc. Inst. Mech. Eng., Part I: J. Syst. Control Eng.*, vol. 226, no. 2, pp. 233–242, 2012.
- [83] R. Vidal and O. Shakernia, “Probabilistic pursuit-evasion games: theory, implementation, and experimental evaluation,” *IEEE Trans. Robot. Autom.*, vol. 18, no. 5, pp. 662–669, 2002.
- [84] N. Kasdin and D. Paley, *Engineering Dynamics: A Comprehensive Introduction*. Princeton University Press, 2011.
- [85] K. Tanaka, M. Iwasaki, and H. Wang, “Switching control of an R/C hovercraft: stabilization and smooth switching,” *IEEE Trans. Syst., Man, Cybern. B*, vol. 31, no. 6, pp. 853–863, 2001.
- [86] S. Fuller and R. Murray, “A hovercraft robot that uses insect-inspired visual autocorrelation for motion control in a corridor,” *IEEE Int. Conf. Robot. and Biomimetics. (ROBIO)*, pp. 1474–1481, 2011.
- [87] F. Roubieu, J. Serres, N. Franceschini, F. Ruffier, and S. Viollet, “A fully-autonomous hovercraft inspired by bees: Wall following and speed control in straight and tapered corridors,” *IEEE Int. Conf. Robot. and Biomimetics. (ROBIO)*, pp. 1311–1318, 2012.
- [88] C. Detweiler, B. Griffin, and H. Roehr, “Omni-directional hovercraft design as a foundation for MAV education,” *IEEE/RSJ Int. Conf. Intell. Robot. and Syst.*, pp. 786–792, 2012.
- [89] A. Stubbs, V. Vladimerou, A. Fulford, D. King, and J. Strick, “A hovercraft testbed for networked and decentralized control,” *IEEE Control Syst. Mag.*, vol. 26, no. 3, pp. 56–69, 2006.
- [90] C. Ryoo, Y. Kim, M. Tahk, and K. Choi, “A missile guidance law based on Sontag’s formula to intercept maneuvering targets,” *Int. J. Control, Autom., and Syst.*, vol. 5, no. 4, pp. 397–409, 2007.

- [91] W. Chen, “Nonlinear disturbance observer-enhanced dynamic inversion control of missiles,” *J. Guid., Control, and Dyn.*, vol. 26, no. 1, pp. 161–166, 2003.
- [92] A. Levant, “Higher-order sliding modes, differentiation and output-feedback control,” *Int. J. Control.*, vol. 76, no. 9-10, pp. 924–941, 2003.
- [93] Y. Guo, S. Wang, Y. Yao, and B. Yang, “Evader maneuver on consideration of energy consumption in flight vehicle interception scenarios,” *Aerosp. Sci. Technol.*, vol. 15, no. 7, pp. 519–525, 2011.
- [94] A. Levant, “Flocking for multi-agent dynamic systems: Algorithms and theory,” *IEEE Trans. Autom. Control*, vol. 51, pp. 1–20, 2006.
- [95] D. Shishika, K. Sherman, and D. A. Paley, “Competing swarms of autonomous vehicles: Intruders versus guardians,” (*Submitted to*) *Dyn. Syst. Control Conf.*, 2017.
- [96] Z. Zuo, “Trajectory tracking control design with command-filtered compensation for a quadrotor,” *IET Control Theory Appl.*, vol. 4, no. 11, pp. 2343–2355, 2010.
- [97] B. Friedland and Y.-J. Park, “On adaptive friction compensation,” *IEEE Trans. Autom. Control*, vol. 37, no. 10, pp. 1609–1612, 1992.
- [98] J. Downes, “The swarming and mating flight of *Diptera*,” *Annu. Rev. Entomol.*, vol. 14, no. 1, pp. 271–298, 1969.
- [99] T. Brock-Clutton and A. C. Vincent, “Sexual selection and the potential reproductive rates of males and females,” *Nature*, vol. 351, no. 6321, p. 58, 1991.
- [100] L. J. Cator, B. J. Arthur, L. C. Harrington, and R. R. Hoy, “Harmonic convergence in the love songs of the dengue vector mosquito,” *Science*, vol. 323, no. 5917, pp. 1077–1079, 2009.
- [101] L. J. Cator, K. R. Ng’Habi, R. R. Hoy, and L. C. Harrington, “Sizing up a mate: Variation in production and response to acoustic signals in *Anopheles gambiae*,” *Behav. Ecol.*, pp. 1033–1039, 2010.
- [102] C.-d. Yang and C.-c. Yang, “Analytical solution three-dimensional realistic true proportional navigation,” *J. Guid., Control, and Dyn.*, vol. 19, no. 3, pp. 569–577, 1996.
- [103] Y.-C. Chiou and C.-Y. Kuo, “Geometric approach to three-dimensional missile guidance problem,” *J. Guid., Control, and Dyn.*, vol. 21, no. 2, pp. 335–341, 1998.

- [104] P. Reddy, E. Justh, and P. Krishnaprasad, “Motion camouflage in three dimensions,” *Proc. IEEE Conf. Decision Control.*, no. 1, pp. 3327–3332, 2006.
- [105] M. H. Shafiei and T. Binazadeh, “New approach to nonlinear guidance law design,” *Int. J. Innovative Comput. Appl.*, vol. 8, no. 5, 2012.
- [106] R. L. Shaw, *Fighter Combat*. Naval Institute Press, 1985.
- [107] F. Imado, “Some aspects of a realistic three-dimensional pursuit-evasion game,” *J. Guid., Control, and Dyn.*, vol. 16, no. 2, pp. 289–293, 1993.
- [108] J. S. McGrew, J. P. How, B. Williams, and N. Roy, “Air-combat strategy using approximate dynamic programming,” *J. Guid., Control, and Dyn.*, vol. 33, no. 5, pp. 1641–1654, 2010.
- [109] H. Huang, J. Ding, W. Zhang, and C. J. Tomlin, “A differential game approach to planning in adversarial scenarios: A case study on capture-the-flag,” *IEEE Int. Conf. Robot. Autom.*, pp. 1451–1456, 2011.
- [110] G. C. Chasparis and J. S. Shamma, “Linear-programming-based multi-vehicle path planning with adversaries,” *Proc. Amer. Control Conf.*, pp. 1072–1077, 2005.
- [111] M. G. Earl and R. D’Andrea, “A decomposition approach to multi-vehicle cooperative control,” *Rob. Auton. Syst.*, vol. 55, no. 4, pp. 276–291, 2007.
- [112] M. Chen, Z. Zhou, and C. J. Tomlin, “Multiplayer reach-avoid games via low dimensional solutions and maximum matching,” *Proc. Amer. Control Conf.*, pp. 1444–1449, 2014.